



Integration of Ground Motions into
Induced Seismicity Risk Management in the
Kiskatinaw Area, Northeast B.C.

Technical Report

Prepared for



July 2023

v2.0.1

Disclaimer

ATTENTION: PLEASE READ CAREFULLY

The information prepared by Nanometrics Inc. ("Nanometrics") and contained in this document is intended to report and provide insights for the full use, as required, of the recipient(s) of this document. Recipient(s) acknowledge that, if applicable, the overall outputs contained in this document are estimates by their nature, as they are dependent upon measurements and mathematical models with varying levels of inherent uncertainty and assumptions that are typical of empirical and statistical analysis. The findings in this document should be assessed as a whole and any attempt to rely on partial analysis or summary descriptions in this document could lead to undue emphasis on particular factors or inaccurate conclusions.

The information in this document is provided with the understanding that this document is intended for use as part of a wider scope of work that may be provided by Nanometrics and Nanometrics is not providing any professional advice or recommending any one course of action based on the contents of this document.

Nanometrics endeavours to provide accurate and reliable information and insights. This document has been provided in good faith based on data collected by Nanometrics which was available at the time the document was generated and which is dependent on various factors including, but not limited to, the number, geographical distribution and/or, if applicable, the performance of commissioned stations which may be affected by factors outside of the control of Nanometrics. Without limiting the foregoing, Nanometrics Inc. specifically disclaims any responsibility if this document is inaccurate, incomplete or misleading at the time of distribution.

All information in this document is provided "as is", without warranty of any kind, express or implied, including, but not limited to any warranties of merchantability, merchantable quality or fitness for a particular purpose. In no event will Nanometrics, or its partners, suppliers, employees or agents, be liable to the recipient(s) or anyone else for any loss, damage, cost or expense of any kind, including any consequential, special or similar damages, arising in connection with results obtained from the use of this information, any decision made or action taken in reliance on this document or any information contained in this document.

Table of Contents

Disclaimer	2
Table of Contents	3
Acknowledgements	5
Introduction	1
Plain Language Summary	2
1. Phase 1 - Ground Motion Prediction	5
1.1 Introduction	5
1.2 Ground Motion Data	5
1.3 Source and Attenuation Attributes in the Fourier Domain	9
1.3.1 Displacement Spectral Fitting	14
1.4 GMPE Functional Form	16
1.4.1 Magnitude Scaling	17
1.4.2 Ground Motion Database	23
1.4.3 Distance Scaling (FR)	24
1.4.4 Regression models of PGA and PGV motions	25
1.4.5 Residual Analysis for PGA	25
1.4.6 Ground-Motion Variability	33
1.5 Site Amplification Mapping	36
1.5.1 List Of Studies Or Data Related To The Study Area	36
1.5.2 Data Input To Site Amplification Modeling	37
1.5.3 Site Amplification Modeling	42
1.5.4 Site Amplification Maps	51
1.6 Shakemaps	53
1.7 Chapter Conclusion	61
2. Phase 2 - Perception and Damage Ground Motion Thresholds	62
2.1 Introduction	62
2.2 Ground Motion Perception Levels	63
2.3 Ground Motion Damage Levels	68
2.4 Ground Motion to Intensity Conversion Equations	69
2.5 Analyzing Ground Motion In Fort St. John	74
2.6 Associating Felt Reports With Ground Motion	79
2.7 Conclusion On GMICE Choice And Perception And Damage Thresholds	84

3. Phase 3 - Review of Traffic Light Protocol Magnitude Thresholds	86
3.1 Introduction	86
3.2 Generating Maximum Magnitude Maps	86
3.3 Conclusions	96
4. Summary	98
References	101
Company Profile	106

Acknowledgements

This report has been prepared by Nanometrics Inc. with contributions from:

Mark Novakovic, Ph.D., Project Manager and Seismic Hazard Expert

Karen Assatourians, Ph.D., Seismic Hazard Expert

Nanometrics thanks ARC Resources & Tourmaline for contributing private earthquake data to the study which enhanced the available ground motion data significantly. Nanometrics also thanks Stu Venables and Michelle Gautier from the BC Energy Regulator for providing additional data and feedback throughout the study as well as BC OGRIS for funding this research.

Introduction

The project will investigate the incorporation of ground motions into traffic-light protocols (TLPs) for induced seismicity oversight with a focus on applications in the Kiskatinaw area. The objectives of the study are twofold:

1. The development of regional ground motion models for induced events, which can be used for the assessment of associated hazard in future, and
2. the review of the existing magnitude thresholds of traffic-light protocols (TLPs) on the basis of ground motions for effective induced seismicity risk management.

The project is conducted in three phases: ground motion prediction, definition of perception and potential damage thresholds, and review of traffic light protocol (TLP) magnitude thresholds on the basis of ground motions.

Plain Language Summary

Traffic light protocols (TLP) are commonly implemented regulatory systems designed to mitigate risk during oil and gas operations. TLPs are typically region specific, real-time, risk management systems with discrete response levels. Each level is defined with observable criteria and invokes specific actions to ensure a quick and effective reduction in both the number and size of induced earthquakes. Ground motions below the threshold of general perceptibility, or with occurrence rates on the same order as established background seismicity levels are categorized as “Green”. Ground motions which can be felt, but damage is unlikely fall under the “Amber” level. Ground motions which could begin to cause damage fall under the “Red” level. The traffic light levels are generally defined with ranges of magnitude which may produce the ground motion response described in each category. Specific actions or procedures are followed as traffic light levels are exceeded which could include reporting to the regulator, modifying operations, or even completely suspending operations. In order to define appropriate traffic light thresholds, the typical ground motion that can be expected to result from an earthquake with a given magnitude must be characterized, and the ground motion levels associated with human perception and possible damage must be identified.

The shaking intensity resulting from a seismic event can be broken down and simplified into three main categories: the source (earthquake magnitude), path (the earth seismic waves propagate through) and the site (localized near-surface conditions such as soft soils or hard rock). It is expected that ground shaking is the strongest when closest to the epicenter, where the strength of the shaking becomes weaker at greater distances. This is due to energy lost from wave spreading, wave scattering, the layering of rock and its composition. Depending on the makeup of the near-surface, soft and deep sediments can amplify seismic waves causing their intensities to be much stronger than a site with shallow sediments or exposed hard rock.

In the first phase of this study, ground motion recordings collected from seismic monitoring stations across the Kiskatinaw region are compiled and analyzed. A ground motion prediction equation (GMPE) is developed through the modeling of: how earthquake ground motions scale based on the magnitude of the event; how those waves attenuate or lose energy as they travel from the hypocenter to the surface; and what type of amplification may be expected for a site with particular ground condition. These models

may be evaluated for points across the Kiskatinaw region to estimate the ground shaking level resulting from an earthquake with a given size and location. The resulting ground motion estimates may be mapped to show the distribution of shaking intensities across the area, which are commonly referred to as shake maps. Shake maps are useful for planning what the impact of an event might be prior to an earthquake (scenario), and may be generated shortly after an event has occurred to map the shaking distribution across the region to action response plans.

The second phase of this study aims to review the available literature in order to identify ground motion levels associated with the perception level and the level of ground motion in which minor damage may begin to occur. Human perception can depend on what the person is doing at the time (walking, driving, sitting, lying down, etc.), if they are in a building or structure, what materials or design level is it constructed, the duration of the earthquake motions and its frequency content. Perception also ranges from barely noticeable to uncomfortable levels. Damage similarly will largely depend on the construction type of the structure (wood, masonry, concrete, steel, etc.), its design level, and overall robustness. Damage can be further broken down into non-structural and structural damage. Non-structural damage may include damage to finishes, plaster, tiles, or non-load bearing walls. This threshold is typically defined as the level of peak ground motion that is sufficient to cause cracking, chipping, or detachment of these non-structural elements, but without compromising the overall safety of the building. Structural damage includes damage to the load-bearing elements of a structure, such as beams, columns, walls, and foundations and compromises integrity and safety of the structure, and generally are the result of significantly stronger ground motion intensities than those associated with non-structural damages. In this study, any damage is considered as unacceptable, so thresholds are defined conservatively as the ground motion level which is unlikely to cause any damage.

In the third phase, ground motions associated with the perception and damage levels identified in the previous phase are related back to the earthquake magnitude which is unlikely to exceed the thresholds. Maximum magnitude maps are generated which show the maximum magnitude that could occur in any location across the region and not exceed the perception or damage threshold at any point across the region. As the proximity to the hypocenter of an event may have a large impact on the ground motion intensity experienced at the surface, maps are generated for alternative operational depth levels.

The findings of this study will be used to refine and inform the traffic light protocol definitions for the Kiskatinaw region in north east British Columbia.

1. Phase 1 - Ground Motion Prediction

1.1 Introduction

A regional ground motion model and site amplification map are developed for the Kiskatinaw area to estimate the resultant ground motions from induced events, which can be used for the assessment of the associated hazard. As part of this study, an earthquake catalog and ground motion dataset are compiled using a combination of public and private data. Regional source and attenuation attributes, which describe how ground motions scale with magnitude and how their amplitudes decay with distance, are examined using the compiled data. Moment magnitude, stress drop and other source parameters are determined following a displacement spectral fitting approach. In order to provide a more robust estimate of ground motions from significant (moderate magnitude) events where ground motion data is sparse, ground-motion simulations are leveraged. A ground-motion prediction equation (GMPE) is developed through regression analysis of recorded data where the source, path and site effects are parameterized in the model. The model is applicable for moment magnitudes of 1.25 to M6, and hypocentral distances up to 50 km. Uncertainties in the ground-motion estimates are quantified through residual analysis in terms of within-event, between-event and total variability. Finally, a site amplification map is developed for the region by correlating empirical station terms from regression analysis to publicly available geotechnical information such as depth to bedrock, surficial geology and the USGS topographic slope based V_{s30} estimates (REF). The following sections describe the data and methodology.

1.2 Ground Motion Data

Data from the following sources are collected to be used in this study:

- Operator data (ARC-Tourmaline) between 2017-2022: 327560 record components from 64 stations
- BCOGC GMM reports: 279 record components from 4 stations
- IRIS: 116242 record components from 28 stations

Station data availability prior to 2017 is insufficient to include records before this time in the regression analysis. Records corresponding to far recording distances (>50 km) and single vertical channel records are removed from the database. A total of 398571 (132857 triaxial record sets) record components from 91 stations are kept in the database for this study.

The earthquake catalog is examined and filtered in order to remove undesirable events to prevent the introduction of bias and additional uncertainties. For event-station pairs at close distances, the hypocentral distance is very sensitive to the depth of an event. Events with a depth error greater than 1 km are filtered from consideration. The catalog is further filtered to remove events with azimuthal gaps greater than 180° in order to ensure that the earthquake is well recorded by stations in all directions. In order to preserve the ‘larger’ magnitude range in the catalog, all $M_L > 2.5$ events are considered regardless of the above criteria.

Compiled raw waveforms are processed in order to compute ground motion parameters. The processing routine includes windowing, trend removal, tapering, bandpass filtering and instrument response correction. For each record, the ground motion window of interest is identified based on P and S arrival times. Where available, manual phase picks from the private arrays are used, otherwise, P and S arrivals are estimated based on a simplified traveltime model derived from the BCER regional velocity model (Nanometrics, 2020). The regional travel-time relationships for P and S waves are provided in Equations 1-1 and 1-2, respectively:

$$t_p = \{0.161R_{hyp} \quad for \ R_{hyp} \leq 50 \text{ km}, \quad (1 - 1)$$

$$t_s = \{0.33R_{hyp} + 0.5 \quad for \ R_{hyp} \leq 50 \text{ km} \quad (1 - 2)$$

where t_p and t_s are P- and S-wave travel times (s) and R_{hyp} is the hypocentral distance (km).

For a given earthquake record, the ground-motion window is defined from t_p to $t_p+4\Delta t_{sp}$ relative to the origin time, where Δt_{sp} is the S-P travel time difference. A 2-second buffer is considered at both ends of the ground-motion window to account for prediction uncertainties. This buffer is meant to ensure that the strong portion of ground motion is entirely captured. A pre-event noise window of up to 30 s, where available, prior to the start time of the ground-motion window is included in the time series to quantify the

quality of records. Figure 1-1 shows an example of windowing the ground-motion time series.

A linear trend line is subtracted from the raw waveform trace and a cosine taper is applied at each end. The resultant waveforms are then processed using a zero-phase shift 4th-order Butterworth bandpass filter. The low-pass frequency (flp) is defined as 80% of the Nyquist frequency in order to filter potential high-frequency noise as part of initial batch processing. The high-pass frequency (fhp) is defined as $\log(fhp) = 0.2 - 0.3ML + 0.3\log(Rhyp)$. This accounts for the dependence of signal-to-noise ratio on magnitude and distance. fhp typically ranges from 0.1 Hz to 3.3 Hz for the processed waveforms. The instrument response is deconvolved from the recording by complex division in the frequency domain to ensure the accurate recovery of ground-motion amplitudes over a wide-frequency band.

Finally, waveforms are visually inspected for record quality. Each record is assessed to determine if

- A. windowing parameters need refinement,
- B. the record has gaps or is incomplete within the ground-motion window of interest,
- C. the record is too noisy and seismic arrivals cannot be distinguished, or
- D. the waveforms are clipped due to the limited dynamic range of the recording instrument.

Peak ground acceleration (PGA), peak ground velocity (PGV) and Fourier Acceleration Spectra (FAS) are computed for each usable component.

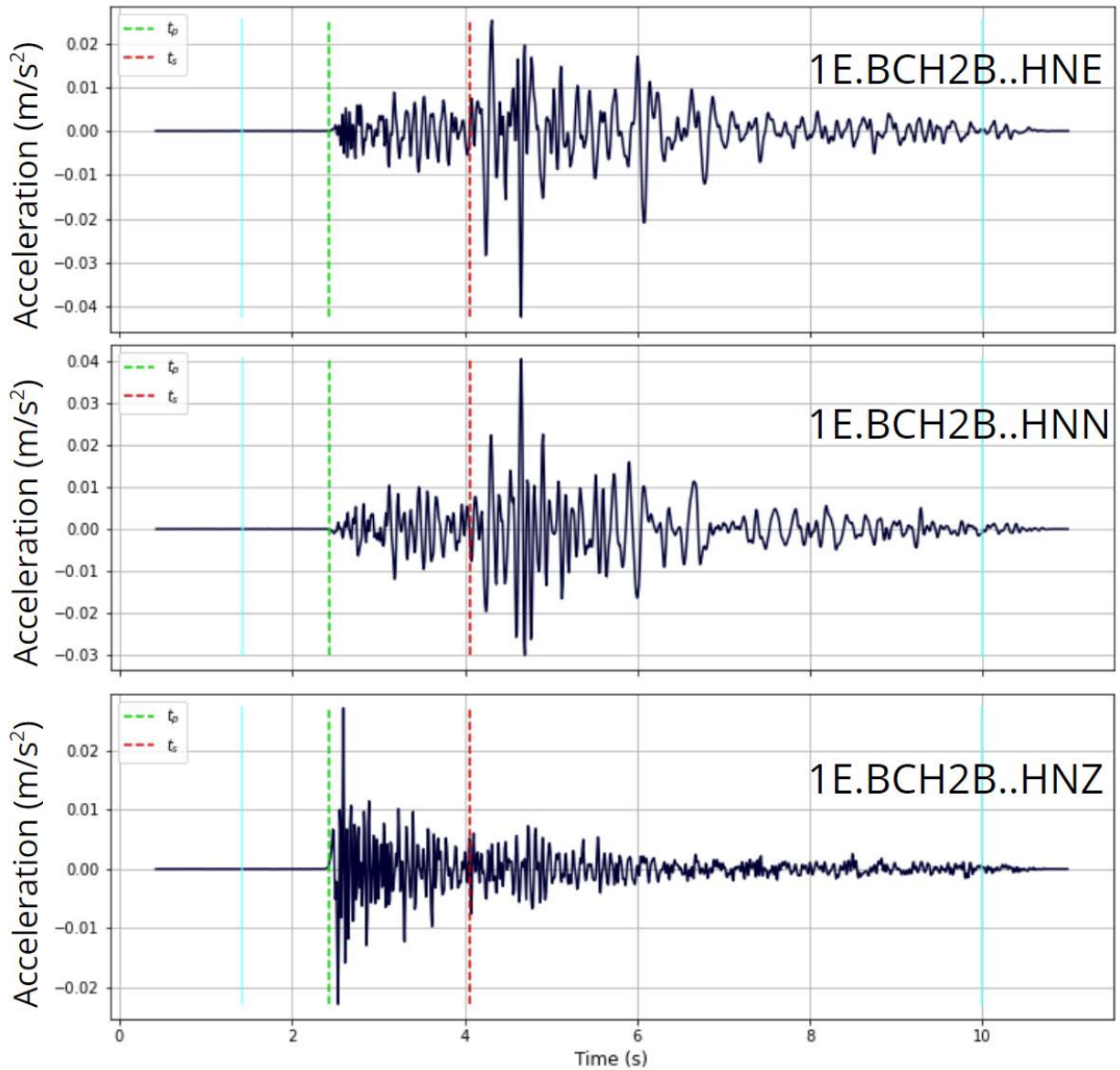
2020-09-11T22:37:26.71Z, M_L 3.44, R_{Hyp} 6.6 km


Figure 1-1: Example of a processed time series from a M_L 3.44 earthquake at hypocentral distance of 6.6 km. Each panel shows a different component of the same record in terms of velocity. The green dashed line shows the P-arrival, the red dashed line shows the S-arrival and the light blue lines indicate edges of tapering.

1.3 Source and Attenuation Attributes in the Fourier Domain

In practice, GMPEs are developed with respect to the moment magnitude scale. Moment magnitude is a more robust measurement of the earthquake size as it is valid across the entire range of magnitudes, a characteristic that is lacking in other magnitude scales. “Moment” is a physical quantity proportional to the slip on the fault multiplied by the area of the fault surface that slips; it is related to the total energy released during the earthquake. The moment can be estimated from seismograms and is then converted into the moment magnitude by a standard formula. As earthquake waves radiate from the source through the earth to the receiver, the strength of the recorded signal decreases with increasing distance. In order to relate the spectra recorded at a station to the earthquake magnitude, the signal needs to be back projected to the source. To this end, models that can correct recorded earthquake spectra to what would have been recorded at the source are required. This section details the process of modeling the attenuation attributes of ground motions in the Fourier domain in order to determine the seismic moment, moment magnitude, and other source parameters (stress drop, source radius, corner frequency) that describe the earthquake.

An equivalent point source approach is adopted to model source and attenuation characteristics of Fourier amplitudes. Vertical ground motions are considered as a proxy for unamplified horizontal component motions (e.g. Lermo and Chavez-Garcia, 1993), with the assumption that site amplification effects of vertical ground motions are small enough to neglect. Observed ground motions are regressed on an earthquake-by-earthquake basis to fit the following functional form (Yenier and Atkinson, 2014):

$$\log A(f, \mathbf{R}) = c_1(f) + F_z(\mathbf{R}) + c_2(f)R_{\text{Hyp}}, \quad (1-3)$$

where A is the Fourier spectra acceleration, f is the frequency, \mathbf{R} is the effective distance parameter, c_1 is the product of the high-frequency site effects modeled by the κ_0 operator (Anderson and Hough (1984) and the apparent source spectrum, F_z is a geometric spreading model which captures the frequency independent attenuation of ground motions due to the expansion of the wavefront, c_2 is the frequency dependant coefficient for anelastic attenuation (inverse of quality factor, Q), and R_{Hyp} is the hypocentral distance. \mathbf{R} is adopted from Yenier and Atkinson (2014) which accounts for near-distance saturation effects of ground motions and is shown in Equations 1-4 and 1-5:

$$R = \sqrt{R_{Hyp}^2 + h_{eff}^2} \quad (1-4)$$

$$h = -1.72 + 0.43M \quad (1-5)$$

where h is the effective depth term and M is the magnitude.

The $c_1(f)$ parameter represents an apparent source term that combines the effects of source and kappa:

$$c_1(f) = \log A_0(f) - \frac{\pi \kappa_0}{\ln(10)} f \quad (1-6)$$

where A_0 is the apparent acceleration source spectrum and the second term characterizes the zero-distance value of the high frequency spectral amplitude decay (Anderson and Hough (1984)). In this formulation site-to-site variations of κ_0 effects are ignored and a single value of κ_0 is applied to all sites across the region.

Attenuation rates primarily depend on the source-site distance and the properties of the rock mass which they propagate through. For close distances, direct waves dominate the ground motions where at greater distances ground motions are generally dominated by a combination of surface waves and trapped phases, which may contain multiple reflections and refractions. Theoretically, direct waves spread spherically in a whole space where their amplitudes attenuate at $R^{-1.0}$, where surface waves decay cylindrically with a rate of $R^{-0.5}$ and is generally considered independent of frequency. Depending on the focal depth, faulting mechanism and crustal structure, the transition distance can range from ~40 to 100 km. Anelastic attenuation accounts for frequency dependent effects of attenuation due to characteristics of the rock mass along the ray path, has limited effect at lower frequencies relative to high frequencies and increasing influence on resulting ground motions with increasing distance.

The attenuation trends of low frequency FAS are examined in order to assess the general shape of the geometric attenuation ahead of regression. As the geometric spreading is expected to be frequency independent, it simplifies the computational complexity of regression analysis by imposing an appropriate model ahead of time. To this end, events which have earthquake recordings within four distance bins (7.1 km - 11.9 km; 11.9 km - 15.6 km; 15.6 km - 23.6 km; and 23.6 km - 33.3 km) are identified. For each event, the mean

Normalized Fourier Acceleration Spectra

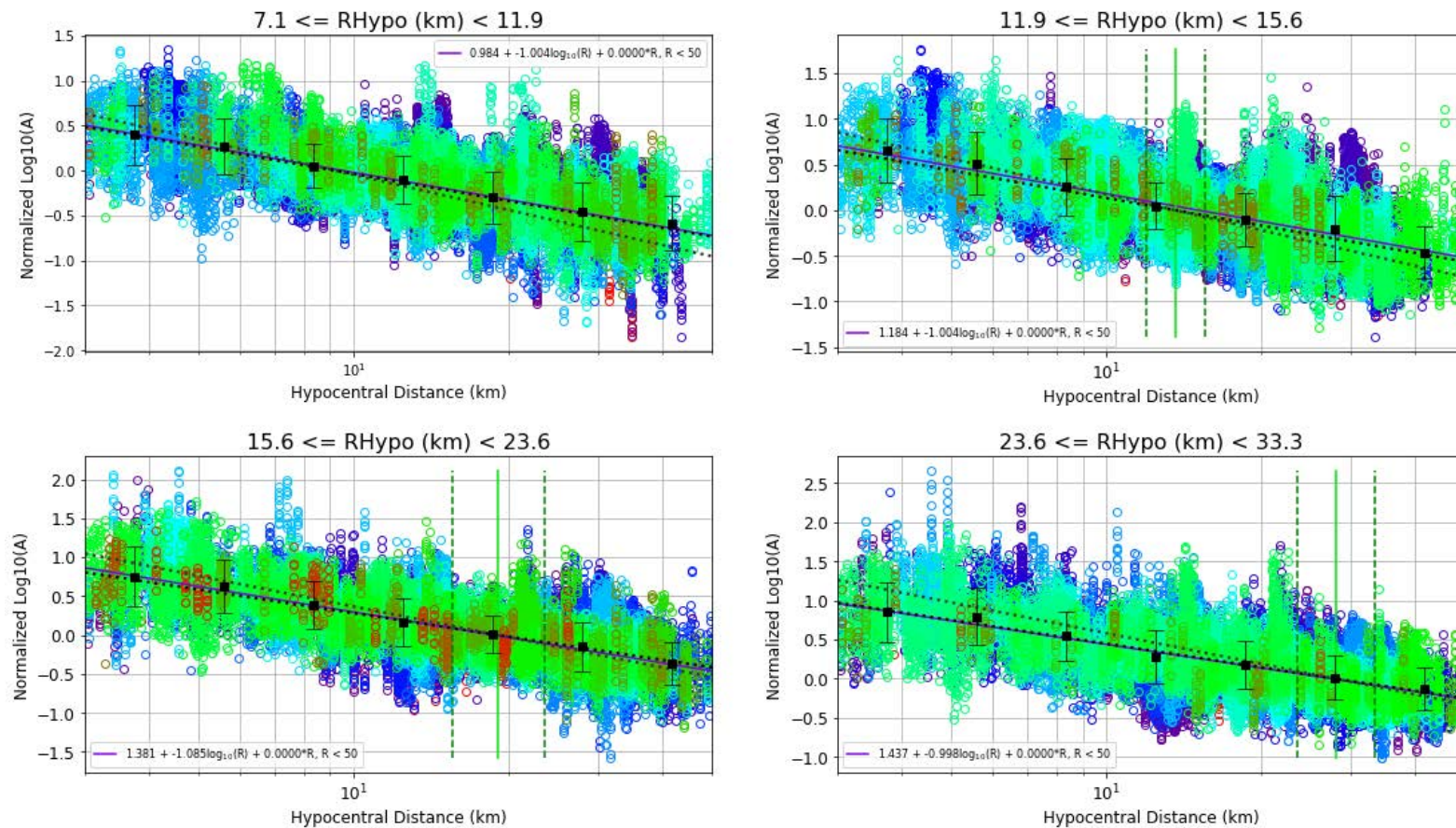


Figure 1-2: Fourier Acceleration Spectra are normalized across several distance bins (each panel represents a different bin) in order to illustrate the shape of the expected geometric spreading function (coefficient of the $\log_{10}(R)$ term in legend). Dotted lines show reference slopes for $b = -1$ and $b = -1.3$ drawn from the center of each distance bin.

amplitude within the distance range is determined and removed from all records at all distances associated with that event illustrated in Figure 1-2. This effectively normalizes the data and provides guidance on the slope and overall shape of the attenuation in the region. It is found that the geometric spreading decays with R^{-1} within 50 km and that there are limited effects of anelastic attenuation at lower frequencies. The geometric spreading term $Z(\mathbf{R})$ takes on the following form:

$$F_z(\mathbf{R}) = -1.0 \log_{10}(\mathbf{R}) \text{ for } \mathbf{R} \leq 50 \text{ km} \quad (1-7)$$

Regression analysis is conducted by removing the geometric spreading function from ground motion observations to partially correct the spectra to the source. The apparent source- κ_0 term and anelastic attenuation coefficient are solved simultaneously, then the apparent source term is decomposed to determine an appropriate κ_0 for the region. Due to the close distances considered, it was necessary to perform the regression for records greater than 10 km in order to decouple trade-offs between near-distance saturation effects, the geometric spreading function and the anelastic attenuation. At distances greater than 50 km, changes in the geometric spreading are anticipated in terms of the transition to surface wave spreading as well as potential moho bounce effects. Data beyond 50 km are excluded due to the inability to reliably resolve these effects due to sparsity in the dataset.

The imposed geometric spreading model well represents the data attaining near zero residuals, depicted in Figure 1-3. Figure 1-4 depicts the resulting anelastic attenuation coefficients converted to Q values. At frequencies greater than 10 Hz, where anelastic attenuation is expected to begin controlling the attenuation, a near constant Q value of 1800 is attained, falling between the Atkinson & Boore (2014) model for Central and Eastern North America (CENA) and the Raoof et al. (1999) model for California. Figure 1-5 depicts the near surface attenuation κ_0 parameter for each event. On average a regional κ_0 parameter of 0.0055s is attained.

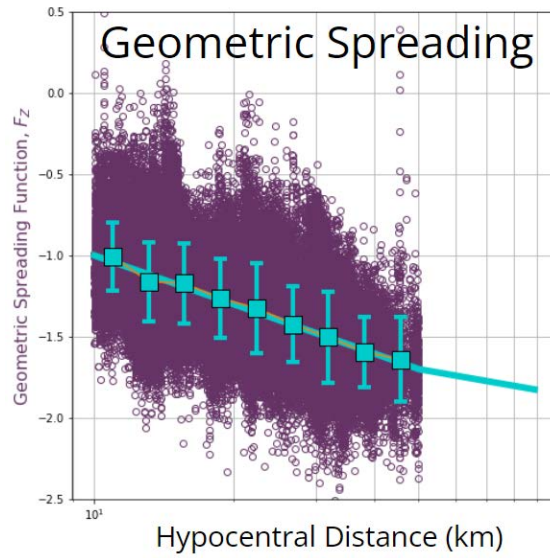


Figure 1-3: Performance of the geometric spreading model after correcting for the source and attenuation terms from Equation 1-3.

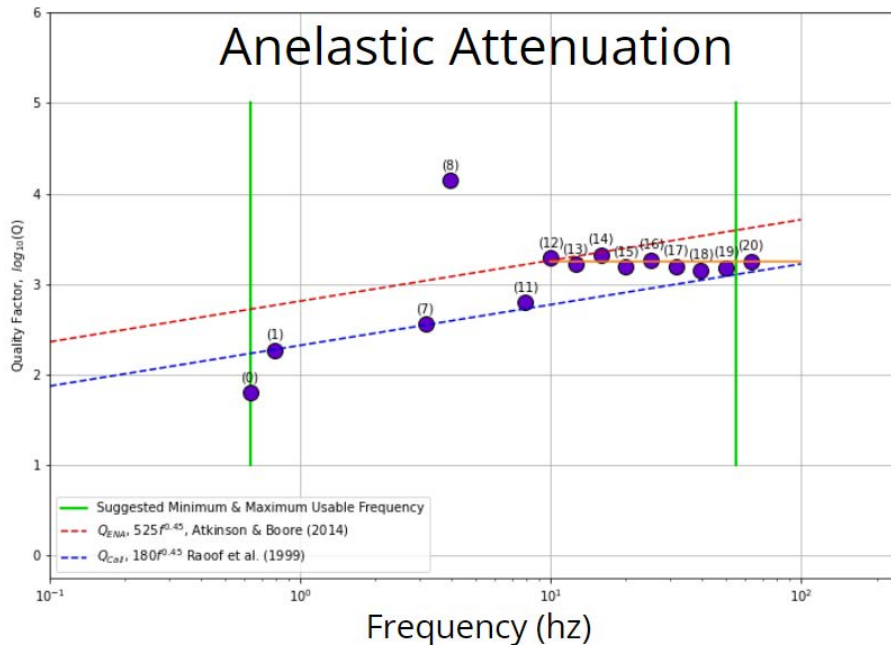


Figure 1-4: Anelastic attenuation parameter, Q-values, based on the c_2 term of Equation 1-3 compared with published models for CENA and California.

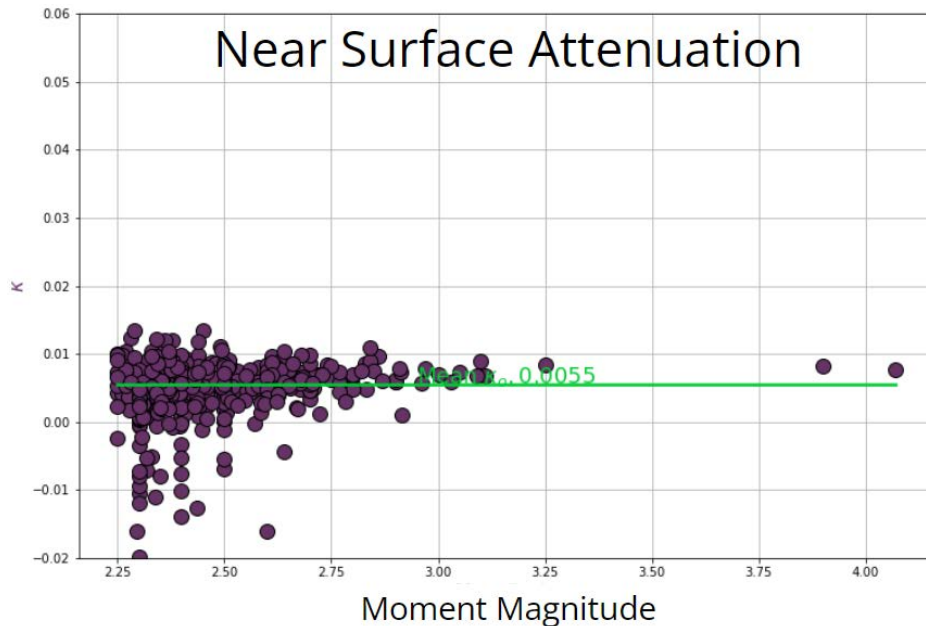


Figure 1-5: Magnitude dependence of mean κ -values associated with each event based on c_1 values in Equation 1-6 derived in the previous stage and the overall average of κ -values (green line).

1.3.1 Displacement Spectral Fitting

Apparent source terms, $A_0(f)$, are calculated by applying the attenuation corrections derived in the previous steps to the Fourier acceleration spectra recordings at each station for each event. The source corrected fourier acceleration spectra are integrated to attain event displacement source spectra. The plateau level at the low frequency end of the spectrum (typically less than 1 Hz) is used to define the seismic Moment, and is input to the Hanks & Kanimori (1979) equation for Moment Magnitude (M_w), Equation 1-8:

$$M_w = \frac{2}{3} \log_{10}(M_0) - 10.7 \quad (1 - 8)$$

where M_0 is the seismic moment in units of dyne-cm.

Next, theoretical source spectra are generated by evaluating the Brune point source model (1970) using the calculated event M_w and a range of stress parameter values ($\Delta\sigma$). For each event, the empirical source displacement spectra are compared to the ideal Brune model through a brute force algorithm to find the best spectral match by minimizing the standard

deviation of residuals between the empirical and theoretical spectra (e.g. Figure 1-6). Once the best match is identified, the stress parameter, corner frequency, seismic energy, and source radius are also derived for each event.

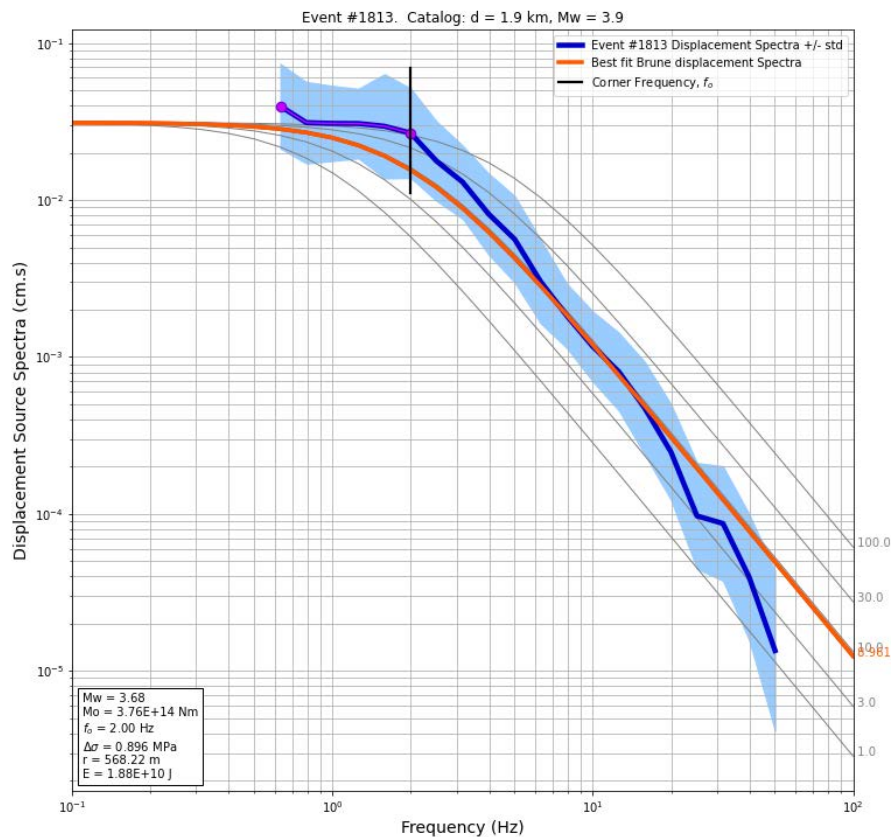


Figure 1-6: Empirical displacement source spectrum (blue line) compared against the best fitted theoretic Brune model (thick orange line), as well as other candidate source spectra evaluated for alternative stress parameter values (thin grey lines).

The resulting Mw associated with each event determined from spectral-matching are compared with the catalog local magnitude of Mahani & Kao (2020). Mw from displacement spectral fitting using regionally calibrated attenuation parameters results in magnitudes smaller than their local magnitude counterparts for $M_L > 2$ (Figure 1-7). For small magnitude events ($M_L < 2$) a near 1:1 agreement is observed. The correlation trend in Figure 1-7 and Equation 1-9 can be used for estimating the equivalent moment magnitude of events in the region with known local magnitude.

$$\begin{aligned}
 MW &= 0.73ML + 0.42 && \text{if } ML \leq 2.7 && (1-9) \\
 MW &= 0.88ML && ML > 2.7 &&
 \end{aligned}$$

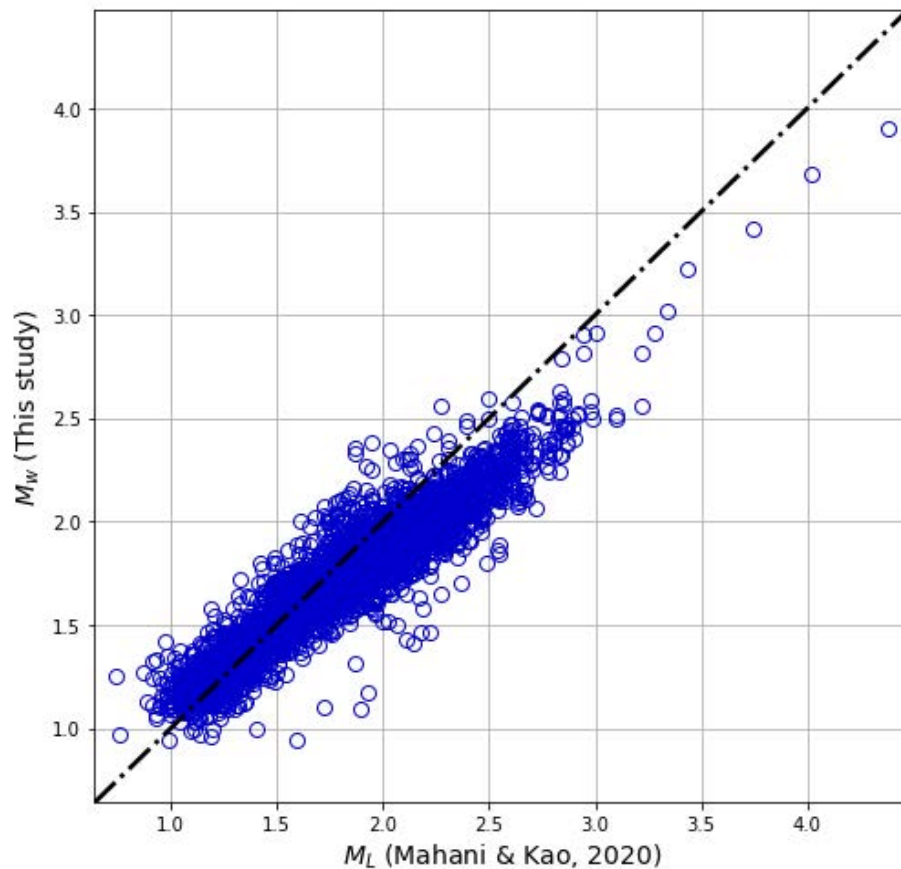


Figure 1-7: Comparison of moment magnitude of events with local magnitude.

1.4 GMPE Functional Form

The GMPE developed for the study area estimates the maximum horizontal-component peak ground motion for a given set of predictor parameters and it has the following general functional form:

$$\log(\text{PGM}) = F_M + F_R + S_j + C \tag{1-10}$$

where:

$$F_M = a_0 + a_1M + a_2M^2 \quad (1-10-1)$$

$$F_R = F_{gsprd} + F_{anelastic} \quad (1-10-2)$$

$$F_{gsprd} = b_1 \times \log(R) \quad R \leq R_1 \quad (1-10-3)$$

$$F_{anelastic} = \gamma \times R_{hyp} \quad (1-10-4)$$

In these equations PGM is the maximum horizontal-component peak ground motion parameter of interest (PGA or PGV in this study), F_M is the regional magnitude scaling function (defines how the PGM scales with M_w at a reference distance of $R = 1$ km, accounting for regional $\Delta\sigma$) and will be derived from point-source simulations to ensure stability in magnitude scaling in ranges where observations are limited. The F_R term is the regional attenuation function (represents how the PGM decays with distance, and accounts for regional geometrical spreading and anelastic attenuation). The S_j term captures the effects of near-surface site conditions at a given site (j). The site terms are referenced to the average response of all sites across the region. The C term is an overall calibration factor which accounts for any missing effects in the simulations.

1.4.1 Magnitude Scaling

In order to extend the model to larger magnitudes than have not been well recorded, simulations will be used. The relationship between stress drop and moment magnitude in combination with a crustal amplification model derived from the velocity model in the area are used to simulate the PGA and PGV for $M1 - M5.5$ range.

To derive the relations between regional M_w and stress drop, the values of these parameters of each earthquake derived from spectral matching analysis are correlated and the best model is fitted to the data. Figure 1-8 shows the scatter plot of each earthquake in M_w -Stress drop space, the best fitted model as well as a number of similar published models. The developed stress model is shown in Figure 1-8 along with models developed for natural seismicity in California and CENA (Yenier and Atkinson, 2015), as well as from induced events in Oklahoma (Novakovic et al., 2017) evaluated at the average event depth in the region of 2.4 km. It is not expected that the stress scaling derived in this study would

necessarily agree with models developed with different datasets in different regions, but it is a useful comparison to make in order to inform trends where data is sparse. Overall the stress scales at a similar rate to that observed from natural events in California, although the model tends to envelope the upper end of the stress drop range observed in this study. At lower magnitudes the model for Oklahoma matches close to the upper range of stresses though shows lower stresses for larger magnitudes. It is not anticipated that stress would scale differently at high magnitudes for induced events than natural events so it is assumed that the stress drop cannot obtain stress values larger than 100 bars by considering the saturation of the California model for magnitudes greater than 5.1. In this study a saturation term is applied to the model at $\Delta\sigma$ -100 bars where the model is extrapolated to magnitudes beyond the range of existing catalog earthquake sizes.

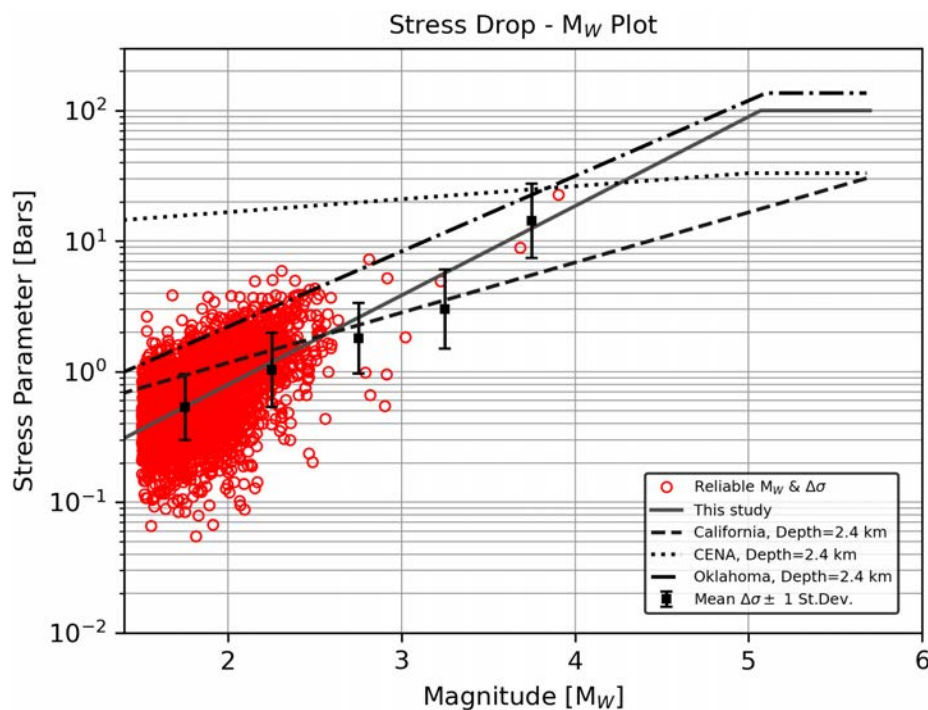


Figure 1-8: Scatter plot of catalog earthquakes' stress drops as function of magnitude (red circles) along with the fitted model (thick gray line) and a number of similar models developed for other regions evaluated at the average event depth of the region (given for comparison). The squares with whiskers show the binned stress drop means and 1-standard deviation range.

Crustal structure modifies (usually amplifies) the seismic waves that pass through it toward the surface. Crustal amplification is due to variation of seismic impedance of layers and conservation laws. To this end, a crustal amplification model, which is another component required for accurate simulations, is developed.

The BCOGC Velocity model (2020) developed for the Kiskatinaw area (Figure 1-9) is used in this study to develop a crustal amplification model. The density is estimated for each layer using Gardner et al., (1974) equation which is based on empirical relations between p-wave velocity and bulk density of matter that the wave propagates in it. The V_p and V_s at the median event depth of 2.36 km are 5.19 km/s and 3.05 km/s, respectively.

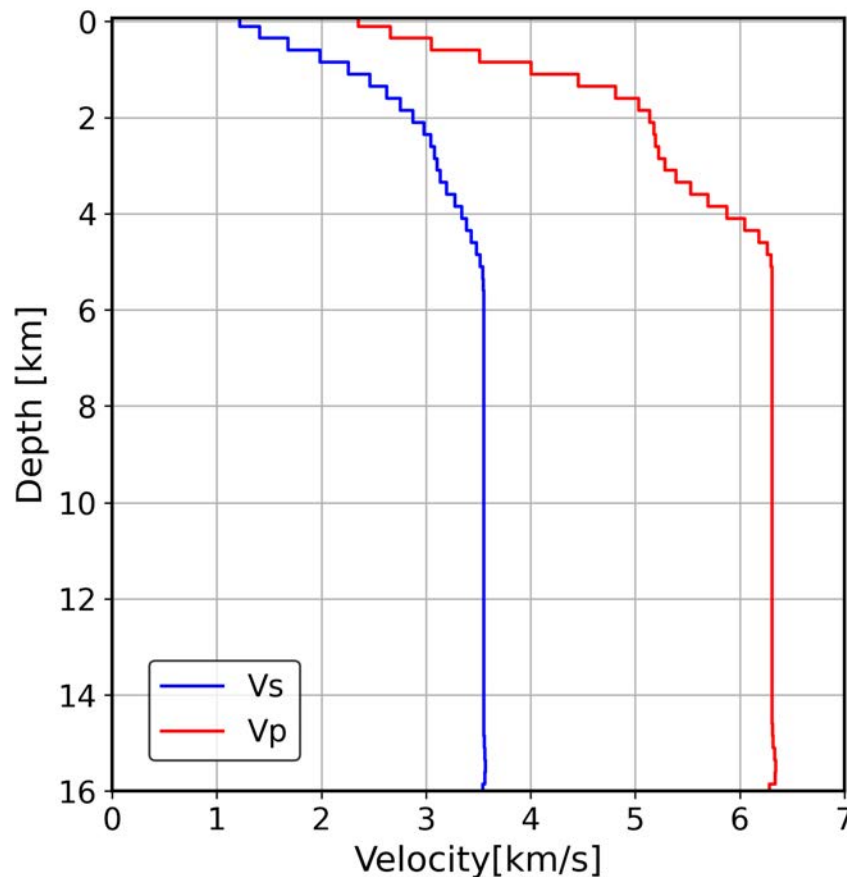


Figure 1-9: Model of velocity of P and S waves (V_p and V_s) used in this study.

The crustal amplification is modeled and estimated using D. Boore's Site_Amp program as part of the FMSIMM package (Boore, 2005). The velocity - density structure of the subsurface and the typical incident angle are the main inputs to Site_Amp program. The average incident angle is estimated using ray tracing technique by considering the average depth of events and epicentral distances to the recording stations in the region and the regional velocity structure.

Figure 1-10 shows the estimated crustal amplification as a function of frequency as well as other published models applicable to sites at the NEHRP B/C boundary ($V_{S30} = 760$ m/s) of California (Boore, 2016). Similar to the scaling of stress, it is not expected that the models match, though the California models can be used to help verify that the overall shape of the derived amplification model is appropriate. It is noted that at lower frequencies a similar trend is observed against the models developed for California, where the model developed in this study plateaus at frequencies greater than 3 Hz. This is likely attributable to differences in crustal structure and influences from the proximity of the region to the deformation front.

The magnitude scaling term (F_M) of the GMPE in Equation 1-10 is derived for Peak Ground Velocity (PGV) and Peak Ground Acceleration (PGA). The stochastic point source modeling program SMSIM (Boore, 2012) is used to simulate PGA and PGV at the source over a wide range of magnitudes ($M_w 1-6$) based on the regional source, propagation and site characteristics derived in the analyses so far. For this analysis, several hundred earthquake time histories are simulated for magnitudes between $M_w 1-6$ at 0.1 magnitude unit increments for unit distance. The mean of measured PGA and PGVs resulting from the simulations represent magnitude scaling terms (F_M) at the source. For each motion type, the model of Equation 1-10-1 is fitted to the simulated amplitudes (Figure 1-11 and 1-12 for PGA and PGV respectively) to derive parameters of the quadratic model equation (a_0 , a_1 and a_2), which are tabulated in Table 1-1. The developed magnitude scaling function will help guide the scaling of ground motions at magnitudes where empirical data is limited.

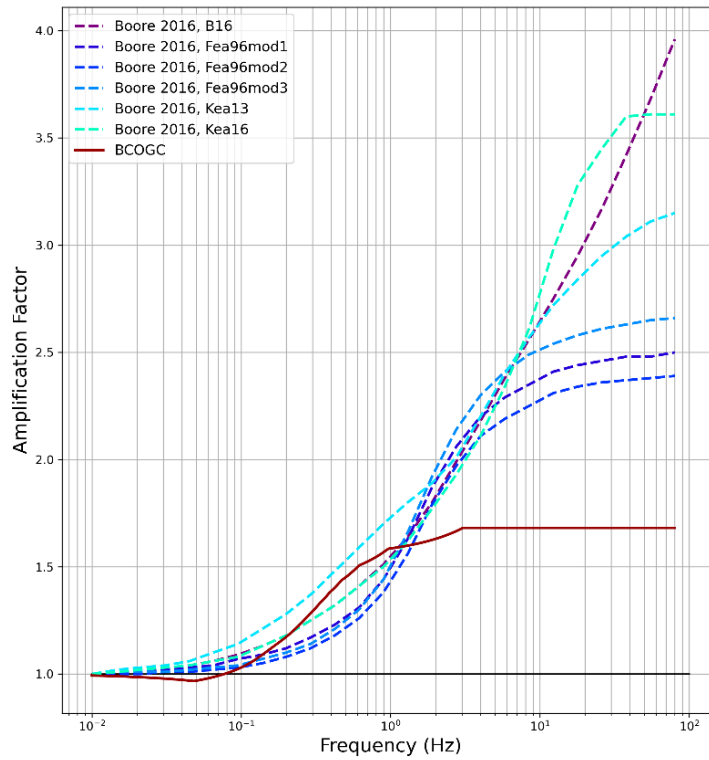


Figure 1-10: Amplification model developed in this study (red curve) along with a number of published curves applicable for California B/C sites. Each curve represents the amplification factors as a function of frequency.

Table 1-1: Contains coefficients for the magnitude scaling function for PGA and PGV.

	a_0	a_1	a_2
$F_{M,PGA}$	-1.5306	1.3068	-0.0610
$F_{M,PGV}$	-3.7629	1.3925	-0.0552

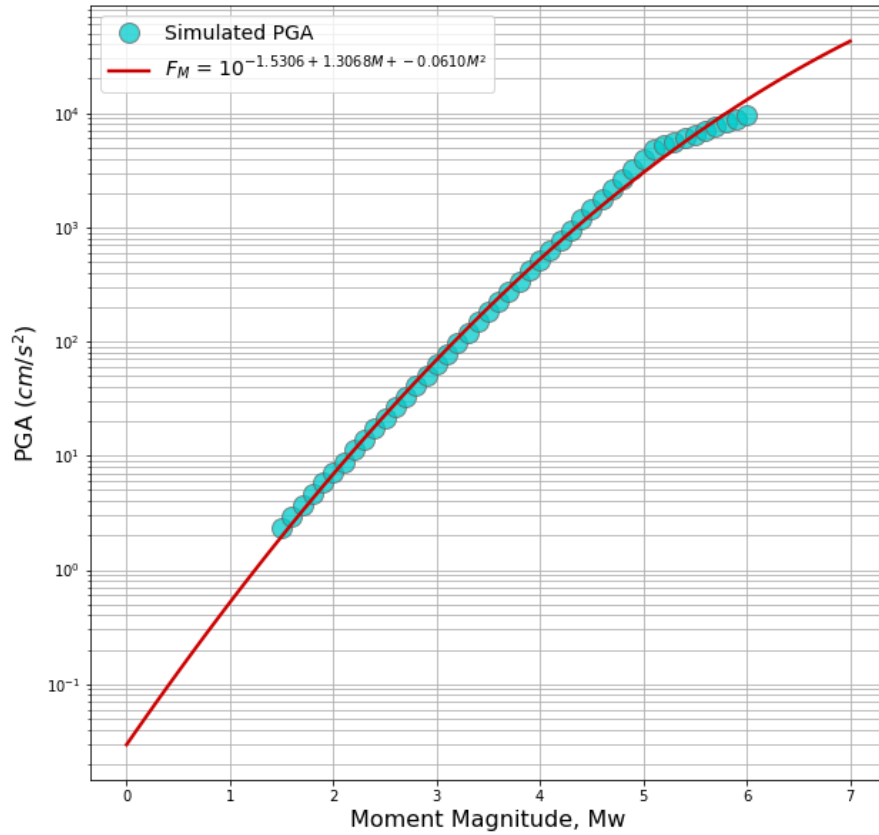


Figure 1-11: Fitted magnitude scaling term (source term) model of PGA (red line) to the SMSIM simulated amplitudes at unit distance (green circles).

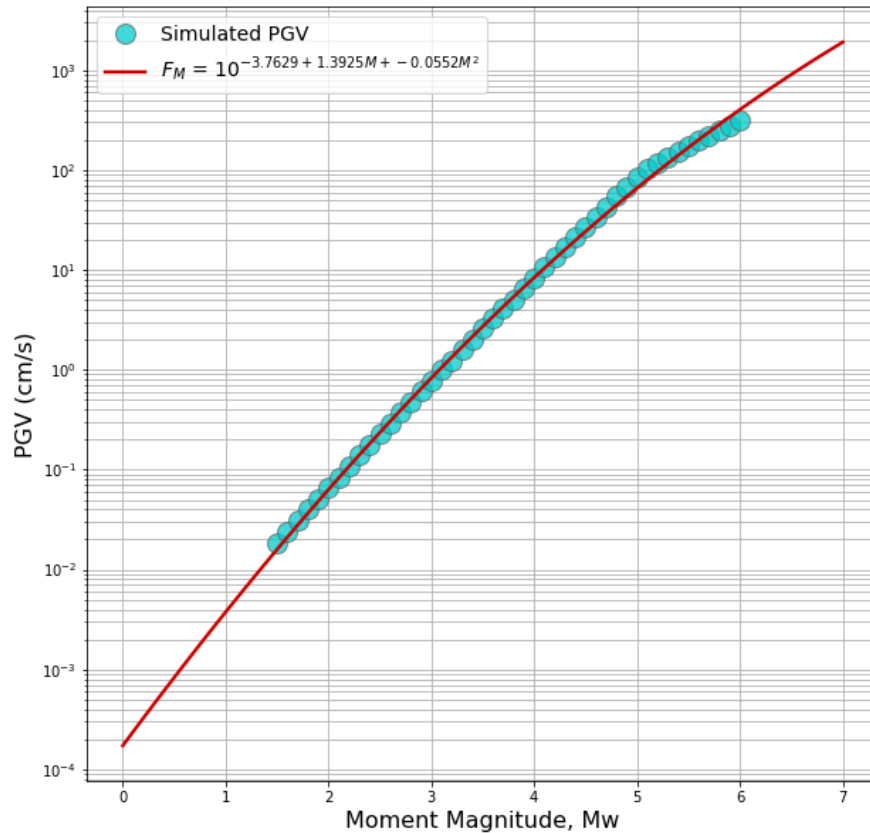


Figure 1-12: Fitted magnitude scaling term (source term) model of PGV (red line) to the SMSIM simulated amplitudes at unit distance (green circles).

1.4.2 Ground Motion Database

The ground motion database used in the regression is compiled from the maximum horizontal component PGA and PGV of records with SNR > 3. Data is rich between 2.5 - 50 km and moment magnitudes 1.25 - 2.5. Figure 1-13 shows the magnitude-distance distribution of the database records and provides insight into the range of M-R that recorded data drives the shape of the GMPE.

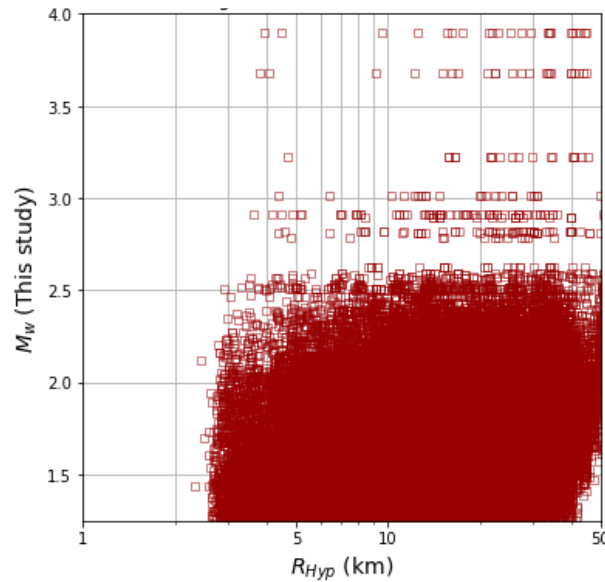


Figure 1-13: Magnitude-distance distribution of the database of records used for deriving GMPE model parameters through regression analysis.

1.4.3 Distance Scaling (F_R)

Distance scaling at close distances is predominantly controlled by the geometric spreading function, and is frequency independent. Anelastic attenuation is a frequency dependent term that controls the decay of amplitudes at further distances.

The linear geometric spreading function determined during Fourier attenuation modeling with a decay rate of $b_1 = -1.0$ is considered in the GMPE regression and the parameters of Equation 1-10-3 will be the following:

$$F_{\text{gsprd}} = -1 \times \log(R_{\text{eff}}) \quad R_{\text{eff}} \leq 50 \text{ km} \quad (1-11-1)$$

$$R_{\text{eff}} = \sqrt{R_{\text{hyp}}^2 + h^2} \quad (1-11-2)$$

$$\log_{10}(h) = -0.405 + 0.235 \times M \quad (1-11-3)$$

It is noted that sensitivity testing against the assumed geometric spreading rate of R^{-1} was performed by imposing $R^{-1.3}$ in the regression, where the decay of ground motions with distance was found to be over-corrected and that unrealistic positive anelastic attenuation

values are attained. As noted in the previous section, data availability is rich at distances from 2.2 km to 50 km, with a sufficient number of records for distances below 6 km. It is expected that the GMPE will be applicable up to 50 km, where surface wave spreading may begin to dominate the geometric spreading, such that the model would no longer be applicable due to limited observations.

1.4.4 Regression models of PGA and PGV motions

The C , γ and b parameters in equations 1-10, 1-10-3 and 1-10-4 for PGA and PGV motions are derived through linear least squares regression analyses and are listed in table 1-2.

Table 1-2: GMPE model parameters derived from regression analyses.

	b1	γ	C
PGA	-1.0	-0.01843	0.08
PGV	-1.0	-0.01572	0.35

1.4.5 Residual Analysis for PGA

Figure 1-14 shows the developed GMPE for maximum component PGA and its residuals as function of distance, azimuth, and magnitude, as well as derived empirical station terms.

Panel A shows the overall shape of the modeled attenuation as a scatter plot of PGA corrected for source and site terms as function of distance in color circles. The red line shows the derived $F_R (+C)$ model and the red squares with yellow line connecting them are the bin averages of data $F_R (+C)$ terms. An increasing trend of mismatches between observations and the model at distances less than 6 km is observed. At such close distances, the recordings are nearly directly above the epicenter of the earthquake and the ray-paths are near vertical. As a result, less energy is lost to scattering at layer interfaces and the observed motions at the surface are relatively amplified compared to those recorded at greater distances. The mismatch therefore attributed to the inability to account for the near-directly up-going waves within the magnitude scaling simulations. A secondary adjustment is developed and applied to correct for this near-distance effect, and is presented in a later section.

Panel B shows the azimuthal distribution of PGA residuals ($\log(\text{PGM}) - F_M - F_R - S_j - C$) in color circles. The red squares show 20° azimuth bin averages and the yellow line connects squares for better view. Panel B suggests there is a gentle azimuthal dependence of PGA amplitudes which would correlate with the dominant event mechanism in the region. The trend is not found to be too significant, and as it is noted that there are more than one faulting styles in the region, a directivity effect is not implemented in this study.

Panel C shows the distribution of individual ground motion recording residuals ($\log(\text{PGM}) - F_M - F_R - S_j - C$) at different moment magnitudes. The red squares with a yellow line connecting them show the residual averages in 0.5 magnitude units. The deviations of bin averages are relatively small up to magnitudes $\sim M3$ where there is a slightly increasing trend with increasing magnitudes.

Panel D shows the distribution of event residuals as a function of moment magnitude. Event residuals are calculated by averaging residuals of each event and show that as a single pink circle in panel D. The gray squares and whiskers are the averages and associated standard errors of binned event residuals respectively where the bin size is 0.1 magnitude units. This graph demonstrates that the event residual averages are generally small and statistically indistinguishable from zero within M1.4 to M2.1 magnitude band, but there is a slight trend to have positive residuals at large magnitudes (above M2.5), however, due to the small sample size it is difficult to assess whether any strong bias exists.

Panel E graphs the overall residuals of the PGAs as function of hypocentral distance shown as color circles, with binned averages shown with red squares connected with yellow line. Panel E demonstrates that the developed GMPE in its current form, accurately estimates amplitudes within a distance bin at hypocentral distances beyond $R_{\text{hyp}} = 6$ km, however, it may increasingly underestimate ground motion amplitudes at shorter distances ($R_{\text{hyp}} \leq 6\text{km}$) significantly, as noted during the discussion of Panel A. In order to correct for this effect, a model, represented by the black narrow in Panel E, is developed to match the overall shape of the mean residuals at short distances and it has the following functional form:

$$\log_{10}(A_{\text{PGA}}) = \min[-1.343 \times \log_{10}(R_{\text{hyp}}) + 1.248, 0.4917] \quad \text{for} \quad R_{\text{hyp}} \leq 8.5 \text{ km} \quad (1-12)$$

where A_{PGA} and R_{hyp} are the PGA and hypocentral distance respectively.

Panel F shows the distribution of PGA measurements corrected for station terms ($PGA / 10^{S_j}$) as function of hypocentral distance (color circles) and overlays those with color lines representing the evaluated GMPE for a number of magnitudes for comparison. Similar to findings in panel A and E of Figure 1-14, panel F shows the initial form of the GMPE model reasonably predicts PGA amplitudes at distances beyond $R_{hyp} \geq 6$ km but underpredicts amplitudes at shorter distances.

Panel G gives the values of station terms (site terms) of each station in \log_{10} units where positive terms indicate relative amplification to the average site condition in the region, and negative terms indicate relative deamplification to that of the average site condition in the region (note that the station codes of private networks' stations anonymized).

Figure 1-15 shows the performance of the developed GMPE for maximum component PGA after correcting for the near-distance effect using Equation 1-12.

Panel A shows the match between PGA measurements corrected for source and site terms has notable improvement. The residuals distributions by magnitude and distance (panels C and E respectively) improved significantly so that the binned averages further approach the zero line. In addition the event residuals (panel D) binned averages further converge to zero line on a wider range of magnitudes (M1.3-M3.1). Panel F shows improvement after applying the near-distance correction to GMPEs as PGA measurements corrected for site terms (color circles) and the GMPE curves drawn for a number of magnitudes are more consistent and well aligned. Panel G is unchanged as the correction is applied only to path terms and it didn't affect the site terms.

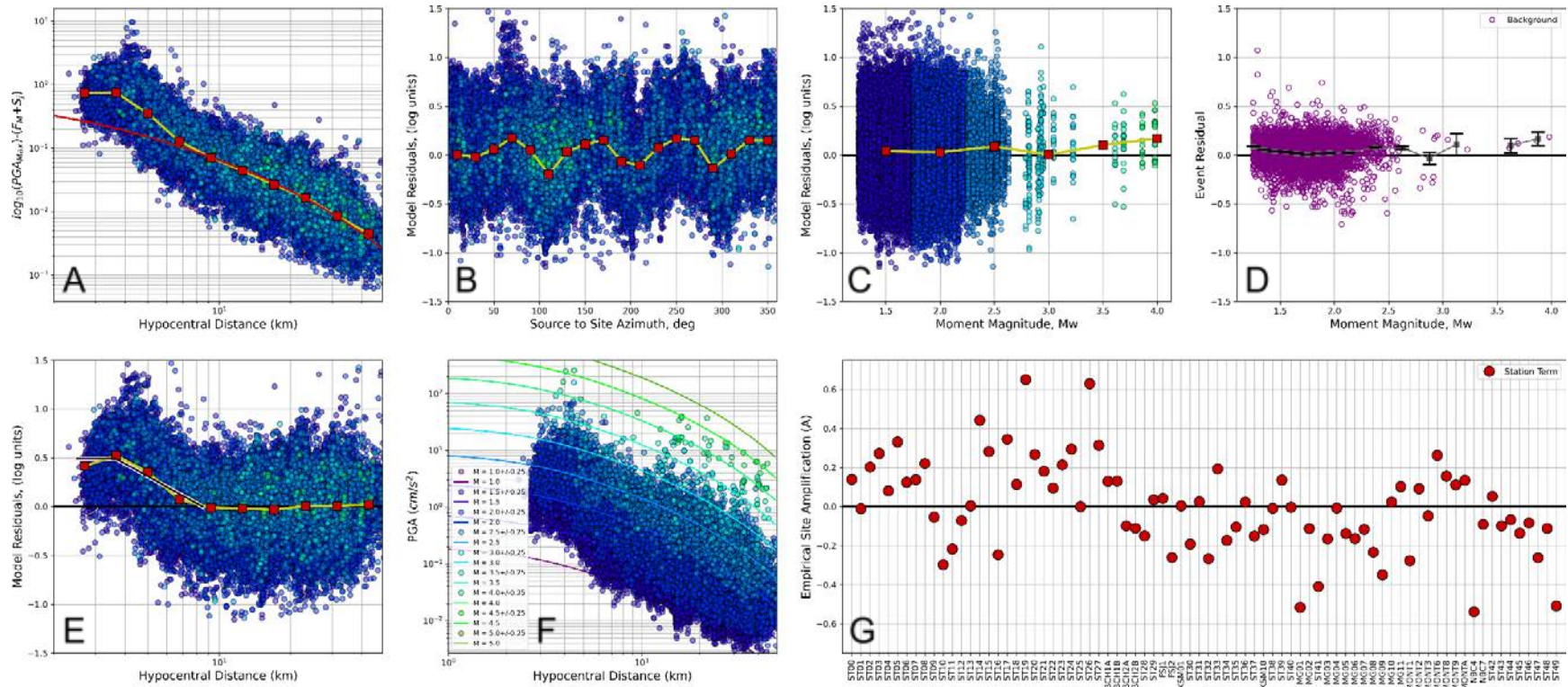


Figure 1-14: Developed GMPE of PGAs and its residuals as function of distance, azimuth, magnitude and station for comparison and residual analyses (Description of the panels given in the text).

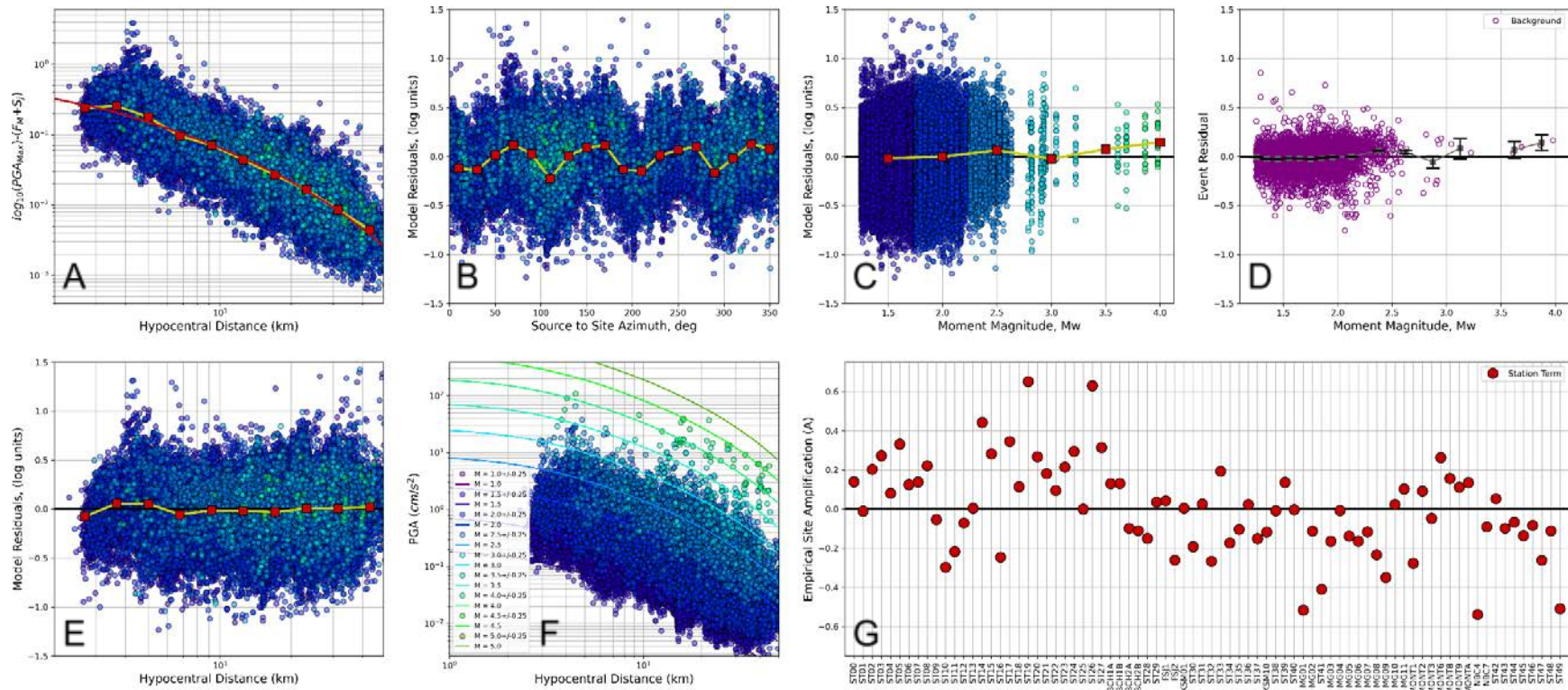


Figure 1-15: Developed GMPE of PGAs after applying Equation 1-12 correction and its residuals as function of distance, azimuth, magnitude and station for comparison and residual analyses (Description of the panels are those given in the text for Figure 1-14).

1.4.5 Residual Analysis for PGV

The residual analysis is repeated for PGV where Figure 1-16 shows the GMPE performance in terms of its residuals as function of distance, azimuth and magnitude, as well as the derived empirical site terms.

Figure 1-16 contains similar panels to those of Figure 1-14 and presents the same comparisons for PGV. Similar trends and conclusions are observed those present in the analysis of PGA. Of particular note is the presence of a similar near-distance trend. The short distance bias is modeled in a similar way to apply a correction at short distances and it has the following functional form:

$$\log_{10}(A_{PGV}) = \min[-1.118 \times \log_{10}(R_{hyp}) + 1.039, 0.3771] \quad \text{for} \quad R_{hyp} \leq 8.5 \text{ km} \quad (1-13)$$

where A_{PGV} and R_{hyp} are the PGV and hypocentral distance respectively. This term is applied to the functional form of the GMPE and the same set of graphs are redrawn for PGV in Figure 1-17. Figure 1-17 demonstrates similar improvements in the estimation of maximum horizontal PGV with the implementation of the near-distance correction as was observed with PGA.

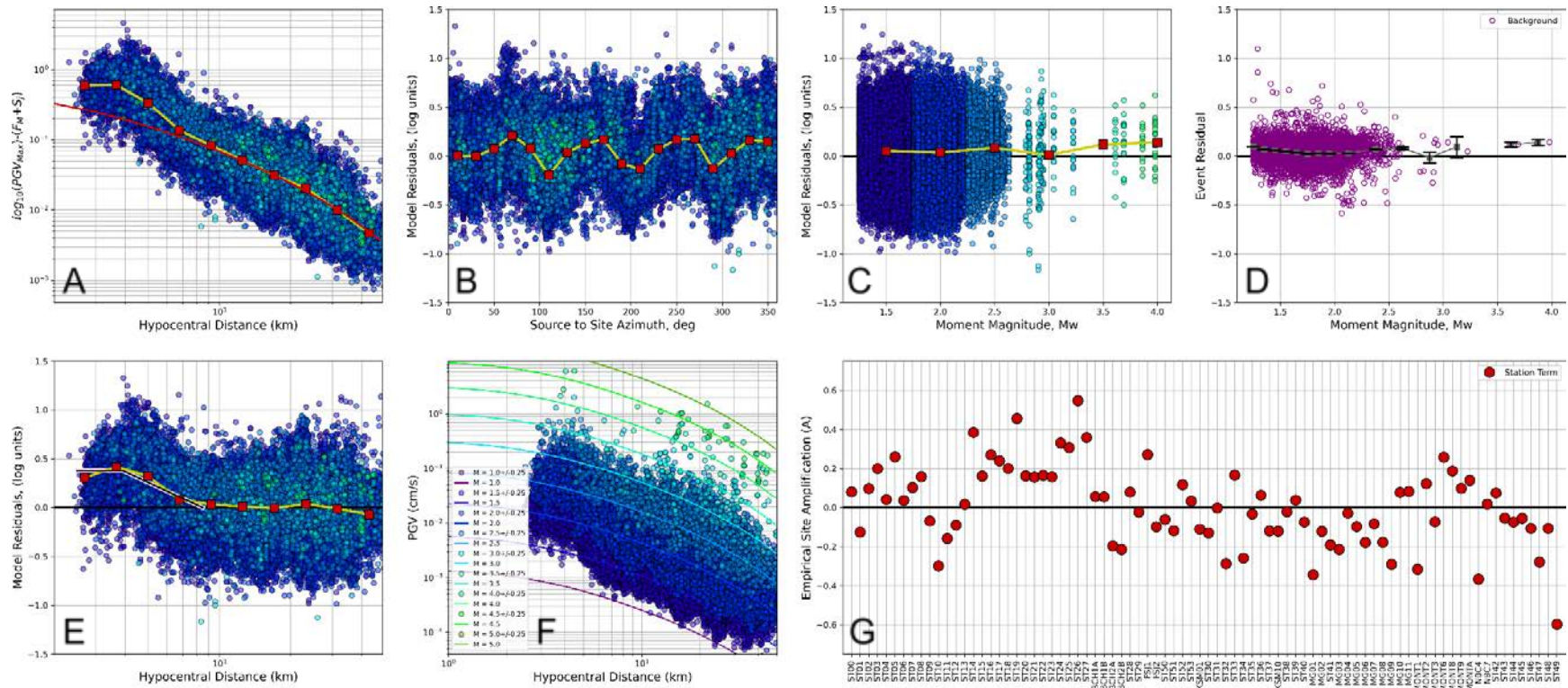


Figure 1-16: Developed GMPE of PGVs and its residuals as function of distance, azimuth, magnitude and station for comparison and residual analyses (Description of the panels given in the text).

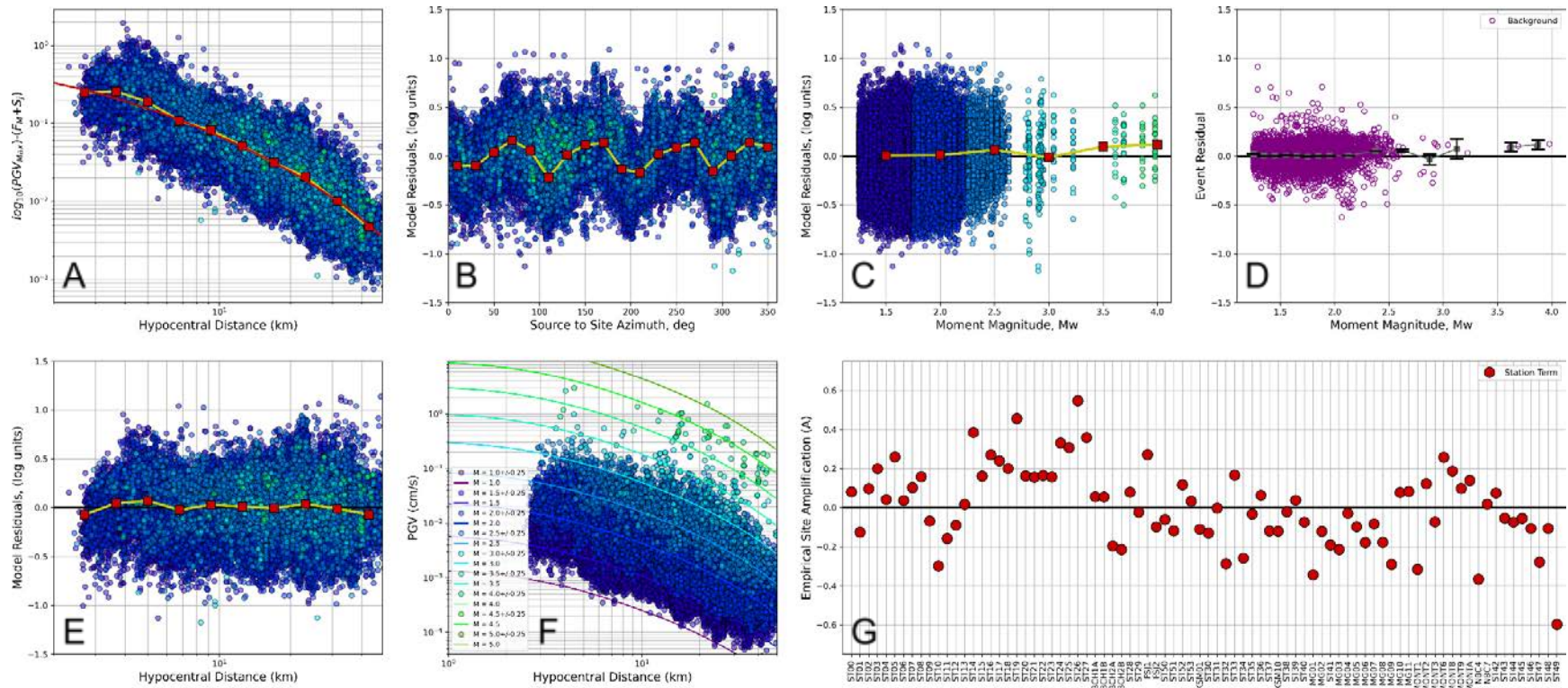


Figure 1-17: Developed GMPE of PGVs after applying Equation 1-13 correction and its residuals as function of distance, azimuth, magnitude and station for comparison and residual analyses (description of the panels are given in the text for Figure 1-17).

1.4.6 Ground-Motion Variability

Ground motions estimated by the derived GMPEs represent the median maximum horizontal component motion. The GMPEs were developed through regression analysis where model predictions carry variability and their standard deviation is represented by parameter σ . There are two component of variability that contribute to recorded ground motion amplitudes (Al Atik et al., 2010):

- Between-event variability (τ):

This includes variations in source attributes of different events (e.g., mechanism, stress drop, rupture size, slip distribution and rate etc.)

- Within-event variability (φ):

This includes variations in wave propagation and site effects for a given event (e.g., radiation pattern, path dependent attenuation directional dependencies, near-surface site effects etc.)

The between-events and within-event standard deviations of the ground-motion model represent the earthquake-to-earthquake variability and record-to-record variability, respectively (Al Atik et al., 2010). The between-events and within-event residuals are uncorrelated, so the total standard deviation of the ground-motion model, σ , can be written as:

$$\sigma = \sqrt{\varphi^2 + \tau^2} \quad (1-14)$$

Figure 1-18 (from Strasser et al., 2009) schematically illustrates between event and within event variabilities for two events with the same magnitude. The data shown is for two events having the same magnitude, which is also the magnitude used to calculate the median of the predictive equation. The between-event variability, τ , characterizes the dispersion of the between-event residuals, δB (one residual per earthquake). Similarly, the within-event variability, φ , characterizes the dispersion of the within-event residuals δW (several residuals per earthquake).

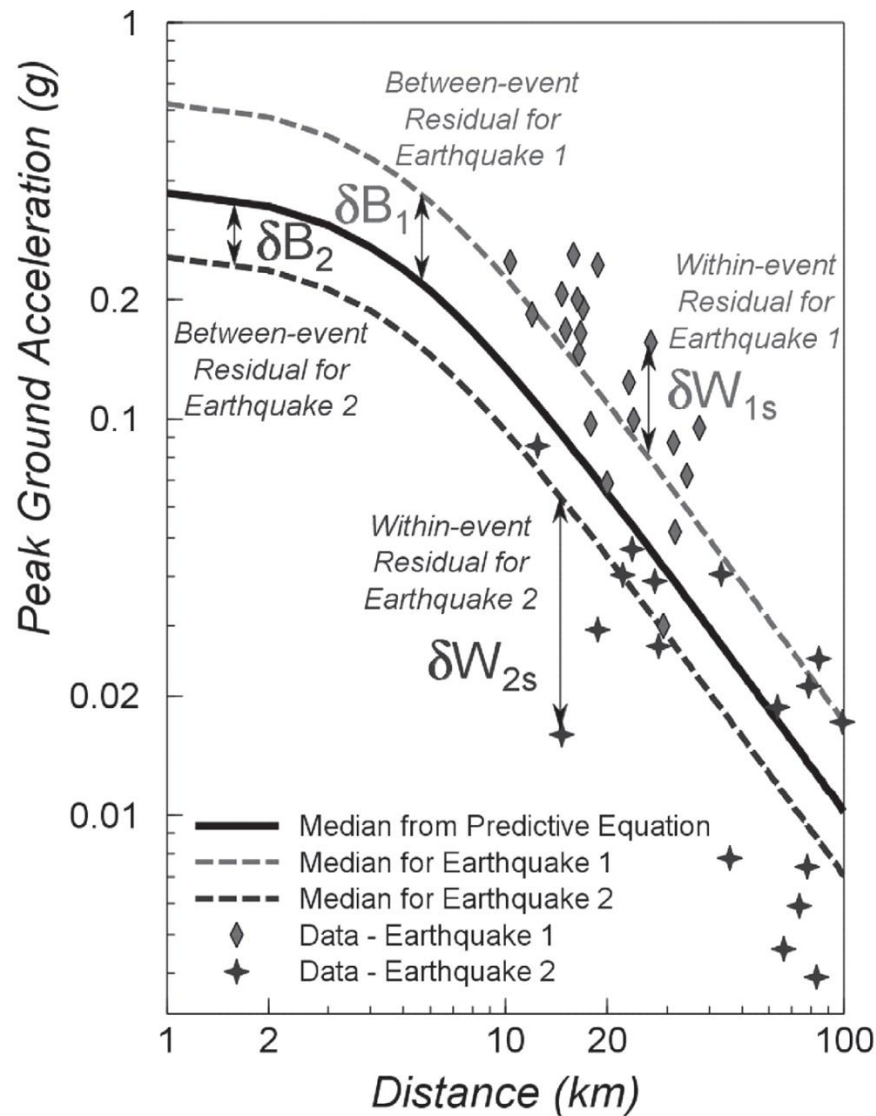


Figure 1-18: Between-event and within-event components of ground motion variability (after Strasser et al., 2009)

In this study residuals between observed and predicted ground motions are examined to determine the between- and within-event variabilities. For each event, residuals from all stations are averaged to calculate the mean event residual that represents the event-specific ground motion offset relative to the median GMPE (δB). Then the standard deviation of all mean event residuals are calculated for both PGA and PGV GMPEs. The

values of the between-event variability (τ) for PGA and PGV are 0.14 and 0.12 \log_{10} units respectively. The plots of event residuals and between-event terms are shown in Figure 1-19. Ground motion residuals are then corrected for event-specific offsets to calculate within-event residuals. Within-event variability (ϕ) is calculated as the standard deviation of all within-event residuals. The values of the within-event variability (ϕ) for PGA and PGV are 0.23 and 0.22 \log_{10} units respectively. Figure 1-20 shows the within-event residuals of all PGA and PGV motions as function of distance as well as the binned averages and calculated within-event variability band. Using the values of τ and ϕ , the total variability value (σ) of GMPEs for PGA and PGV are calculated following the equation 1-14. The values of the total variability (σ) for PGA and PGV are 0.27 and 0.25 \log_{10} units respectively.

As shown above, due to inherent randomness within the earthquake process, and differences in earthquake source parameters (i.e. mechanism, stress drop, rupture size, slip distribution and rate etc.), it is possible that two earthquakes with the same magnitude having occurred in close proximity to one another may result in different ground motions at the surface. The characterization of variability allows for an estimation of a ground motion to occur for some probability level. This is of particular use for estimating the inverse case of what equivalent earthquake magnitude has an unlikely probability of exceeding a defined ground motion level. This will be explored in a later section of this report.

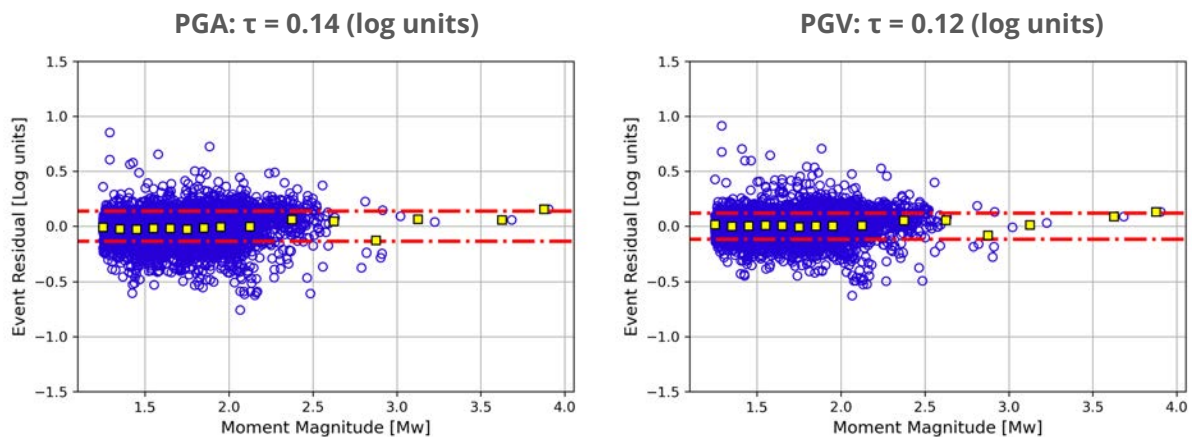


Figure 1-19: Scatter plot of mean event residuals of PGA (left) and PGV (right) as function of magnitude. The yellow squares represent mean values of binned averages and dashed lines show ± 1 -standard deviation band which represents τ .

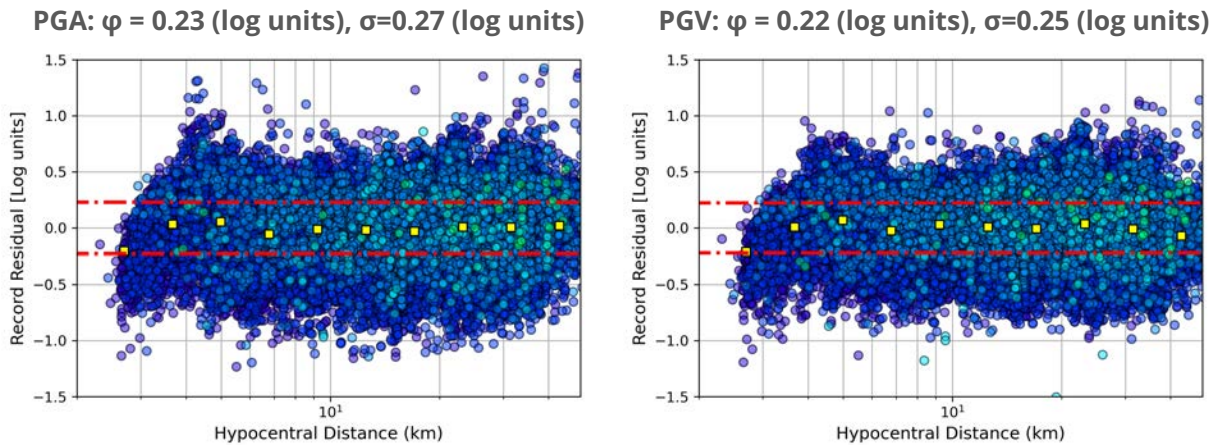


Figure 1-20: Scatter plot of within event residuals of PGA (left) and PGV (right) as function of distance. The yellow squares represent mean values of binned averages and dashed lines show ± 1 -standard deviation band which represents ϕ . The overall values of variabilities are calculated Based on Equation 1-14.

1.5 Site Amplification Mapping

Site amplification at uninstrumented locations requires estimation in order to generate representative shake maps across a region. This requires the development of a site amplification map that captures the spatial variation of near-surface site effects on ground motions across the target region. Empirical site amplifications at recording stations determined through regression analysis in the previous stage are correlated with alternative geological/geotechnical parameters to estimate site effects at uninstrumented locations.

1.5.1 List Of Studies Or Data Related To The Study Area

The following is a list of studies and their associated data sources for study area:

Monahan (2018). Amplification of Seismic Ground Motion Hazard in the Fort St. John – Dawson Creek Area, Northeastern BC. The data and information associated with this study include:

- Database of more than 4800 gamma ray logs, water wells and boreholes are assembled/analyzed for developing depth to bedrock map
- 26 MASW and V_s measurements, surficial geology and seismographic records are used for seismic amplification studies
- The digital database associated with this study included depth to bedrock elevation contours, surficial geology, V_s data and site class maps

Monahan (2016). Mapping the Susceptibility to Amplification of Seismic Ground Motions in the Montney Play Area of Northeast British Columbia. The focus of this study is to create a map of susceptibility to amplification due to local site conditions. The following is the list of data either used or developed by this study:

- Collected surficial geology maps and borehole databases
- V_s measurement
- Developed V_s model for shallow geologic units
- Assigned NEHRP class to surface units

Hickin and Fournier (2011). Energy Open File 2011-2, Compilation of Geological Survey of Canada Surficial Geology Maps for NTS 94A and 93P (1:250,000). The data products of this study are the following:

- Maps of the Montney Play area that depict bedrock topography, drift thickness, and density of bedrock contact point data
- Digital data of 1:1000000 and 1:250000 scale maps

USGS V_{s30} Models and Data (<https://earthquake.usgs.gov/data/vs30/>). This online public source provides a digital database of global V_{s30} values derived from topographic slope. The assumption behind this methodology is that topography with a steeper slope is made up of stiffer materials, where relatively flat areas are associated with softer sediments.

1.5.2 Data Input To Site Amplification Modeling

The sensitivity of site factors derived from GMPE modeling in the previous stage are analyzed against the following parameters: effective depth to bedrock, surficial geology,

site class, and V_{S30} . The data of these parameters are extracted from the above mentioned studies.

Figure 1-21 shows the map of bedrock depth extracted from Monahan (2018) study and is overlain by the locations of sites with calculated site factors in this study. The contour-lines provided by this dataset are grouped into a few depth values with exceedingly unequal intervals (15m, 30m, 100m and 200m).

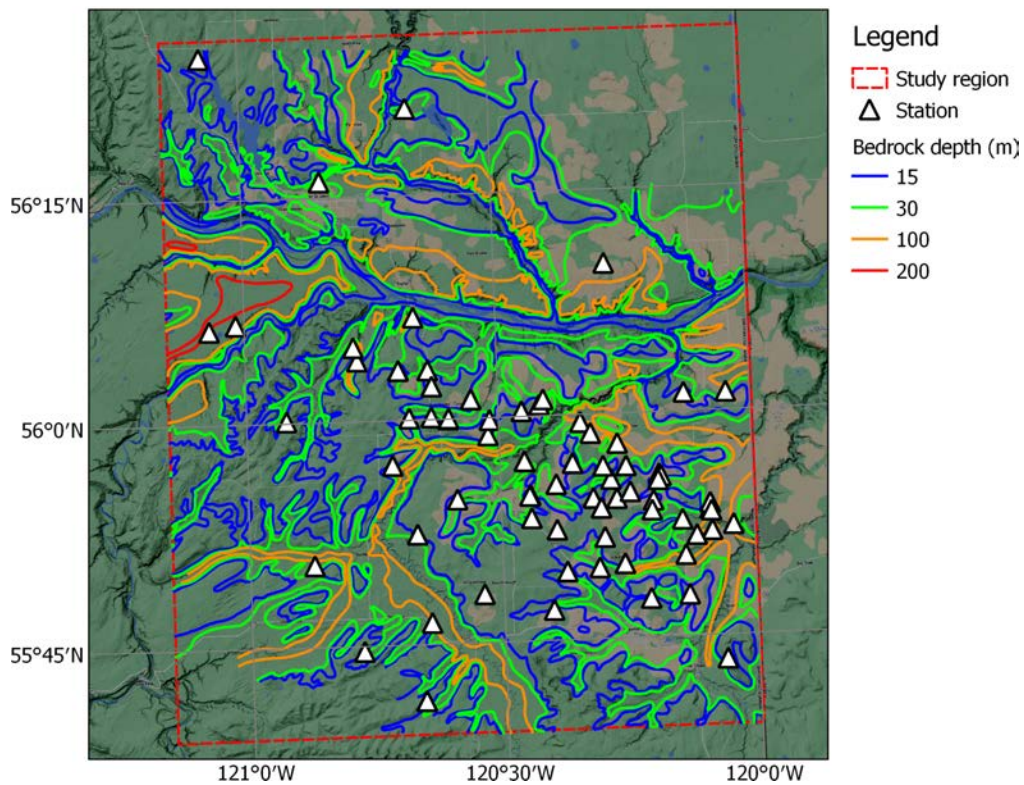


Figure 1-21: Map of depth to bedrock based on Monahan (2018) study. White triangles show the locations of stations with site factors calculated in the derivation of the GMPE model.

Figure 1-22 shows the map of drift thickness (depth to bedrock by Hickin, 2011) study with white triangles showing the locations of sites with calculated site factors. Although the drift thickness of Hickin (2011) shown in Figure 1-22 does not cover the whole study area (enclosed by a red dashed frame), it provides more detailed drift thickness information than Monahan (2018), and is generally consistent with the information provided in the Monahan (2018) study.

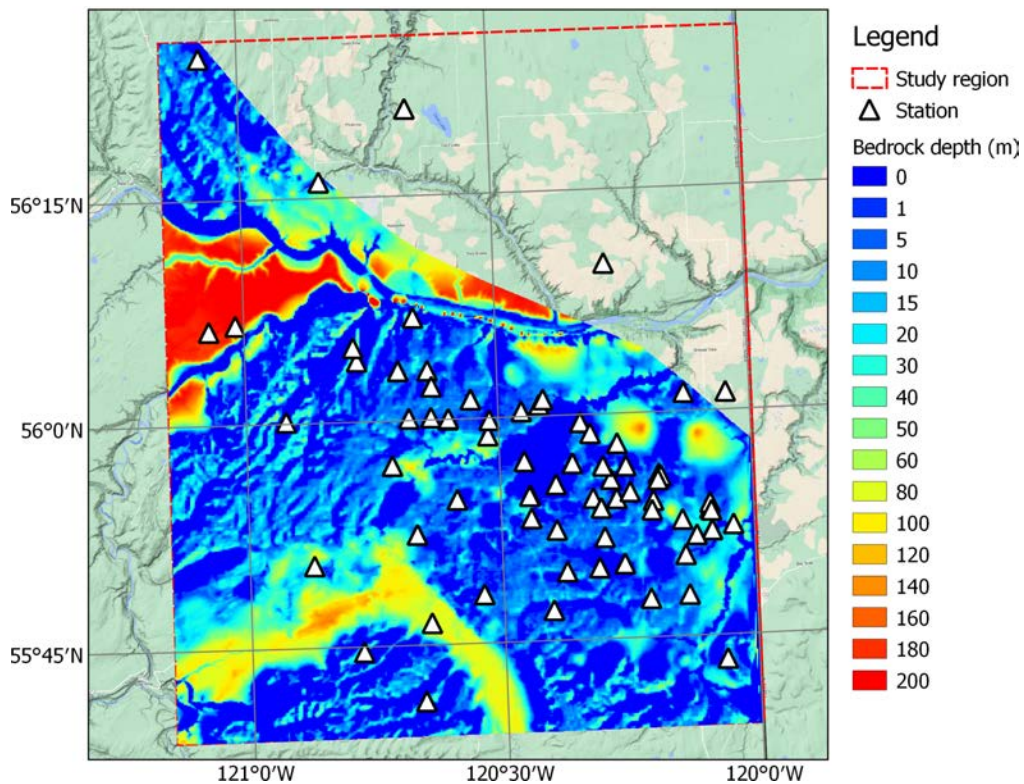


Figure 1-22: Map of depth to bedrock from Hickin (2011) study and the locations of stations with site factors calculated in this study represented by white triangles.

Figure 1-23 shows the surficial geology map of Monahan (2018) study (compiled and revised from maps by Mathews, 1978; Reimchen, 1980; Hickin and Fournier, 2011; and Natural Resources Canada, 2015) and overlain by the locations of sites with calculated site factors in this study.

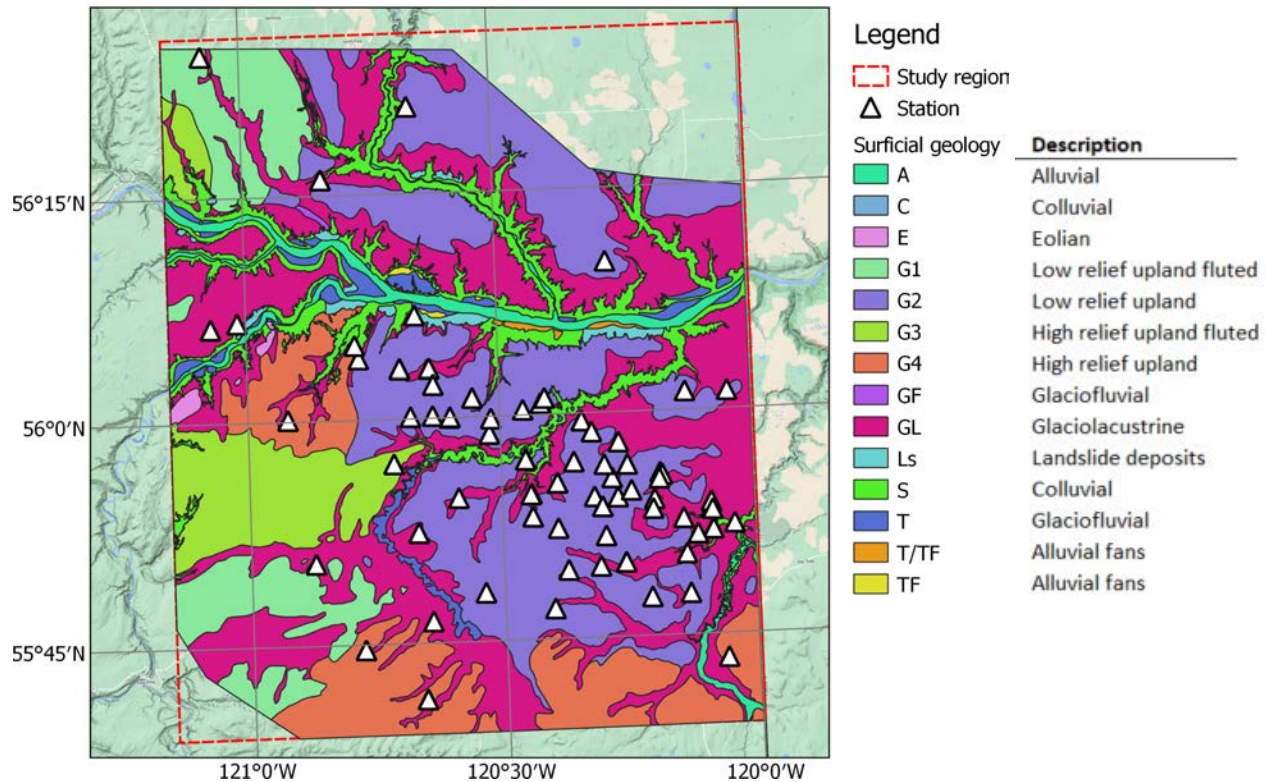


Figure 1-23: Map of surficial geology from Monahan (2018) study. White triangles show the locations of stations with site factors calculated in the derivation of the GMPE model.

Figure 1-24 shows the surficial site classification map of Monahan (2016) study with the overlaying triangles showing the locations of sites with calculated site factors in this study. The majority of seismograph stations sit on site class B-C and D.

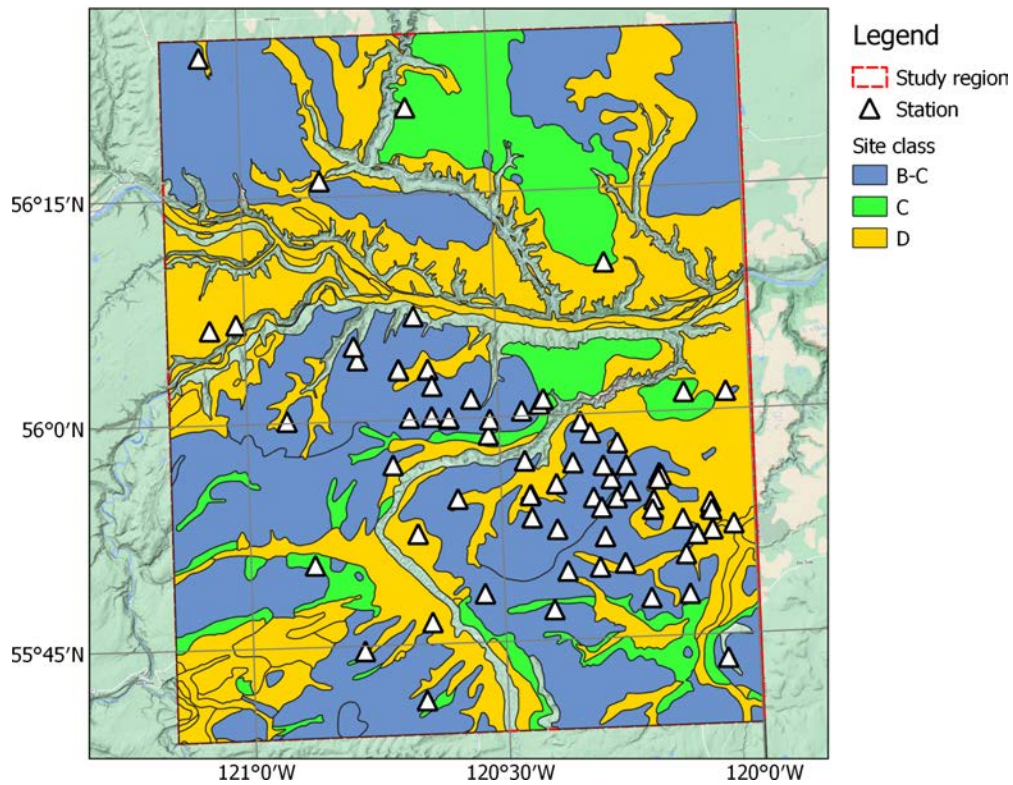


Figure 1-24: Map of surficial site classification from Monahan (2016) study along with white triangles representing the locations of stations with site factors calculated in this study.

Figure 1-25 shows the slope based V_{s30} map from the USGS with white triangles showing the locations of sites with calculated site factors. The USGS slope based V_{s30} model is based on GTOPO30 digital elevation model which assigns elevation to ~500 m by ~900 m tiles along longitude and latitude respectively. Seismograph stations are distributed on sites with estimated V_{s30} ranging from 200 m/s to 900 m/s.

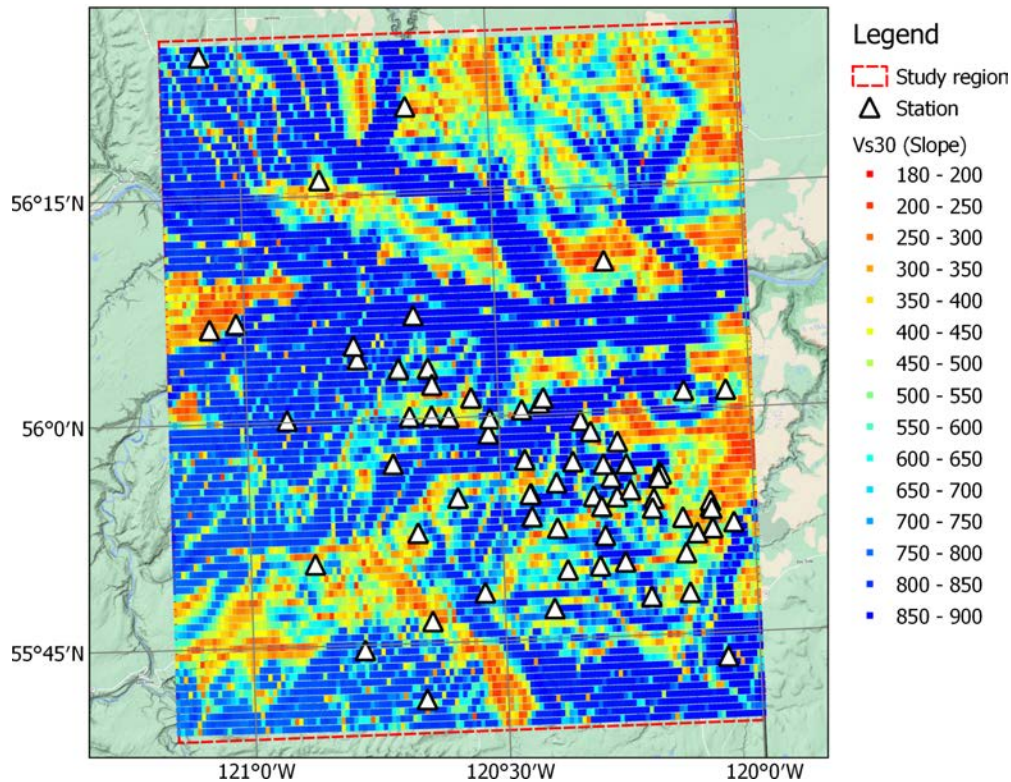


Figure 1-25: USGS's slope based V_{s30} map and the locations of stations with site factors calculated in this study represented by white triangles.

1.5.3 Site Amplification Modeling

Site amplification modeling in the study region is carried out by correlating the site amplification factors at the recording sites derived from the GMPE modeling process with the geological/geotechnical attributes discussed earlier (i.e., depth to bedrock/overburden thickness, surficial geology, surficial site class and V_{s30}). As shown in Figures 1-21 to 1-25 geological/geotechnical information is sampled at each station. Additionally, the sediment thicknesses are corrected for 'effective' thickness by removing the sensor burial depth from

the reported value. In addition geotechnical measurements from water wells, field sites, V_s sites, and petroleum wells compiled in the Monahan study within 150 m from a station are used to refine local site information.

The modeling process of site amplification in terms of geological/geotechnical parameters is carried out in the same manner for both PGA and PGV motions. The empirical site amplification factors derived from regression analysis are plotted as a function of each of the following parameters: effective depth to bedrock, surficial geology, surficial site class and V_{s30} . The data are then analyzed for any existing trends or bias.

Figure 1-26 shows the scatterplot of PGA station terms as function of each of the geological/geotechnical parameters along with recording site names. It is demonstrated that there exists a clear trend between the empirical site terms with depth to bedrock and V_{s30} . Deeper sediments with lower shear-wave velocities are typically associated with higher amplification where sites on more competent materials with shallow sediments and higher shear-wave velocities tend to correlate with relatively lower amplification, or deamplification. As is expected, we observe an increasing trend of site-term with increasing effective sediment thickness as well as decreasing trend in site-terms with increasing shear-wave velocities. The trends are modeled simultaneously following a multivariable regression approach to capture competing effects and are shown as red lines in the figure.

Figure 1-27 shows the site factors of each station, corrected for the effects of the depth to bedrock and V_{s30} , in the same order as shown in Figure 1-26. As a result of site factor corrections there no longer exists any obvious trends relative to effective depth to bedrock and V_{s30} . In panel C of Figure 1-27 the mean deviation of corrected site factors related to each surficial geological unit is shown. Panel D does not show any bias or correlation between the empirical site terms with the estimated NEHRP site classifications made by Monahan (2018). A secondary correction to account for geologic unit types is then captured and applied to the site factors, where updated results are shown in Figure 1-28. In this figure there are no further notable dependence of site factors to the sediment thickness, V_{s30} , geologic unit or site class. Therefore the final model applied to PGA site terms has the following functional form:

$$\log_{10}(A) = 0.105 \times \log_{10}(T) - 0.108 \times \log_{10}(V_{s30}) + C(\text{Unit}) + 0.209 \quad (1-15)$$

with C values for each unit type is:

Unit	Tv	GLp	Tp	Tr	Else
C	0.11	0.022	0.084	-0.124	0

where $\log_{10}(A)$ is the PGA site term, T is the sediment thickness, and C is the constant associated with each geologic unit.

Following the same approach, site terms of PGV are analyzed and modeled in terms of depth to bedrock, surficial geology, surficial site class and V_{S30} . Similar to the PGA case, trends are observed as a function of effective sediment thickness, topographic slope based V_{S30} and surficial geological unit. A set of graphs, similar to those presented for PGA site factors, are produced and shown in the Figures 1-29, 1-30 and 1-31. The final functional form of the PGV site factors predictive relation is:

$$\log_{10}(A) = 0.85 \times \log_{10}(T) - 0.036 \times \log_{10}(V_{S30}) + C(\text{Unit}) + 0.03 \quad (1-16)$$

with C values for each unit type is:

Unit	Tv	GLp	Tp	Tr	Else
C	0.073	0.038	0.017	-0.107	0

where $\log_{10}(A)$ is the PGV site term, and the rest of terms are similar to those of Equation 1-16.

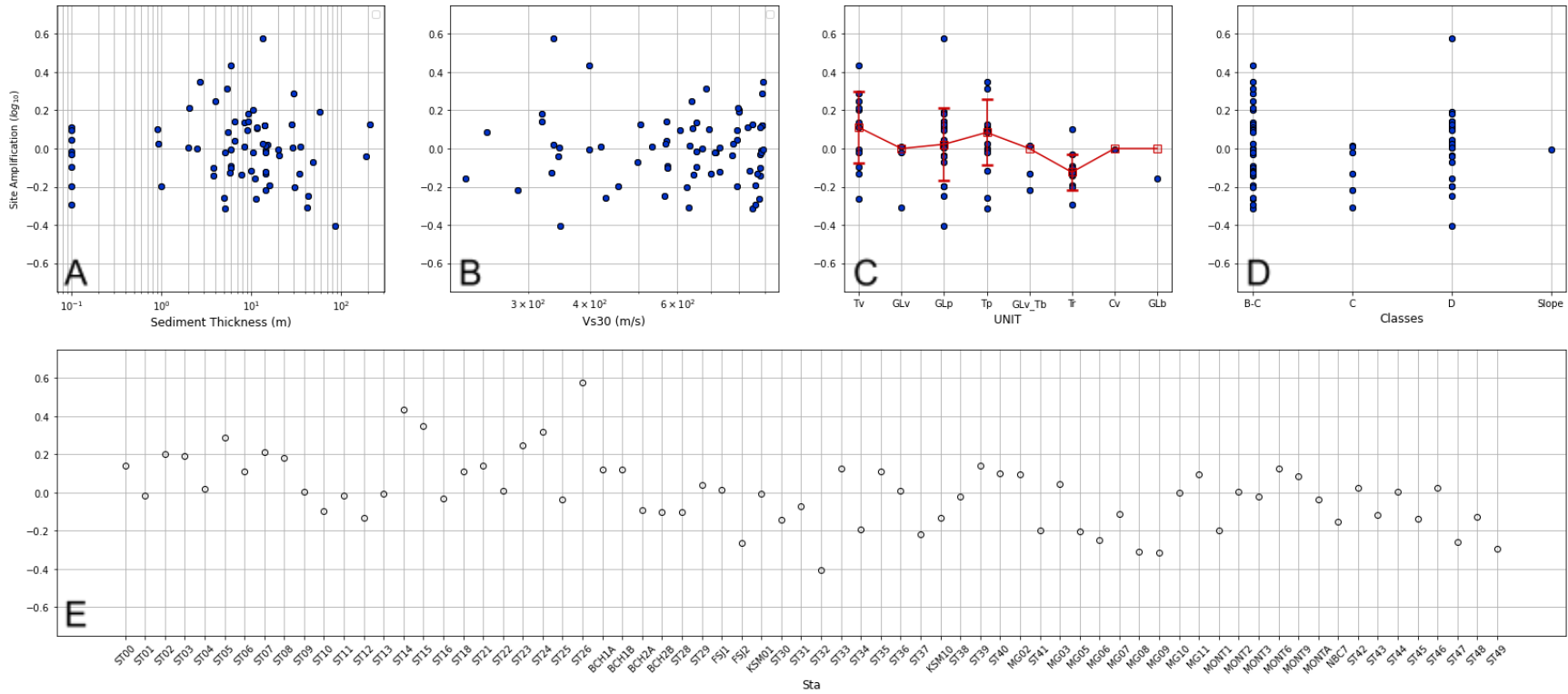


Figure 1-27: Scatter plot of PGA GMPE site terms corrected for sediment thickness and V_{s30} in terms of A: sediment thickness (depth to bedrock); B: V_{s30} ; C: unit (surficial geology); and D: site classes. Panel E provides the PGA site term of each station. Red squares (and the red line) in panel C shows the mean deviation of site factors for each surficial geologic unit.

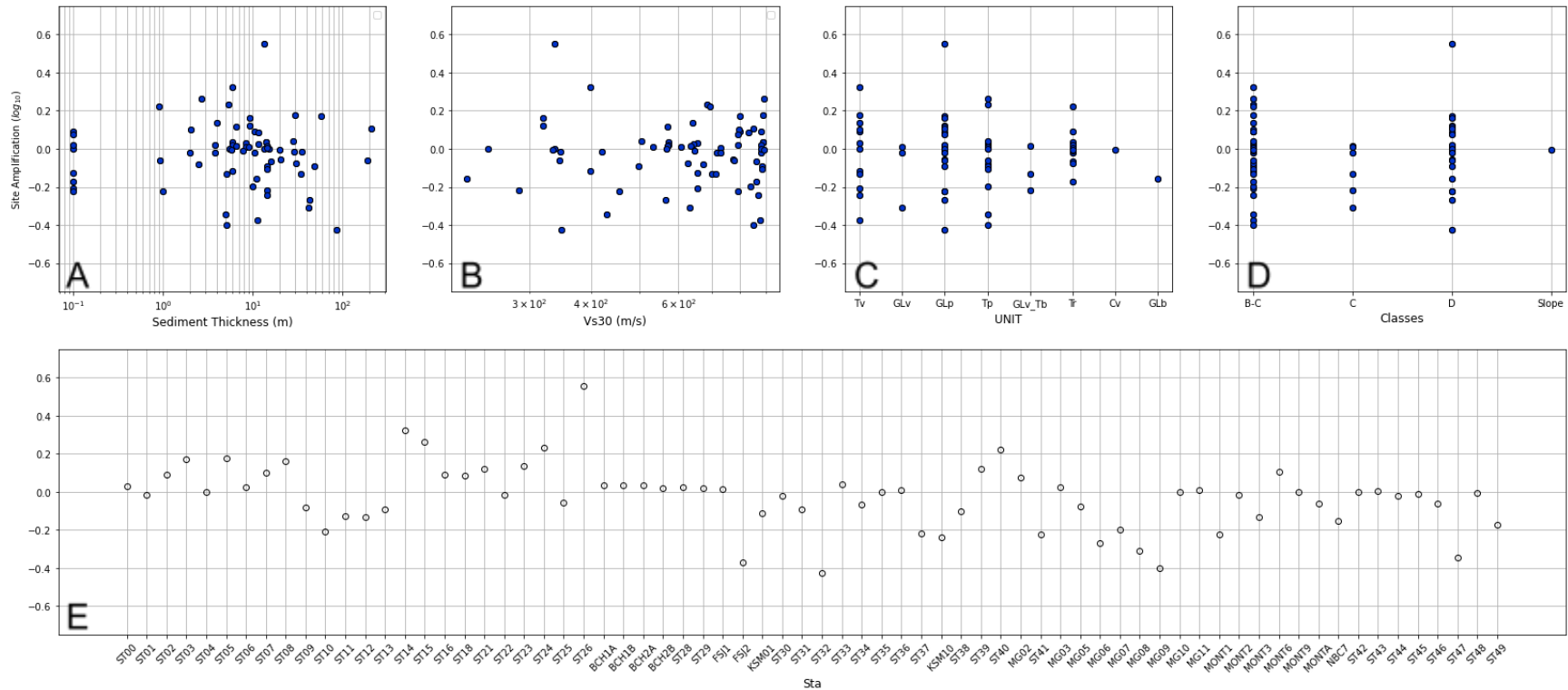


Figure 1-28: Scatter plot of PGA GMPE site terms corrected for sediment thickness, V_{s30} and surficial geologic unit effects in terms of A: sediment thickness (depth to bedrock); B: V_{s30} ; C: unit (surficial geology); and D: site classes. Panel E provides the PGA site term of each station. There is no significant deviation of site terms as function of geological/geotechnical parameters as shown in panels A to D.

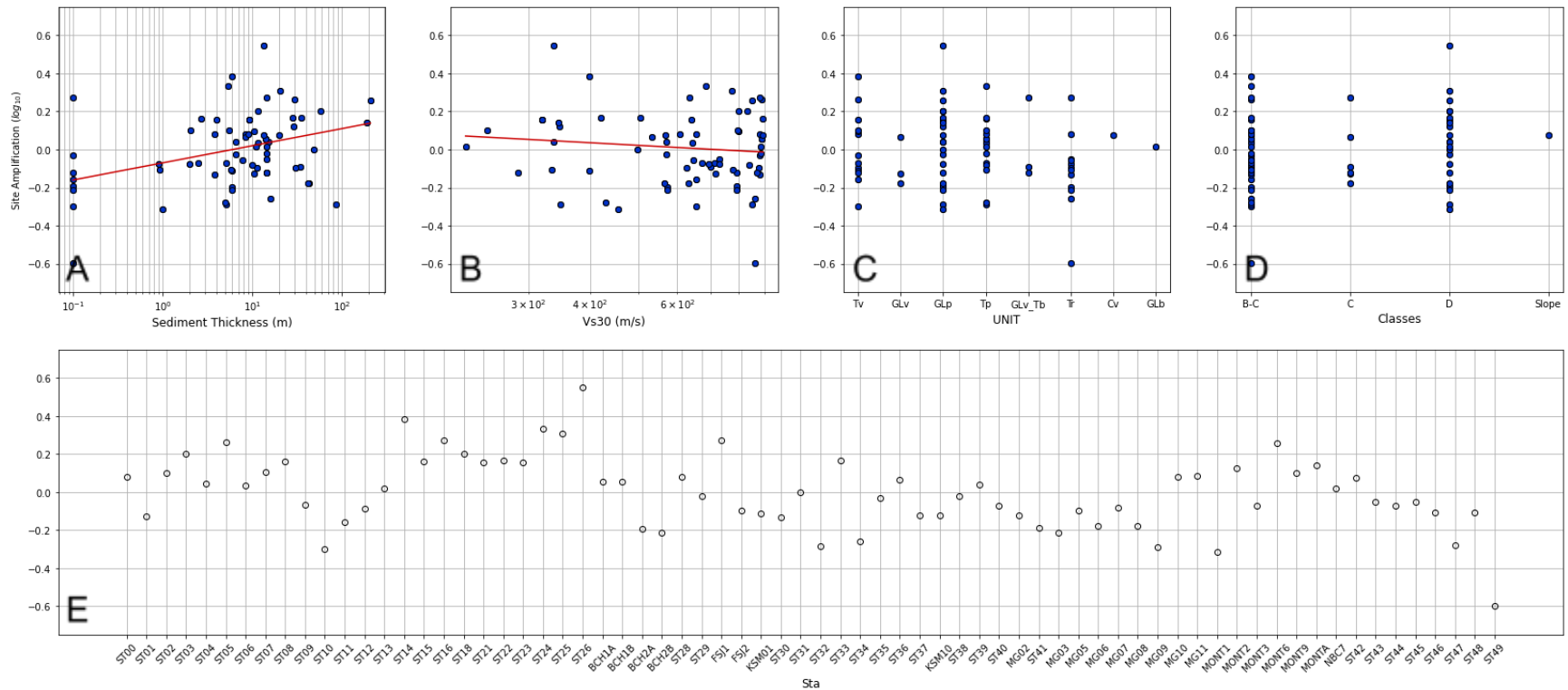


Figure 1-29: Scatter plot of PGV GMPE site terms of each stations in terms of A: sediment thickness (depth to bedrock); B: V_{s30} ; C: unit (surficial geology); and D: site classes. Panel E provides the PGA site term of each station. In panels A and B the red lines show the regression model that best fits the observations.

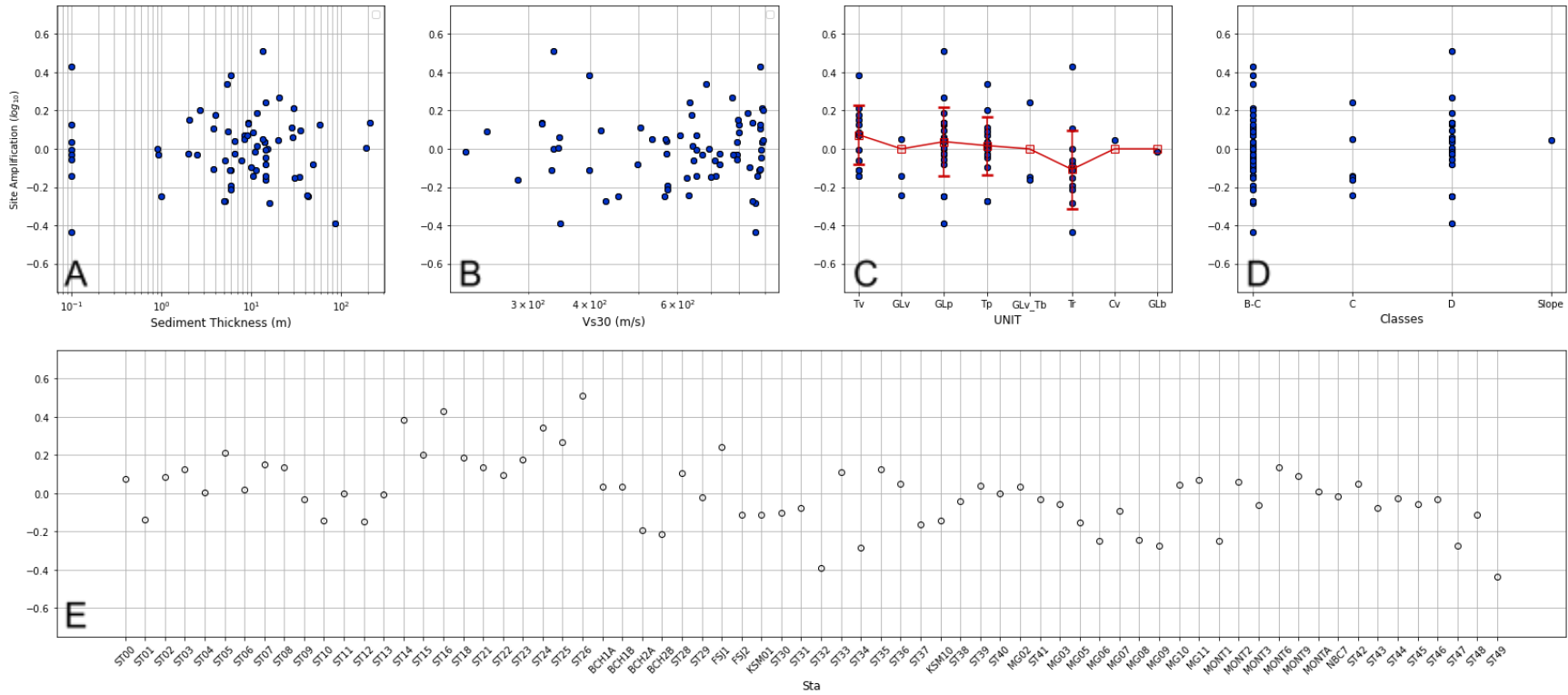


Figure 1-30: Scatter plot of PGV GMPE site terms corrected for sediment thickness and V_{s30} in terms of A: sediment thickness (depth to bedrock); B: V_{s30} ; C: unit (surficial geology); and D: site classes. Panel E provides the PGA site term of each station. Red squares (and the red line) in panel C shows the mean deviation of site factors for each surficial geologic unit.

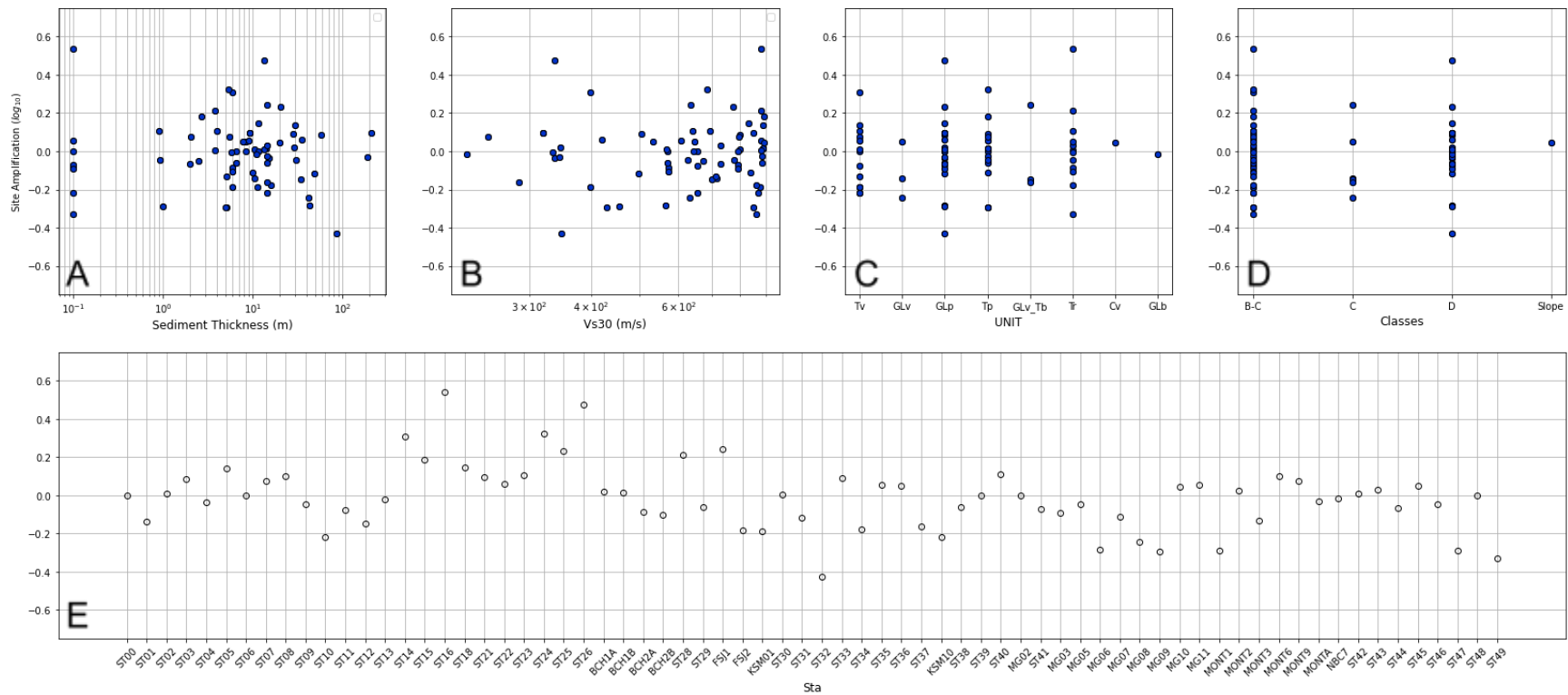


Figure 1-31: Scatter plot of PGV GMPE site terms corrected for sediment thickness, V_{s30} and surficial geologic unit effects in terms of A: sediment thickness (depth to bedrock); B: V_{s30} ; C: unit (surficial geology); and D: site classes. Panel E provides the PGA site term of each station. There is no significant deviation of site terms as function of geological/geotechnical parameters as shown in panels A to D.

1.5.4 Site Amplification Maps

Site amplification maps are developed for both PGA and PGV motions for the study area first by sampling sediment thickness, VS30 and geologic units map layers with grid spacing of 500 m in the GIS platform. Next, the site amplification models are evaluated for the combination of parameters at each grid location to derive the estimated site amplification. Figures 1-32 and 1-33 show the maps of the estimated site amplification grids for PGA and PGV across the study area respectively. The maps clearly associate areas with deeper sediments and lower shear-wave velocities with relatively higher amplifications, and areas with shallower sediments and higher shear-wave velocities with lower amplifications. The derived maps will allow for the incorporation of the localized site effects into the ground-motion estimation to give a more robust representation of the shaking distribution across the region at uninstrumented locations. The site amplifications for PGA and PGV can be found within the "SiteAmp.xlsx" or "SiteAmp.csv" contained in the electronic supplement to this report. The headings include a grid ID ("ID"), the Easting and Northing in NAD83 UTM Zone 11N, Longitude and Latitude, and the Amplification for PGA and PGV in \log_{10} units.

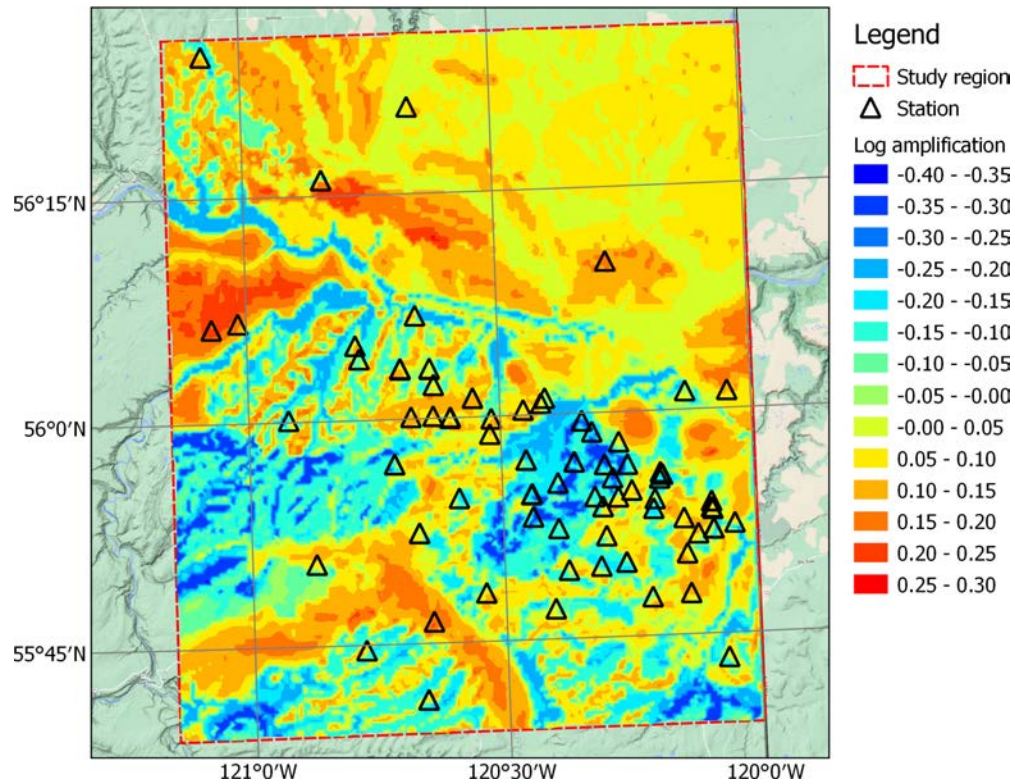


Figure 1-32: Site amplification grid of PGA motions in the study area based on the amplification model developed based on sediment thickness, VS30 and geologic units data. The triangles show the locations of the sites whose data was used for developing the amplification model.

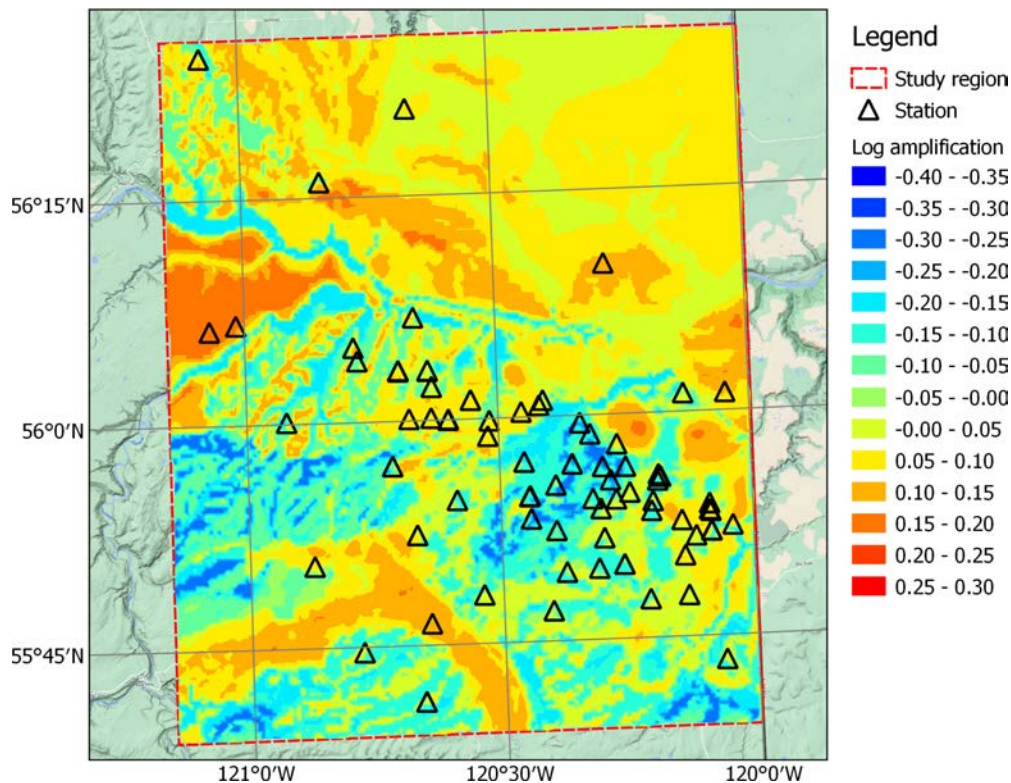


Figure 1-33: Site amplification grid of PGV motions in the study area based on the amplification model developed based on sediment thickness, VS30 and geologic units data. The triangles show the locations of the sites whose data was used for developing the amplification model.

1.6 Shakemaps

Shakemaps show the spatial distribution of shaking intensity across a region due to an earthquake of a given location and size. Shakemaps provide quantitative representation of the ground motion that occurs during an earthquake and are typically generated shortly after an earthquake of concern. These maps help engineers and scientists to assess and visualize the ground shaking intensity and distribution of past or a possible future earthquake. Shakemaps are created for a number of real and scenario cases based on the earthquake source location, the GMPE and site amplification map that were derived in this study.

A scenario shakemap is generated by merging the ground motions estimated from the GMPE for a given magnitude and earthquake location with the regional site amplification grid derived in this study for each grid point across the region (Figure 1-34). PGA and PGV scenario shakemaps are generated for an M4.2 earthquake located at 56.145°N, 120.868°E within the study area, and are shown in Figures 1-35 and 1-36.

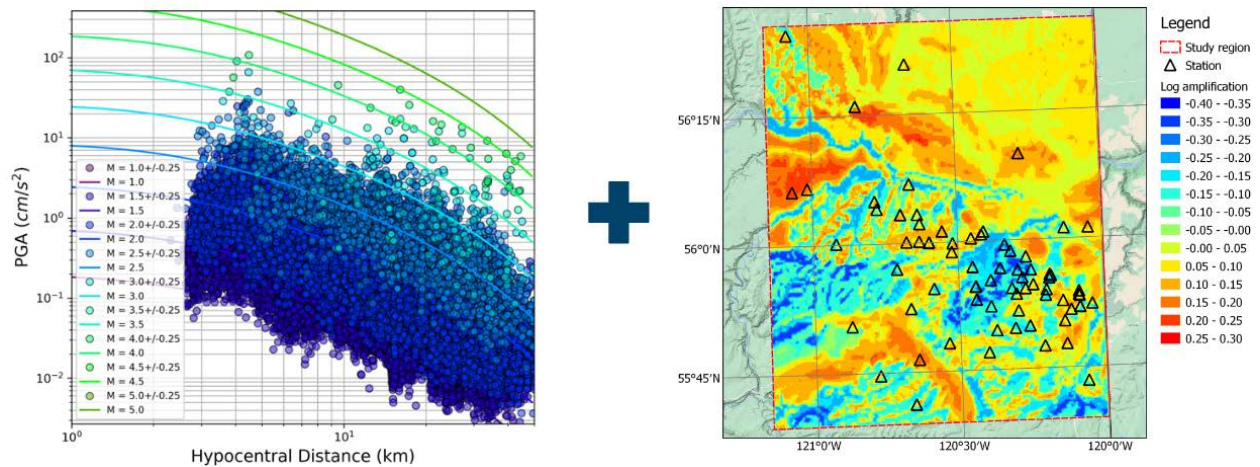


Figure 1-34: Regional models are combined for the generation of shakemaps. Left: regional GMPE model and right: the site amplification grid. For a given earthquake size and location, the GMPE is evaluated and combined with the site amplification for all grid points across the region.

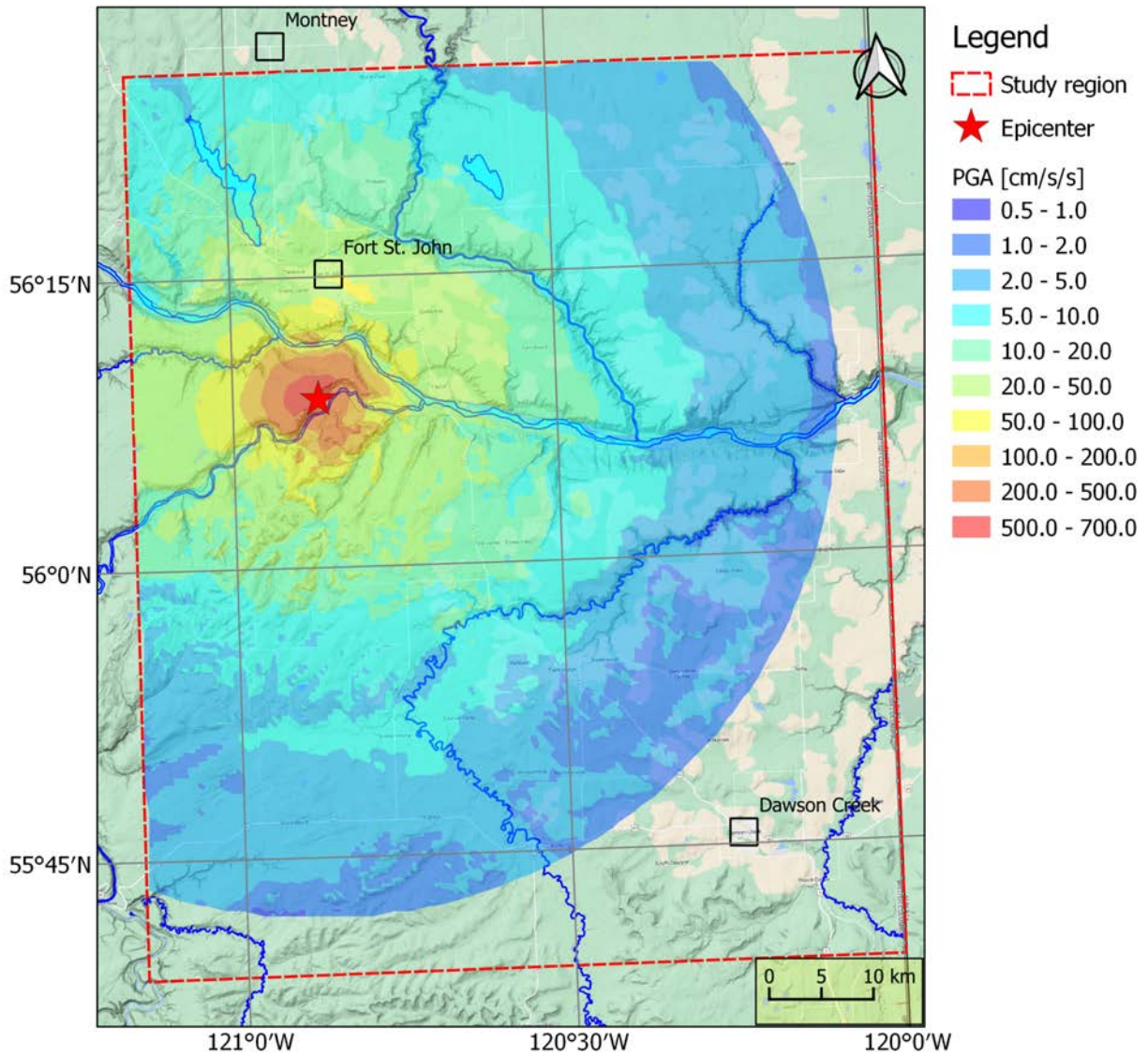


Figure 1-35: PGA scenario shakemap of M4.2 earthquake (56.145°N, 120.868°E) at a depth of 5km.

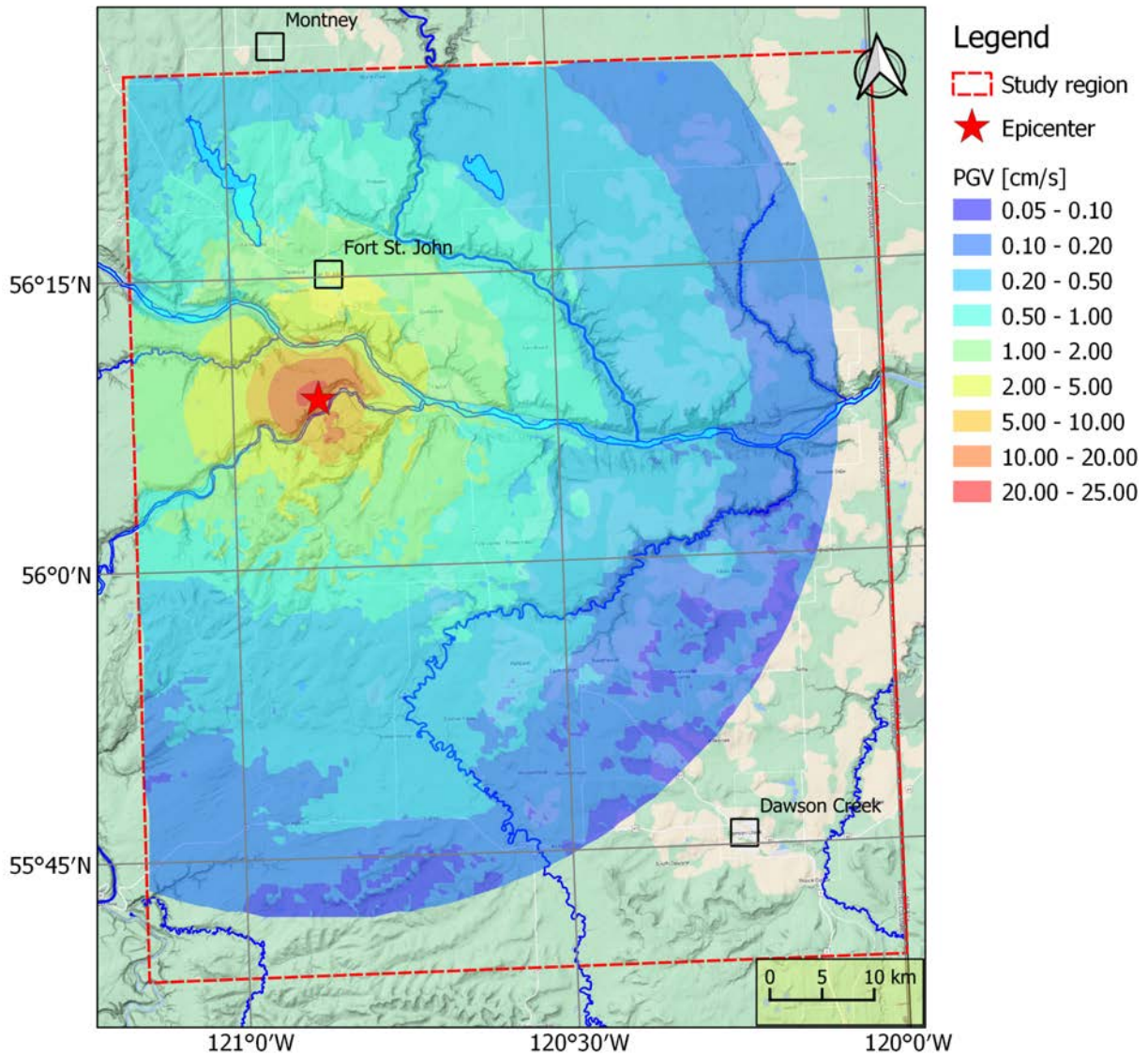


Figure 1-36: PGV scenario shakemap of M4.2 earthquake (56.145°N, 120.868°E) at a depth of 5km.

In the case of real shakemaps, where real earthquake recordings are available in the mapping area, the grid of estimated ground motions are adjusted to incorporate the effects of both individual event's bias, as well as every recording sites' biases, and the generated shakemaps are called assimilated maps. To adjust for the overall event bias (which may be a result of differences in mechanism, slip distribution and rate, stress drop, etc.), the average difference between real recording amplitudes and GMPE predictions, considering site terms at those locations, is determined. The event bias is then added (or

removed) from the grid of predicted motions to adjust the overall predicted amplitude to match the average level of observed motions. For instrumented locations, the ground truth recorded motions are assimilated into the shakemap to further enhance the reliability of the map. These assimilated shakemaps (grid of ground motions) are more robustly determined and are more reliable as they incorporate real recorded amplitudes into the generated maps. Figures 1-37 and 1-38 show PGA and PGV assimilated shakemaps of the Nov. 30, 2018 Fort St. John M3.9 earthquake (56.040°N, 120.691°E at a depth of 1.83km) within the study area. The average event bias for the event is on the order of 0.26 and 0.087 \log_{10} units for PGA and PGV respectively (approximately a factor of 1.8 and 1.01 respectively). The event bias again could be due to differences in source effects that produced relatively higher ground motion content than the average event in the region. The maximum amplitudes recorded were a PGA of 222 cm/s^2 and a PGV 3.38 cm/s at a hypocentral distance of 4 km. The ground motion model estimated a maximum PGA of nearly $\sim 500 \text{ cm/s}^2$ and a PGV of $\sim 8 \text{ cm/s}$ corresponded to a point very close to the epicenter with relatively higher site amplification and a greater influence of the near-distance amplification effect.

Shakemaps for significant events that have occurred through the region are generated. For events more recent than 2017, ground motion data are assimilated, and are referred to as “Real-Event Shakemaps”. For events before 2017, ground motion data were not readily available. These shakemaps are developed based on the resulting median ground motion amplitudes generated by the GMPE combined with the site amplification map, and are referred to as “Scenario Shakemaps”. A number of the historical events had similar magnitudes and occurred in close proximity to one another. To prevent redundancy in the maps generated, earthquakes with similar magnitudes and locations are grouped together as a single representative scenario. Tables 1-3-1 and 1-3-2 list the events with generated shakemaps where the maps may be found in the electronic supplement to this report as part of the “BCOGRIS - Phase 1 ShakeMaps for Significant events” pdf.

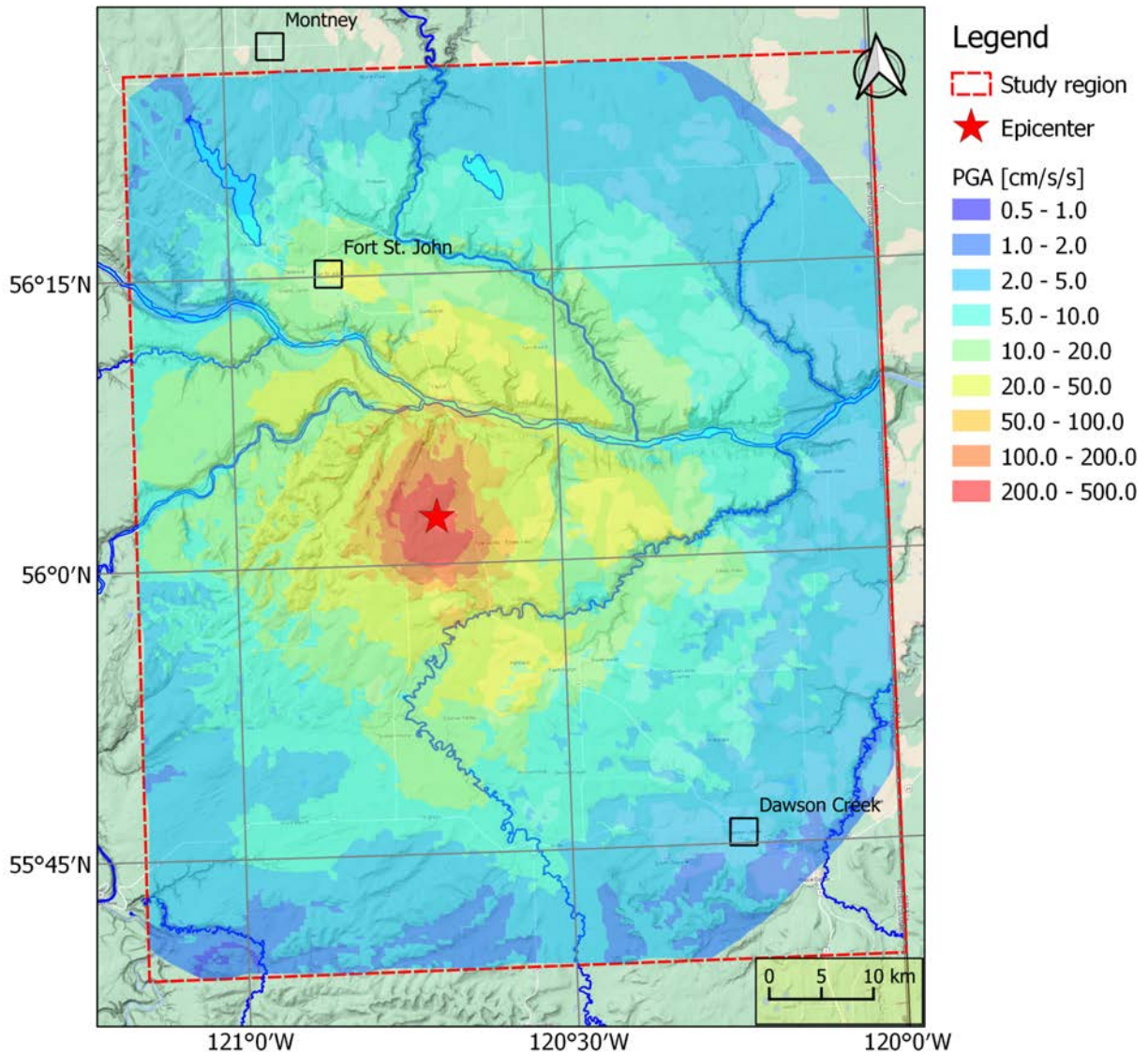


Figure 1-37: PGA of assimilated shakemap of Nov. 30, 2018 Fort St. John M_w 3.9 earthquake (56.040°N , 120.691°E at a depth of 1.83km). The maximum recorded PGA is 222 cm/s^2 at a site in 4 km hypocentral distance.

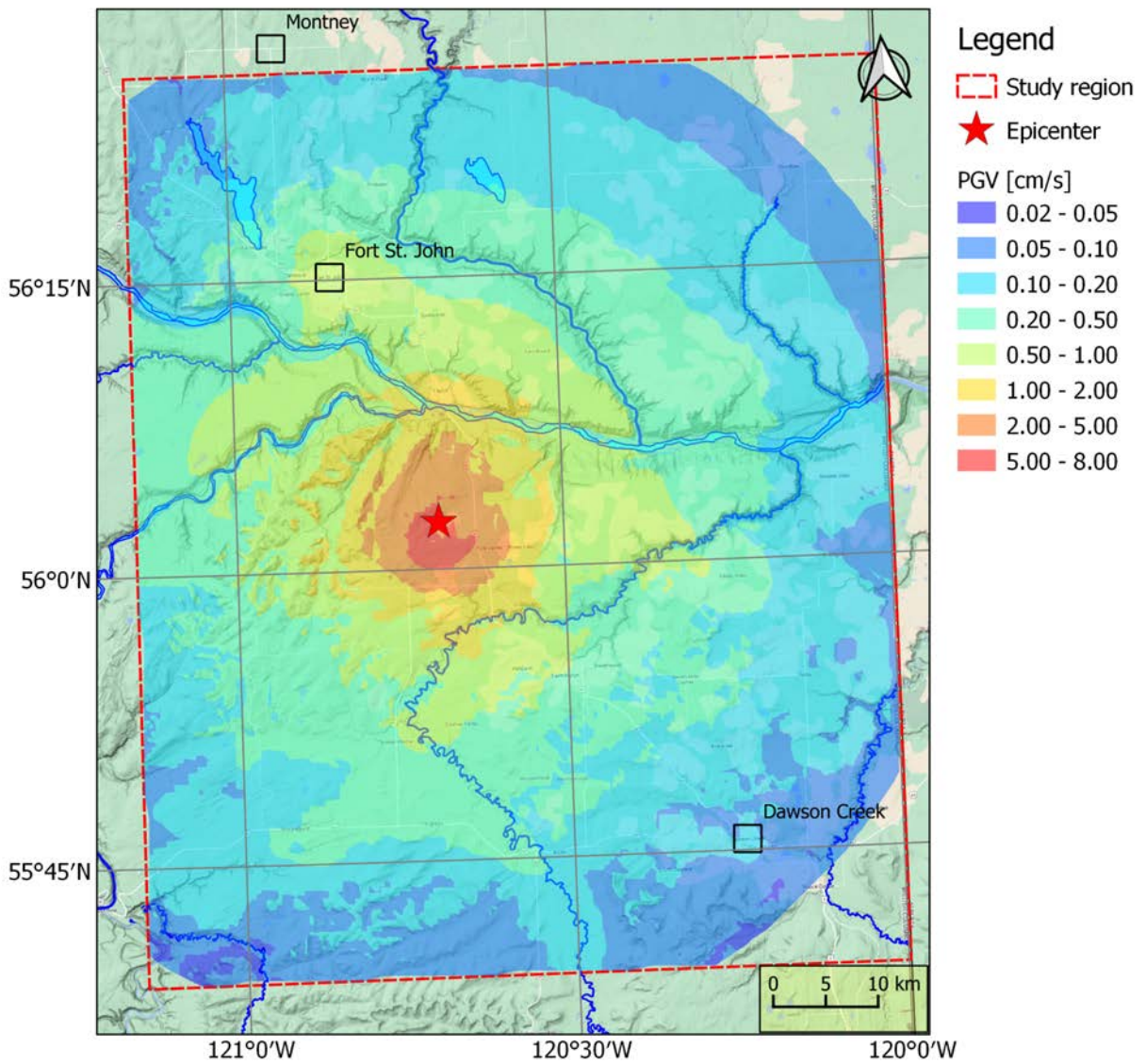


Figure 1-38: PGV of assimilated shakemap of Nov. 30, 2018 Fort St. John M_w 3.9 earthquake (56.040°N , 120.691°E at a depth of 1.83km). The maximum recorded PGV is 3.38 cm/s at a site in 4 km hypocentral distance.

Table 1-3-1: List of events with associated “Real-Event” shakemaps

Origin Time (UTC)	Latitude	Longitude	Catalog Magnitude (M _L)	Moment Magnitude (M _w)	Depth (km)
2018-11-30-02-15-00	56.043	-120.688	4.02	3.68	1.8
2018-11-30-02-06-01	56.042	-120.700	3.43	3.22	1.5
2018-11-30-01-27-06	56.045	-120.692	4.38	3.90	1.6
2019-10-08-13-44-03	55.895	-120.396	3.22	2.81	1.8
2019-10-05-09-07-17	55.895	-120.397	3.34	3.02	1.8
2020-09-11-22-37-27	55.893	-120.386	3.28	2.92	2.0
2021-08-21-14-47-56	56.027	-120.694	3.00	2.91	2.0
2021-07-26-09-32-03	56.059	-120.843	3.74	3.42	1.2
2021-01-25-06-07-09	56.020	-120.690	2.94	2.81	2.0

Table 1-3-2: List of “Scenario” earthquakes

Scenario ID	Latitude	Longitude	Catalog Magnitude	Catalog Magnitude Type	Estimated Moment Magnitude (M _w)	Depth (km)
1	56.271	-120.830	3.00	ML	2.64	1.7
2	56.145	-120.868	4.20	Mw	4.20	1.7
3	56.346	-120.891	3.20	ML	2.82	1.7
4	56.416	-120.774	3.20	mbLg	3.25	1.7
5	56.391	-120.738	3.70	mbLg	3.75	1.7
6	56.272	-120.688	3.10	ML	2.73	1.7
7	56.290	-120.786	4.20	Mw	4.20	1.7
8	55.902	-120.366	3.10	CML	2.73	1.7

1.7 Chapter Conclusion

Ground motions resulting from induced seismicity across the Kiskatinaw region are characterized. First, a ground motion dataset was compiled using data from public and private seismic networks. Next, attenuation was inspected in the Fourier domain in order to correct ground motion recordings for a seismic event to the source, and perform displacement spectral fitting to calculate the moment magnitude, stress drop and other source parameters. A model relating the moment magnitude with stress drop was developed along with a crustal amplification model from the regional velocity model in order to perform earthquake simulations, which help guide the scaling of earthquake magnitudes in magnitude ranges where data are sparse. Next regression analysis was performed to develop a regionally calibrated ground motion prediction equation which accounts for the scaling of earthquake ground motions with respect to magnitude, path (attenuation) and site effects. As the ground motion prediction equation is defined for the median ground motion level, there is a 50% chance for a ground motion recorded at a station for a given magnitude event to exceed the estimated value. To this end, the between-event, within-event and total variability of ground motions are captured, which allows a user to consider alternative percentiles of motion and investigate different probability levels of a given earthquake scenario to exceed a specific ground motion level. Geological and geotechnical information available across the region is correlated with empirical site amplification effects from the regression in order to develop a site amplification model which can be used to further improve the ground motion estimates by considering localized variations across the region. Finally, shakemaps for a number of significant earthquakes which occurred in the region are developed and provided in the electronic supplement to this report.

2. Phase 2 - Perception and Damage Ground Motion Thresholds

2.1 Introduction

Ground motions resulting from an earthquake, whether natural or induced, has the potential to cause nuisance or, if strong enough, damage to homes, buildings, infrastructure or engineered systems. It is important to understand ground motion thresholds associated with different levels of impact at the surface. Ground motion intensity conversion equations (GMICE) are useful to relate reported experiences during a seismic event, with the intensity levels are defined as Modified Mercalli Intensity (MMI), to recorded (or estimated) ground motions through the analysis of “Did you feel it?” reports.

The human perception threshold to ground shaking is the minimum level of vibration or movement of the ground that a human can detect or perceive. The damage threshold of ground shaking is the minimum level of ground motion that can cause damage to a building, infrastructure or other engineered systems. The damage threshold varies depending on the type, size, and age of the structure, as well as the characteristics of the ground motion, such as peak amplitude, frequency content and duration. Damage can typically be defined into two broad categories: non-structural damage and structural damage (Onur and Seemann, 2004; Onur et al., 2008).

The non-structural damage threshold to ground shaking is the minimum level of ground motion that can cause visible damage to non-structural building elements, such as finishes, plaster, tiles, or non-load bearing walls. This threshold is typically defined as the level of peak ground motion that is sufficient to cause cracking, chipping, or detachment of these non-structural elements, but without compromising the overall safety of the building.

The structural damage threshold to ground shaking is the minimum level of ground motion that can cause damage to the load-bearing elements of a structure, such as beams, columns, walls, and foundations and compromises integrity and safety of the structure.

The aim of this section is to determine appropriate felt and damage ground motion thresholds to guide the BCER in the refinement of traffic light protocols throughout the Kiskatinaw region. A literature review is performed to determine perception and potential damage thresholds, as well as identify appropriate GMICEs for the region. Ground motion amplitudes (both recorded and predicted by shakemaps) are associated with felt reports in

the study area and are used to verify the thresholds selected from the literature. The selected GMICE is also used to convert the PGA and PGV shakemaps to Modified Mercalli Intensity (MMI) maps, which can be used to more readily identify areas which ground motions may be perceived or where ground motions have potentially exceeded damage thresholds for some structures.

2.2 Ground Motion Perception Levels

The human perception threshold to ground shaking is the minimum level of vibration or movement of the ground that a human can detect or perceive; however, there are many other human perception levels such as unpleasant, intolerable and so on. In our review of the literature we find that these levels are described based on source type (blast, traffic, pile-driving, etc) as well as motion type (pulse like or steady state, and velocity or acceleration). The following subsections present the findings of the literature review.

Bommer et al., (2006) reviewed a number of standards, codes and publications to identify how vibrations are characterized and how the perception thresholds are specified. Their study summarized three different sets of guidelines that specified thresholds in terms of peak ground velocity and demonstrated the classifications as function of source type. Figure 2-1 shows classification of human perception levels to ground shaking due to three different source types: the US Army Engineering Manual EM 1110-2-3800 (USACE, 1972) for acceptable motions due to blasting in the left panel; the vibration tolerances for traffic-induced vibrations developed by Barneich (1985) and presented by New (1990) in the middle panel; and the paper by Athanasopoulos and Pelekis (2000) dealing with pile driving in the right panel. From blasts, perception is on the order of 0.1 cm/s; where for traffic the perception level is on the order of 1 cm/s; and for pile-driving, the perception level is on the order of 0.1 cm/s.

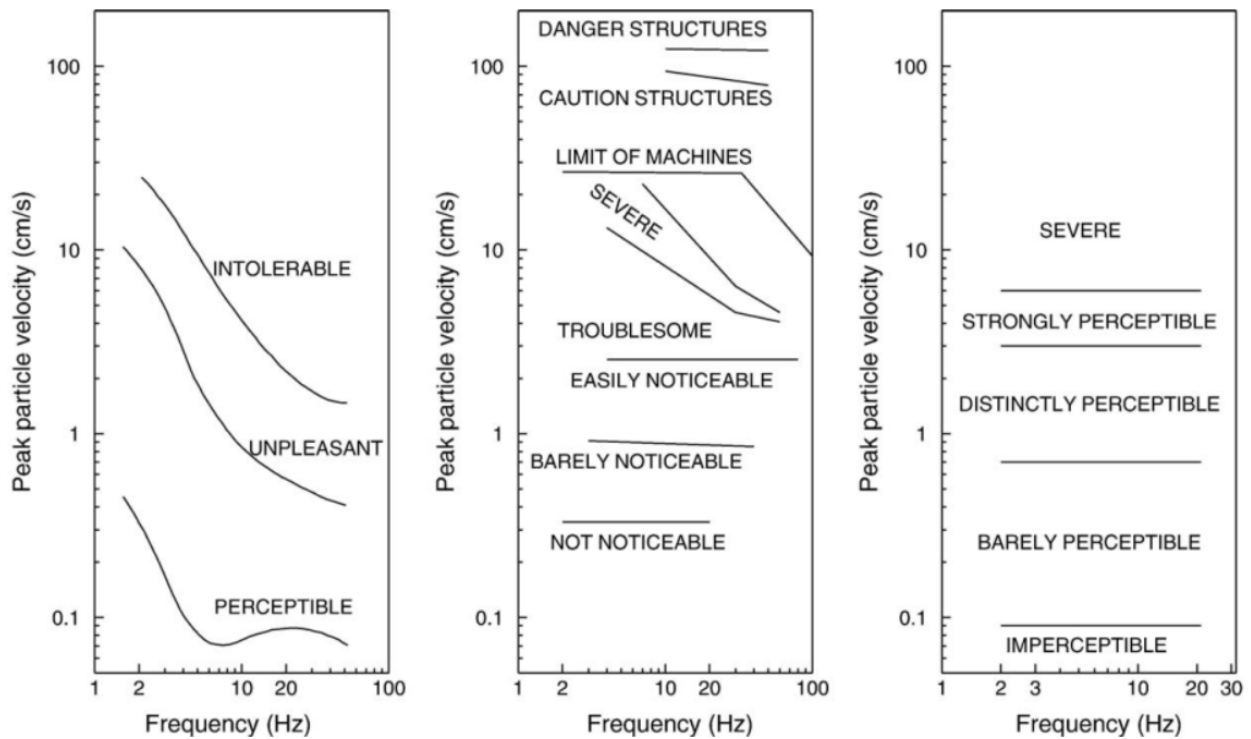


Figure 2-1. Left: recommended levels of human sensitivity to vibration due to blasting from the USACE (1972); middle: reference levels for vibration perception and response from traffic, adapted from Barneich (1985); right: thresholds for vibrations due to pile-driving from Athanasopoulos and Pelekis (2000). From Bommer et al., (2006).

Athanasopoulos and Pelekis (2000) reviewed a number of publications and standards for provisions and recommendations and analyzed vibrations due to sheet pile driving in regards to limiting values of continuous vibration and transient motion intensity for different levels of human perception and discomfort. Their study finds that the threshold values in terms of particle velocity and displacement decrease with increasing values of the frequency of vibration, however, the threshold values with reference to acceleration increase with increasing frequency. In addition they find that the spikiness or continuity of the vibrations affect the values of motion (for example values of PGV) that specify different threshold or perception levels. Figure 2-2 extracted from Athanasopoulos and Pelekis (2000) study summarizes abovementioned findings. In this study we assume ground motions due to induced earthquakes are typically short in duration and are more pulse-like transient vibrations, therefore the perception threshold considered in terms of PGV is on the order of ~ 0.08 cm/s based on panel “c” of Figure 2-2.

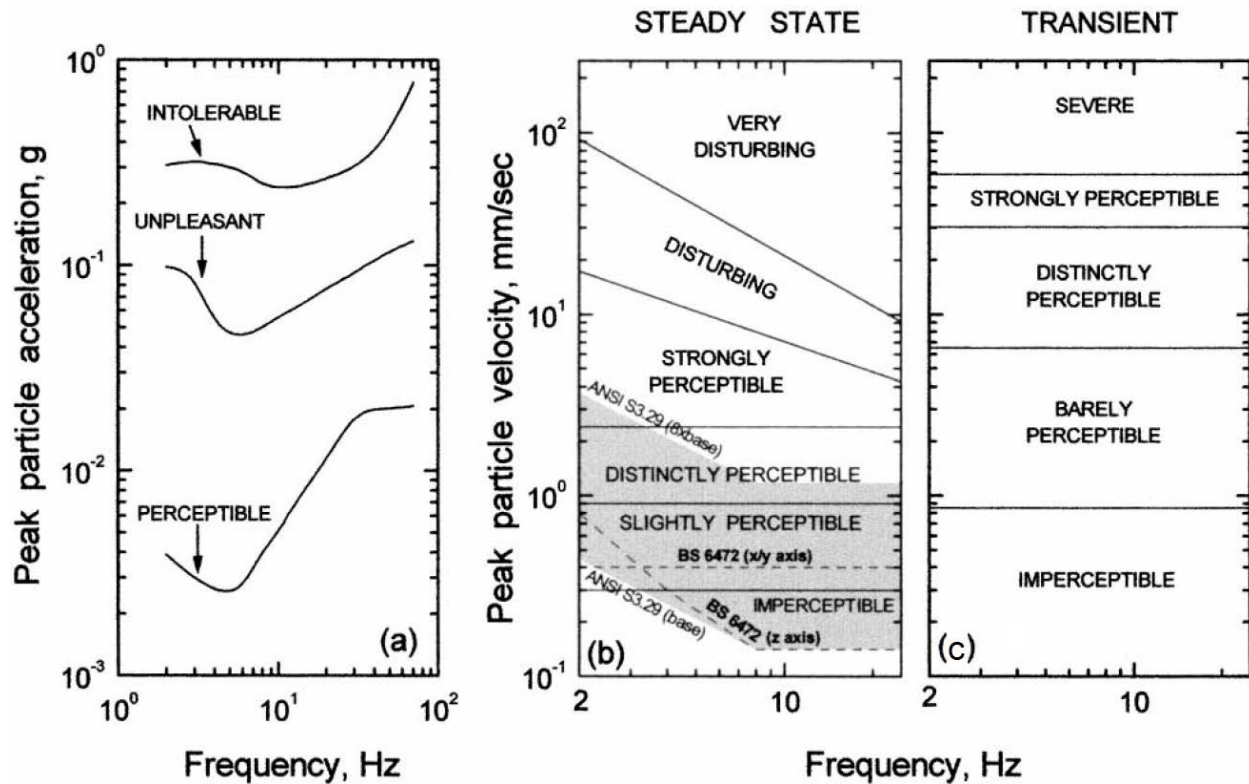


Figure 2-2. Ground motion values associated with different perception levels for PGA (panel a) and PGV (panels b and c) as function of frequency. Panels 'b' and 'c' compare motion levels of separate perception levels due to continuous (panel b) and pulse like (panel c) vibrations. (Modified from Athanasopoulos and Pelekis (2000))

The intensity of an earthquake at a location is a number that characterizes the severity of ground shaking at that location by considering the effects of the shaking on people, on man made structures, and on the landscape (Dewey et al., 1995). Over time several intensity scales have been developed and implemented. In addition, the developed intensity scales have been subject of research studies, for example, Murphy and O'Brien (1977) compared a number of scales against each other and provided one of the earliest correlation relations between PGA and intensity. Since 1973, USGS has adopted the Modified Mercalli Intensity (MMI) scale (Wood and Neumann, 1931) for assigning intensity numbers to the earthquake ground motion effects. According to Dewey et al., (1995) the reasons for popularity of MMI scale is that: 1-the experience has shown MMI's criteria for representing severity of ground

shaking are more reliable than other scales and 2-as construction methods have changed appreciably since the introduction of MMI, amendments and modifications have been developed to MMI criteria listed in Stover and Coffman (1993).

The MMI value assigned to a specific site after experiencing an earthquake effect is described in Table 2-1 (USGS). The lower numbers of the intensity scale (I - V) generally deal with the manner in which the earthquake is felt by people. The higher numbers of the scale (VI - X) are based on observed non-structural and structural damage. Structural engineers usually contribute information for assigning intensity values of VIII or above (Onur and Seemann, 2004; Onur et al., 2008).

Intensity is a more direct descriptor of the severity of ground shaking and its effect on humans and buildings than peak motions like PGA. The effect of ground motions to humans and objects is a function of peak motion, duration and frequency content of the motions therefore a single one of these parameters (such as PGA) will be unable to capture the full effect of the ground motions. As induced earthquakes are usually small-to-moderate magnitude events, they are short in duration and usually rich in high frequency motion content. Thus peak motions (such as PGA and PGV) are the main parameters that drive the intensity of induced earthquakes motions.

Table 2-1. Table of MMI values associated with earthquake effects (USGS: <https://www.usgs.gov/media/images/earthquake-intensity-scale>)

Earthquake Intensity Scale

Modified Mercalli Intensity (MMI)

	INTENSITY	SHAKING	DESCRIPTION
	I	Not Felt	Not felt except by a very few under especially favorable conditions.
	II	Weak	Felt only by a few persons at rest, especially on upper floors of buildings.
	III	Weak	Felt quite noticeable by persons indoors. Many people do not recognize it as an earthquake. Standing cars may rock slightly, vibrations are similar to a passing truck.
	IV	Light	Felt indoors by many, outdoors by few. At night, some are awakened. Dishes, windows, and doors are disturbed. Sensation like a heavy truck striking a building. Standing cars rock noticeably.
	V	Moderate	Felt by nearly everyone; many awakened. Dishes and windows are broken. Unstable objects are overturned. Pendulum clocks may stop.
	VI	Strong	Felt by all; many frightened. Some heavy furniture moved. A few instances of fallen plaster. Damage is slight.
	VII	Very Strong	Negligible damage to buildings of good design/construction. Slight to moderate damage in well-built/ordinary construction. Considerable damage in poorly built/ordinary structures. Some chimneys broken.
	VIII	Severe	Slight damage to specially designed structures. Considerable damage to ordinary construction, including partial collapse. Damage is great in poorly built structures. Fall of chimneys, columns, monuments, and walls. Heavy furniture overturned.
	IX	Violent	Considerable damage to specially designed structures; well-designed frame structures are thrown out of plumb. Damage is great in substantial buildings, with partial collapse. Buildings shifted off foundations.
	X+	Extreme	Some well-built wooden structures destroyed; most masonry and frame structures with foundations are destroyed. Rails are bent.

2.3 Ground Motion Damage Levels

The damage threshold of ground shaking is the minimum level of ground motion that can cause damage to a building, infrastructure or other engineered systems. The damage threshold varies depending on the type, size, and age of the structure. Moreover, different elements of structures will react differently to the ground motion loads due to their strengths. Therefore the damage threshold can be divided into non-structural damage threshold and structural damage threshold.

The non-structural damage threshold to ground shaking is the minimum level of ground motion that can cause visible damage to non-structural building elements, such as finishes, plaster, tiles, or non-load bearing walls. This threshold is typically defined as the level of motion that is sufficient to cause cracking, chipping, or detachment of these non-structural elements, but without compromising the overall safety of the building. Non-structural damage may also be referred to as cosmetic damage. Depending on the type of non-structural element considered, ground motion thresholds causing these damages will be different. The structural damage threshold to ground shaking is the minimum level of ground motion that can cause damage to the load-bearing elements of a structure, such as beams, columns, walls, and foundations and compromises integrity and safety of the structure.

The perception and damage thresholds definitions match closely with the descriptions of earthquake effects of different levels of MMI intensity. The Table 2-2 shows the correspondence of different thresholds with intensity level. This table is developed by comparing the above mentioned definitions of thresholds with Table 2-1. Since the different intensity level descriptions of MMI match reasonably well with the definitions of the perception/damage level descriptions, peak ground motion (or range of motions) can be associated to each intensity level.

Table 2-2. Table of intensity associated with threshold levels

Intensity	Threshold
II	Perception threshold
III	Quite noticeable
V	Widely felt event
VI	Non-structural damage threshold
VII	Structural damage threshold

2.4 Ground Motion to Intensity Conversion Equations

Ground Motion to Intensity Conversion Equations (GMICE) are mathematical relations that assign intensity number (MMI) to a given value of ground motion parameter (eg., PGA, PGV, PSA(T=1s), etc.). In some countries and regions with abundant seismic records(e.g., the United States, Japan, Italy, Turkey, New Zealand, and Taiwan) , researchers have explored the correlation between seismic intensity (through felt reports) and ground motion parameters and established the corresponding GMICEs (Tian et al., 2021). There has been a large number of researches in literature that provide GMICEs for different countries and regions (e.g., Wald et al., 1999; Kaka and Atkinson, 2004; Atkinson and Kaka, 2007; Worden et al., 2012; Sokolov 2002; Bilal and Askan, 2014; Wu et al., 2003; Caprio et al., 2015; Mortalla et al., 2021; Ahmadzadeh et al., 2020 and Tian et al., 2021).

In this study three GMICEs, Atkinson and Kaka (2007), Worden et al., (2012) and Caprio et al., (2015) are selected for investigation based on their relevance to the study region and its geology. Atkinson and Kaka (2007) GMICE (hereafter referred as AK07) is developed based on empirical relationships between instrumental ground motion parameters and observed MMI by using data from felt moderate earthquakes in the central United States and California that were also recorded on broadband seismographic networks and strong motion recorders in the region. AK07 found that the smallest error standard deviation corresponds to the equation that used PGV as the predictive variable. The functional form (Equation 2-1) of the AK07 GMICE is:

$$\text{MMI} = 4.37 + 1.32 \times \text{Log}_{10}(\text{PGV}) \quad \text{if} \quad \text{log}_{10}(\text{PGV}) \leq 0.48 \quad (2-1)$$

$$\text{MMI} = 3.54 + 3.03 \times \text{Log}_{10}(\text{PGV}) \quad \text{if} \quad \text{log}_{10}(\text{PGV}) \geq 0.48$$

where MMI is the intensity and PGV is the peak ground velocity in units of cm/s.

Worden et al., (2012) GMICE (hereafter referred as Wea12) is developed based on the database of 200000 MMI reports in California (on “Did you feel it” system) and a comparable number of peak ground-motion amplitudes from California seismic networks. This model assigns MMI values to the measurements of PGA, PGV, and PSAs for T=0.3 s, 1.0 s, and 3.0s and the model fitting is carried out using total least squares (TLS) method with intention to make the relation reversible (i.e., assigning ground motion to a given value of MMI). Worden et al., (2012) also finds that MMI predictions based on PGV as the predictor variable result in the smallest residual standard deviation. The functional form of Wea12 GMICE (GMICE2) for PGV as independent variable is:

$$\text{MMI} = 3.78 + 1.47 \times \text{Log}_{10}(\text{PGV}) \quad \text{if} \quad \text{log}_{10}(\text{PGV}) \leq 0.53 \quad (2-2)$$

$$\text{MMI} = 2.89 + 3.16 \times \text{Log}_{10}(\text{PGV}) \quad \text{if} \quad \text{log}_{10}(\text{PGV}) \geq 0.53$$

where MMI is the intensity and PGV is the peak ground velocity in units of cm/s.

Caprio et al., (2015) analyzed the regional dependance of several GMICES and derived a new global relationship. For this purpose Caprio et al., (2015) merged the databases used for developing six GMICES, including AK07 and Wea12, and, similar to Wea12, fitted the model using orthogonal least squares technique and developed a new GMICE (hereafter referred as Cea15). Although the Cea15 model is developed only for PGA and PGV as predictor variables. This GMICE has a couple of favorable characteristics: 1-similar to Wea12, is reversible, and therefore the ground motions associated with an MMI value can be estimated the the equation provides associated variability (σ); and 2-because it is based on larger database, based on global data, it is applicable to different regions within reasonable variability. The functional form of Caprio et al., (2015) is shown in Equation 2-3 for PGV and 2.4 for PGA as predictor variables are:

$$\text{MMI} = 4.424 + 1.589 \times \text{Log}_{10}(\text{PGV}) \quad \text{if} \quad \text{log}_{10}(\text{PGV}) \leq 0.3 \quad (2-3)$$

$$\begin{aligned}
 \text{MMI} &= 4.018 + 2.671 \times \text{Log}_{10}(\text{PGV}) & \text{if} & \quad \text{log}_{10}(\text{PGV}) \geq 0.3 \\
 \text{MMI} &= 2.270 + 1.647 \times \text{Log}_{10}(\text{PGA}) & \text{if} & \quad \text{log}_{10}(\text{PGA}) \leq 1.6 \\
 \text{MMI} &= -1.361 + 3.822 \times \text{Log}_{10}(\text{PGA}) & \text{if} & \quad \text{log}_{10}(\text{PGA}) \geq 1.6
 \end{aligned}
 \tag{2-4}$$

Similar to AK07 and Wea12, MMI is the intensity, PGV is the peak ground velocity in units of cm/s and PGA is the peak ground acceleration in cm/s^2 .

Figure 2-3 shows the comparisons of the intensity predictions, MMI, as a function of ground motion. The AK07 and Cea15 GMICES are very close to each other in estimating MMI associated to a peak ground motion (both PGA and PGV), especially at stronger motions. The Wea12 GMICE is relatively far from the other two in almost all motions. Considering that it is intended to use selected GMICE in reverse form (calculated peak motion associated with an MMI intensity), it is clear that for every intensity Wea12 model will predict stronger motions and will be less conservative. At intensities less than 4, AK07 seems to be slightly more conservative, but at intensities V and VI the Cea15 is slightly more conservative.

Figure 2-4 Compares PGV of MMI=II, III, IV based on three selected GMICES with perception and non-structural damage threshold spectra of US Army Engineering Manual EM 1110-2-3800 (USACE, 1972) and USBM RI 8507 (Siskind et al., 1980). These comparisons show that:

- Ground motions associated to intensities based on different GMICES show some variability. This was also observed in Figure 2-3 and found that Wea12 GMICE predicts higher PGV for a any intensity, than other two models in all intensities
- Overlay of GMICES on USBM RI 8507 (non-structural damage threshold) and USACE 1972 (human perception limits to blast vibration) shows consistency between intensities and felt/damage thresholds
- At MMI III (~0.13 mm/s) reported by Cea15 the human perception level threshold may be surpassed
- An intensity IV as reported by Cea15 (~0.5 cm/s), motions may begin to enter the unpleasant range
- Peak particle velocity is typically a relatively low frequency measure. The frequency content of the source will play a role in perception / damage levels

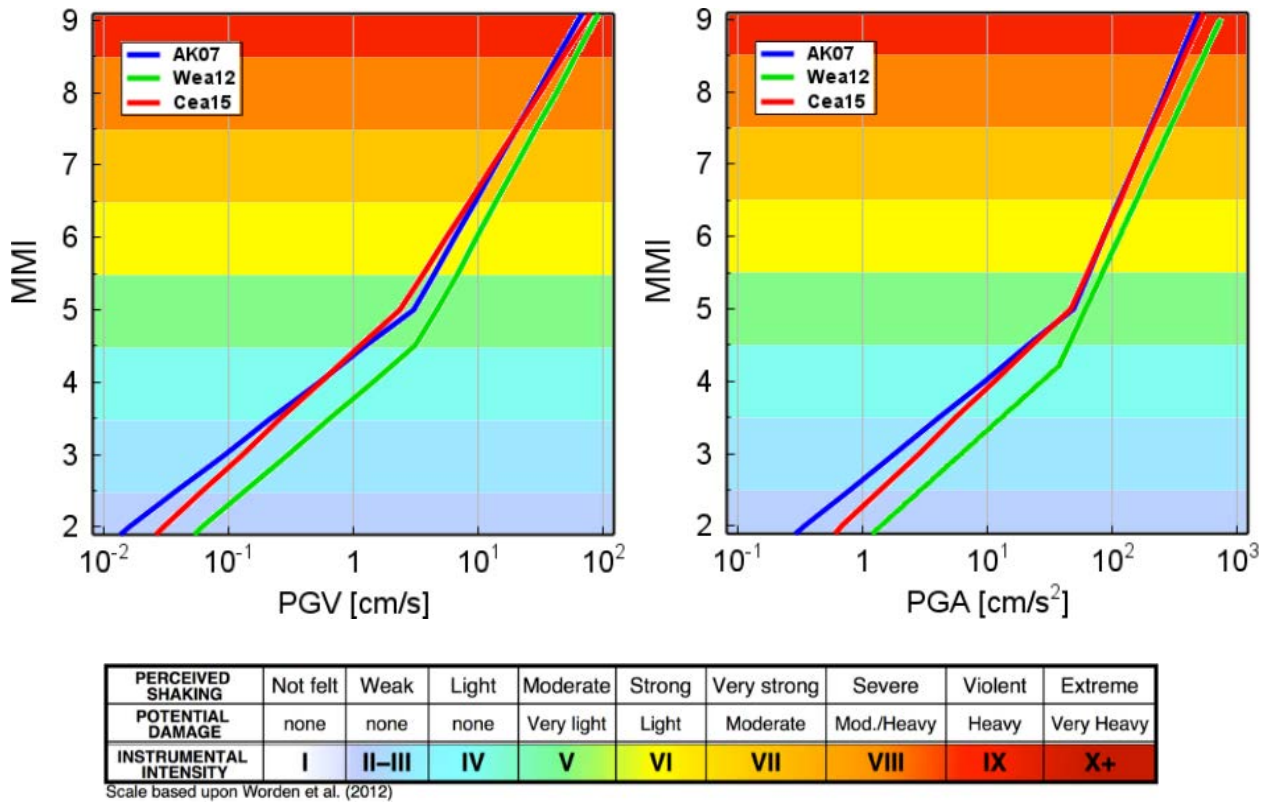


Figure 2-3. Comparison of AK07, Wea12 and Cea15 GMICEs estimates of MMI as a function of PGV (left) and PGA (right).

After reviewing the articles of three GMICEs that are the most relevant to the study area, comparing their curves with one another as well as standard perception/damage threshold spectra, it was found that Cea15 GMICE is the most appropriate for use in this study. The choice is based on the large global database of MMI/ground motions used to develop the model (rather than rely solely on motions from California), it is reversible, provides variability measure, and it is comparable or generally more conservative compared to AK07 and Wea12. .

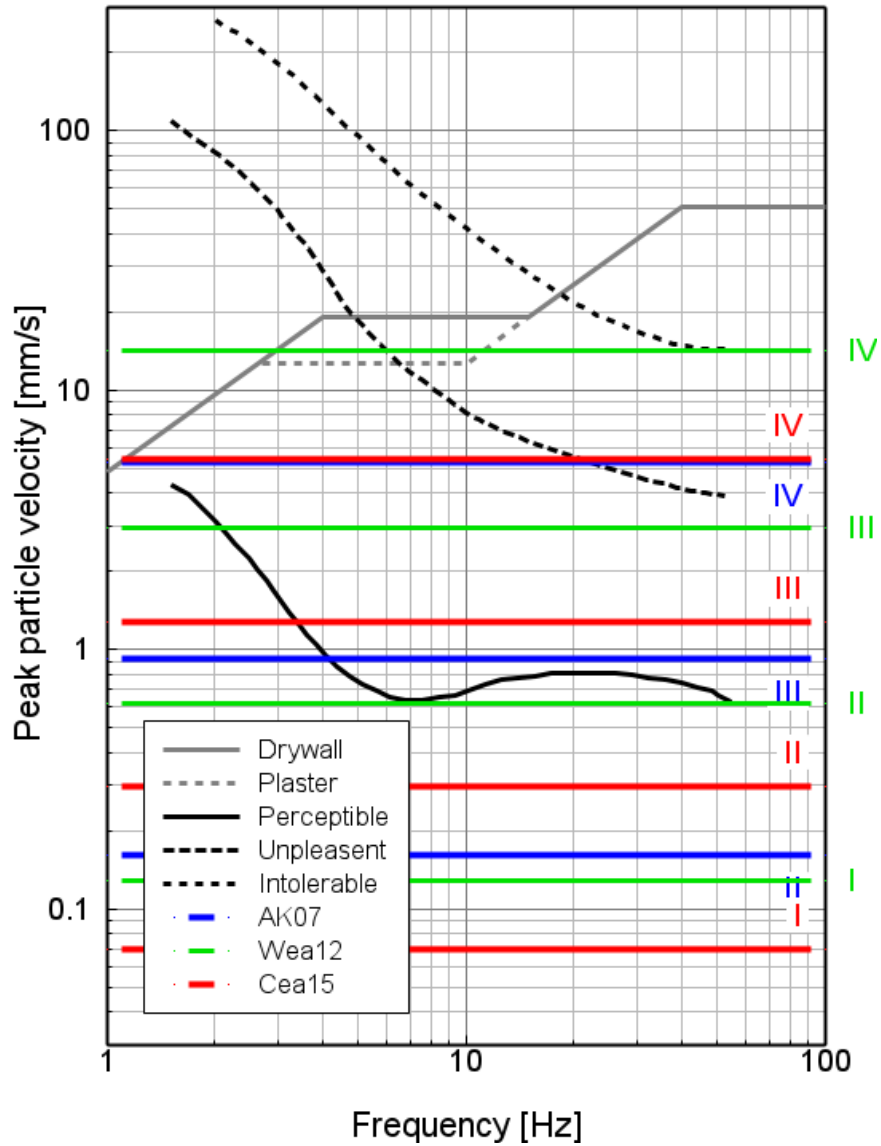


Figure 2-4. Comparison of PGVs associated with MMI=I,II,III,IV based on GMICES with perception and non-structural damage spectra of USACE (1972) and Siskind et al., (1980). The red, green and blue lines represent the center of the band associated with an intensity and they are in a reasonable agreement with one another (especially AK07 and Cea15).

2.5 Analyzing Ground Motion In Fort St. John

With more than 21000 residents (based on the 2021 census), Fort St. John is the most populated city in the study area and this gives a reasonable probability of having reports of felt ground motions due to earthquakes when they occur in the area, as well the city is expected to exhibit elevated levels of background noise associated with cultural activities. The Canadian Nation Network seismic station, NBC7, is located to the north of the city.

Continuous time-history records during the period of November 16, 2018 to December 15, 2018 are collected from a seismic station located in Fort St. John. Statistics of peak and mean level ground motions resulting from induced seismic events and background noise at different times of day are analyzed. During this period, three earthquakes of M3+ occurred after 5:00 PM local time on November 29, 2018 about 20 km south of Fort St. John with the following parameters (note that the date/times in the following are Universal Time):

- M_w 3.90, 2018-11-30 01:27:06 at R_{epi} =26.5 km
- M_w 3.22, 2018-11-30 02:06:01 at R_{epi} =26.7 km
- M_w 3.68, 2018-11-30 02:15:00 at R_{epi} =26.8 km

Figure 2-5 shows a map of the city of Fort St. John, with the location of NBC7 seismographic station and the locations of these seismic events. The left panel is the aerial map of the city which shows the limits of the city and the location of NBC7 seismic station. The right panel shows the location of the city in the study region as well as the locations of three seismic events from Nov. 30, 2018 at the south-southeast of Fort St. John. In the right panel, the red dash line is the limit of the study area and the black square approximately shows the range of the left panel on the map.

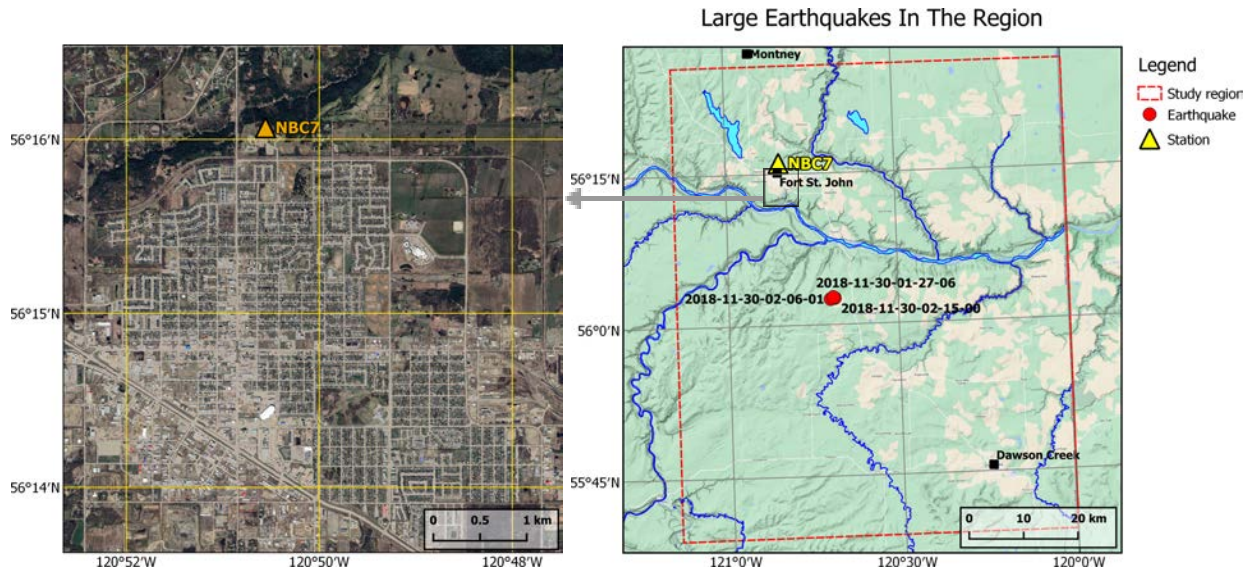


Figure 2-5. (Left) The aerial map of Fort St. John with the yellow rectangle showing the location of NBC7 station, (right) map of the study area (red dashed frame), locations of Nov. 30, 2018 M3⁺ earthquakes (red circles), limits of Fort St. John city (narrow black rectangle) and NBC7 Seismic station.

Three component raw digital time histories of NBC7 station from beginning of Nov.16, 2018 to the end of Dec 16, 2018 (a full month) are collected and processed. The following are the processing stages of the raw records:

- Removal of offsets, trends and outliers
- Band-pass filtering with corner frequencies at 0.1 Hz and 80 Hz frequencies
- Correction for Instrument response

The result of above mentioned processing stages is a month-long digital time history with correct physical units for each channel (component). Then for each component a new time history is created based on the maximum absolute amplitude on the maximum horizontal component per minute measurements. This is the time history which is used for analyzing peak values during the month of collected data. Figure 2-6 shows the plot of processed time history (maximum of two horizontal peak absolute amplitudes) for both PGA and PGV motions on one minute intervals (red line). A 30-minute running average is also computed and shown in the figure (black line), with an overall range of maximum horizontal amplitudes over the month-long window (yellow shading).

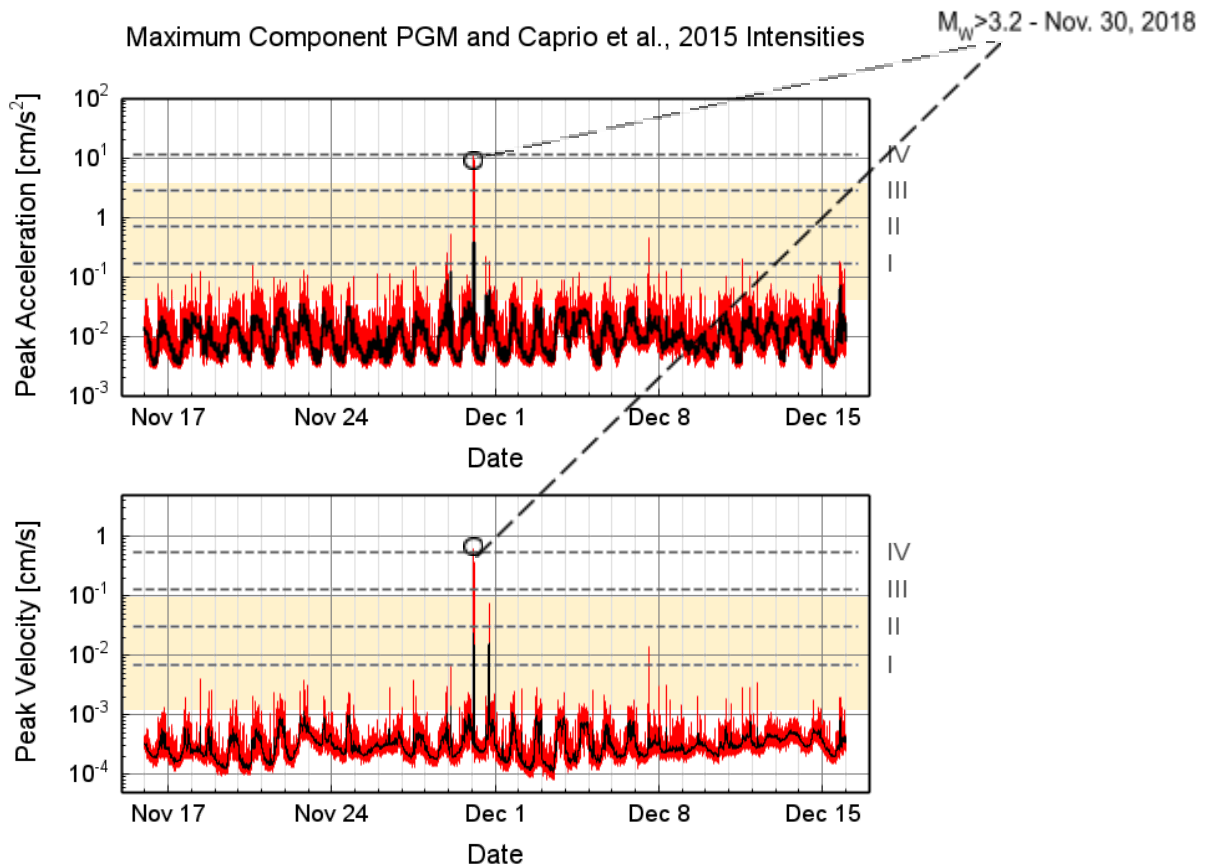


Figure 2-6. Greater of two horizontal components' maximum amplitude of one minute intervals for a month recorded data at NBC7 is shown in red curves for both PGA and PGV motions in upper and lower panels respectively. The black curves are the 30 minute moving average of red curves. The dash lines specify ground motion levels associated with the shown Intensities based on Caprio et al., (2015) equation, with the corresponding MMI to the right..

In Figure 2-6, the spike during Nov. 30 corresponds to the three M3.9, M3.22 and M3.68 events located ~ 25 km southeast of Fort St. John with peak ground motion records from these events in the level of MMI=4, therefore it is expected the motion had been perceived by Fort St. John residents. The figure also shows that the daily peak acceleration due to cultural noise is $\text{PGA} \leq 0.2 \text{cm/s}^2$ with an average of $\text{PGA} \leq 0.04 \text{cm/s}^2$ and peak velocity is $\text{PGV} \leq 0.006 \text{ cm/s}$ with an average of $\text{PGV} \leq 0.0015 \text{ cm/s}$. Additionally, daily background

peak ground motions are within range of $MMI=1$ and the level of cultural noise does not reach the perception threshold. As well the plot of moving averages of peak motions show daily fluctuation of average background noise level.

Figure 2-7 and 2-8 show the distribution of peak horizontal amplitudes of 1-minute windows in one hour bins (in local time) for PGV and PGA respectively. Each black circle represents a reading of peak absolute amplitude of the one minute windows and all minutes within the same hour (e.g, 5am to 6am) across all days of the month. Then within each bin the geomean as well as the standard deviations of log amplitudes are calculated. Using calculated geomean and standard deviations the center value as well as its 1 and 2 standard deviation neighborhood bands are specified in Figures 2-7 and 2-8 (orange squares, triangles and crosses specify geomean, and its $\pm 1\sigma$ and $\pm 2\sigma$ bands respectively). The horizontal dotted lines show the intensity levels based on Caprio et al.,(2015) GMICEs. The horizontal red dash line in Figure 2-8 specifies the 0.8%g PGA level which is the current threshold recommended by BCER and its level is between perception threshold and “felt by some” range.

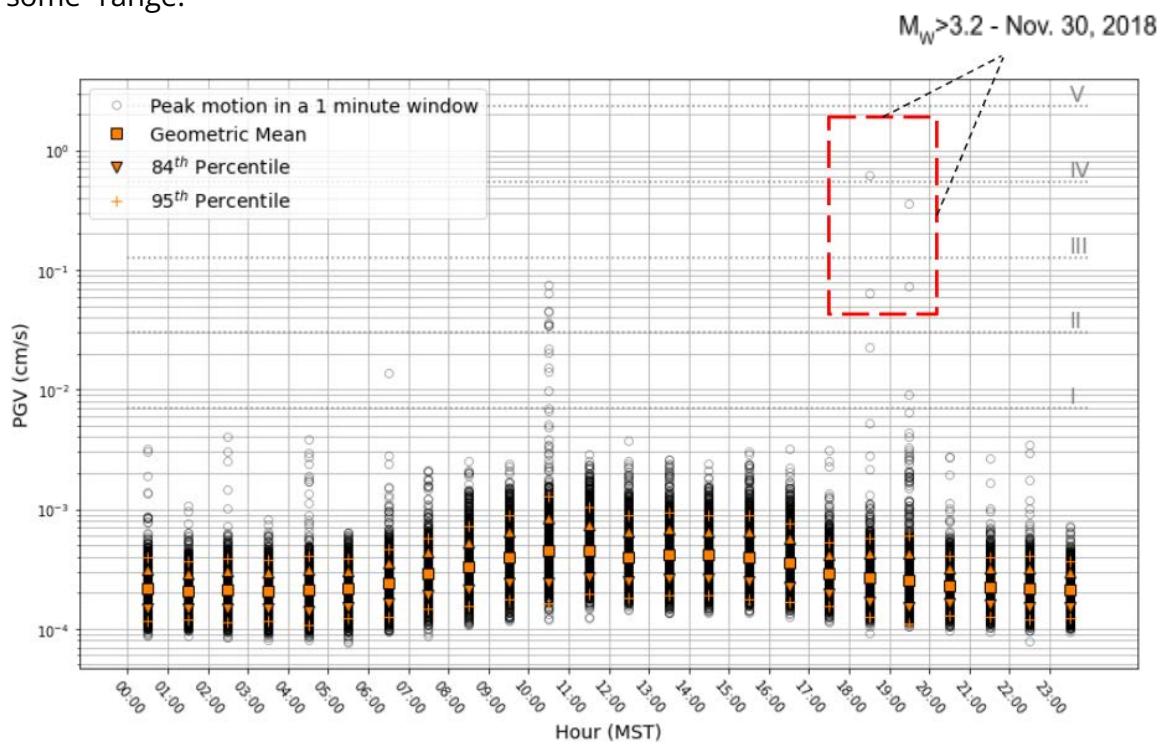


Figure 2-7. Distribution of peak horizontal amplitudes of 1-minute windows in one hour bins (in local time) for PGV.

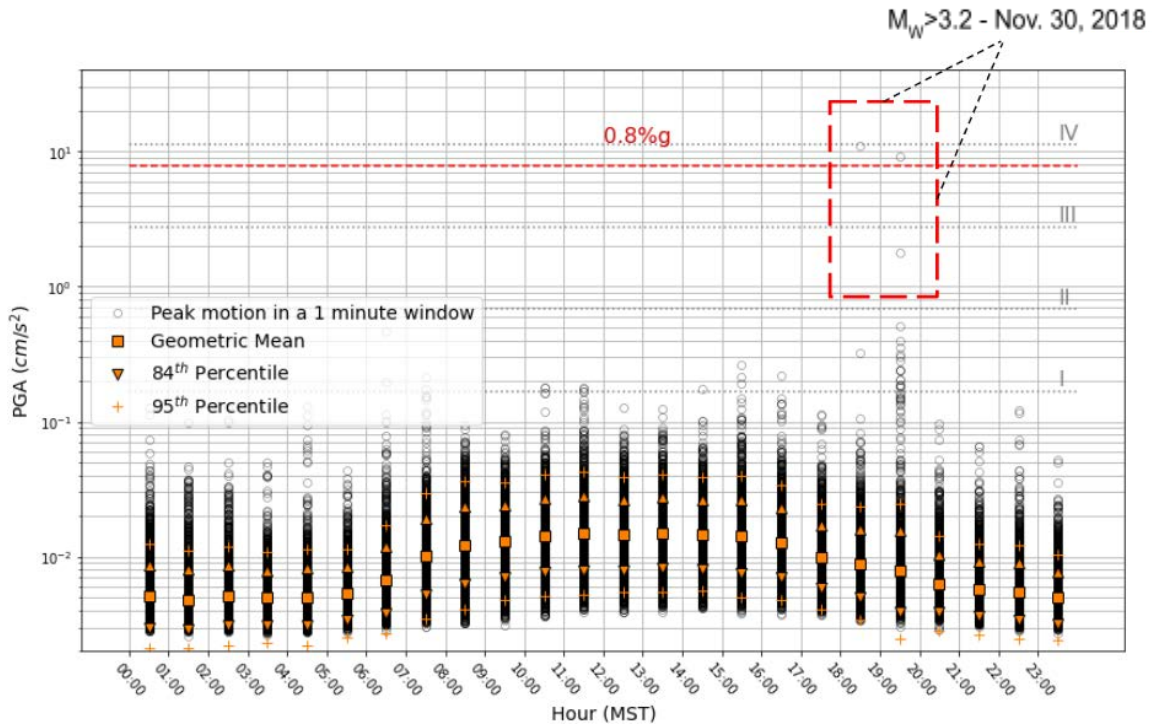


Figure 2-8. Distribution of peak horizontal amplitudes of 1-minute windows in one hour bins (in local time) for PGA.

Figures 2-7 and 2-8 show that there is daily fluctuation of the average of peak horizontal motions and its pattern follows daily work hours and therefore most of the recorded motions are due to cultural noise. The ability to distinguish vibrations resulting from an earthquake versus other anthropogenic activities would be slightly higher during the evenings when populations are typically at home and at rest rather than during the day where populations are more likely to be active. In addition these figures show that the amplitudes associated with the cultural noise correspond to intensities less than MMI=I and occasionally within MMI=I and MMI=II. Also, the peak ground motion amplitudes associated with the three $M_w > 3.2$ earthquakes south of Fort St. John (enclosed in red dashed rectangular box) reaches intensities close to MMI=IV on both PGA and PGV graphs and this suggests the earthquake motions would be felt by some in the city.

2.6 Associating Felt Reports With Ground Motion

During the time period of analyzed seismographic data in this study, there are four $M_w > 2.8$ events in the region whose motions are associated with felt reports. Table 2-3 lists the earthquakes that are associated with felt reports and shows the number of reports per each earthquake. However, there is only one location with felt reports for two events which is co-located with real recording (event # 1 and # 3 at MONT1 station) and although records of these events from NBC7 and ST33 stations at populated areas are analyzed, there is no felt report associated with them. Therefore to be able to compare the felt reports with ground motion intensities, the assimilated ground motion amplitudes from the shakemaps generated in the previous section are assigned to felt report locations in later analysis. Figure 2-9 shows the shakemap of PGV of the first record in Table 2-3 overlain with white squares showing the felt report locations.

Table 2-3. List of earthquakes associated with felt reports (note that larger events have larger number of reports)

Number	Date/Time (UTC)	Latitude	Longitude	Magnitude [M_w]	# of reports
1	2018-11-30 01:27:06	56.0403	-120.6911	3.90	14
2	2018-11-30 02:06:01	56.0441	-120.6944	3.22	1
3	2018-11-30 02:15:00	56.0424	-120.8625	3.68	3
4	2020-09-11 22:37:27	55.8934	-120.3863	2.92	2

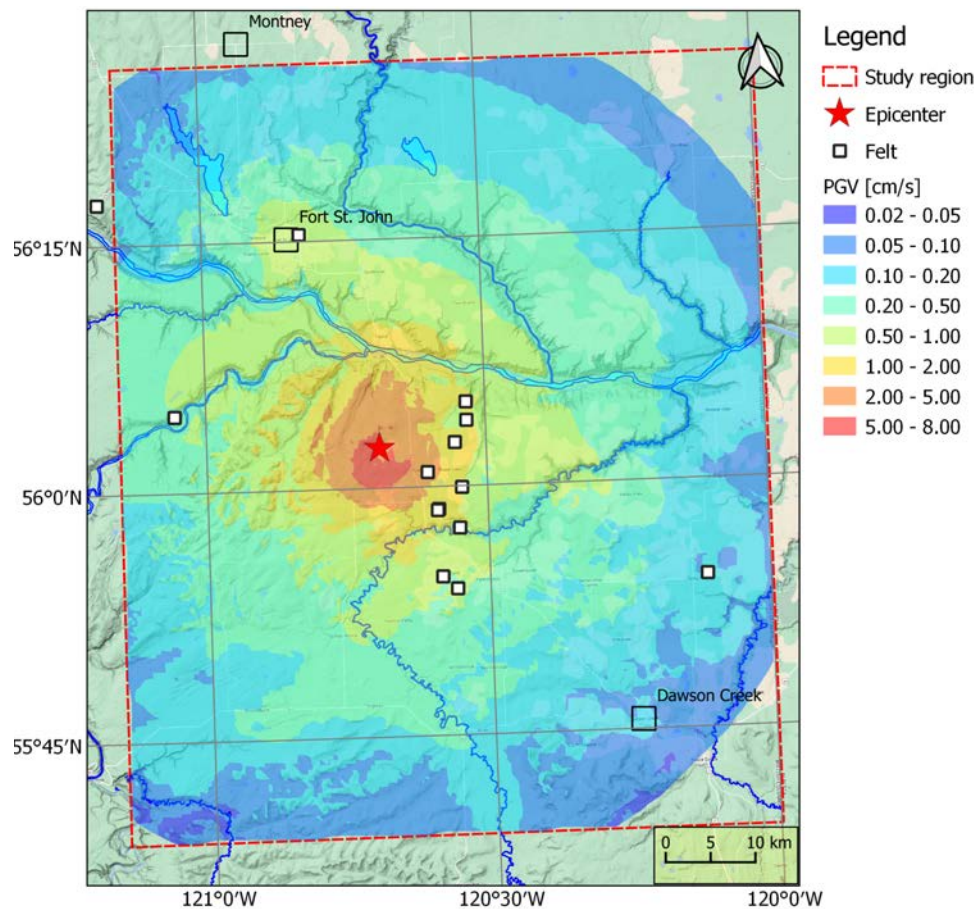


Figure 2-9. Shakemap of PGV of the first event in Table 3-3 (M_w 3.9 at 2018-11-30 01:27:06 UTC) overlaid with the locations of felt reports.

To validate the performance of translating the developed GMPE of this study and to MMI scale with the adopted GMICE (Caprio et al., 2015), the felt reports are compared with ground motions and intensity estimates at reporting locations. The following describes these comparisons and findings.

For initial estimation of the felt effects at reporting sites MMI shakemaps based on PGV map of Figure 2-9 and Caprio et al., (2015) GMICE is prepared and overlain by felt reporting locations (Figure 2-10). This provides a range of intensity estimates that is felt by residents and reported.

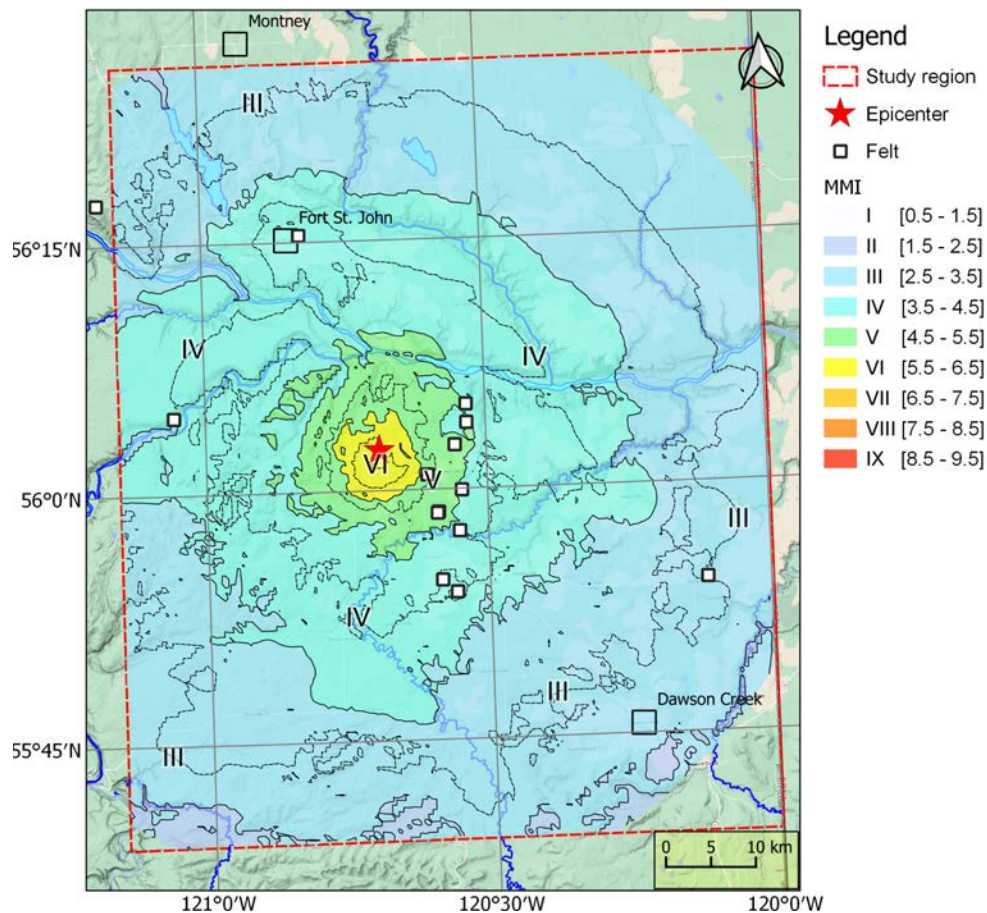


Figure 2-10. MMI intensity Shakemap of M3.9 (at 2018-11-30 01:27:06 UTC) event based on shakemap of PGV (Figure 2-9) and Caprio et al., (2015) GMICE. The white circles show the locations with felt reports.

The distribution of points with felt reports on MMI shakemap shows that:

- Most of the reports are located within areas with intensity IV and V and this is consistent with the review of the reports:
 - All reports suggest a major event with significant shaking
 - The felt effect of the nearest reporting site is “Report of a major earthquake near reporter’s home. Dishes shook off the table” and on the map it corresponds to shaking levels of intensity 5
- There are just two felt reports corresponding to intensity III
- Felt reports are above the perception threshold levels of intensity II-III and are consistent with literature

In the next set of comparisons, the ground motion values at the felt reports locations are extracted from the ground motion shakemaps (maps similar to Figure 2-9 developed for four events for both motion types PGA and PGV) and plotted as a function of hypocentral distance. Figure 2-11 shows the ground motion peak amplitudes (assimilated values estimated from shakemaps: PGA and PGV at left and right panels respectively) as a function of hypocentral distance. The colors of symbols specify the earthquakes (from Table 2-3) they correspond, the dashed lines are intensity estimates of Caprio et al., (2015) GMICE and the background shade shows the variation of intensities between dashed lines. On the right panel two symbols are outlined by gray circles and they correspond to the felt report explained next. In this figure the red circles correspond to the largest event (M_w 3.9) on Nov. 30, 2018 and the felt effects described for them are as follows:

- Report of a major earthquake near the reporter's home. Dishes shook off the table. This is the description for the symbol labeled as "1"
- Strong shaking
- Intense shaking
- Violent shaking
- Strong bang to the house
- Shaking of the whole house
- Pictures fell off the wall
- Vases fell off the table
- Dishes shook on the table
- Shaking was reported 4 miles away

The green and blue circles correspond to two $M_w > 3.2$ aftershocks with the following descriptions:

- Most of the reports are just 'felt effects' after the mainshock
- The whole house shook. This is the description of the symbol labeled as "2"

The open circles correspond to a M_w 2.9 event on Sept. 11, 2020 about 17 km NW of Dawson Creek and there is no description of the motion in the report.

Although there were reports of damage to dishes and other contents, there were no reports of damage to buildings in terms of non-structural or structural damage, which aligns with the maximum intensities experienced of MMI V.

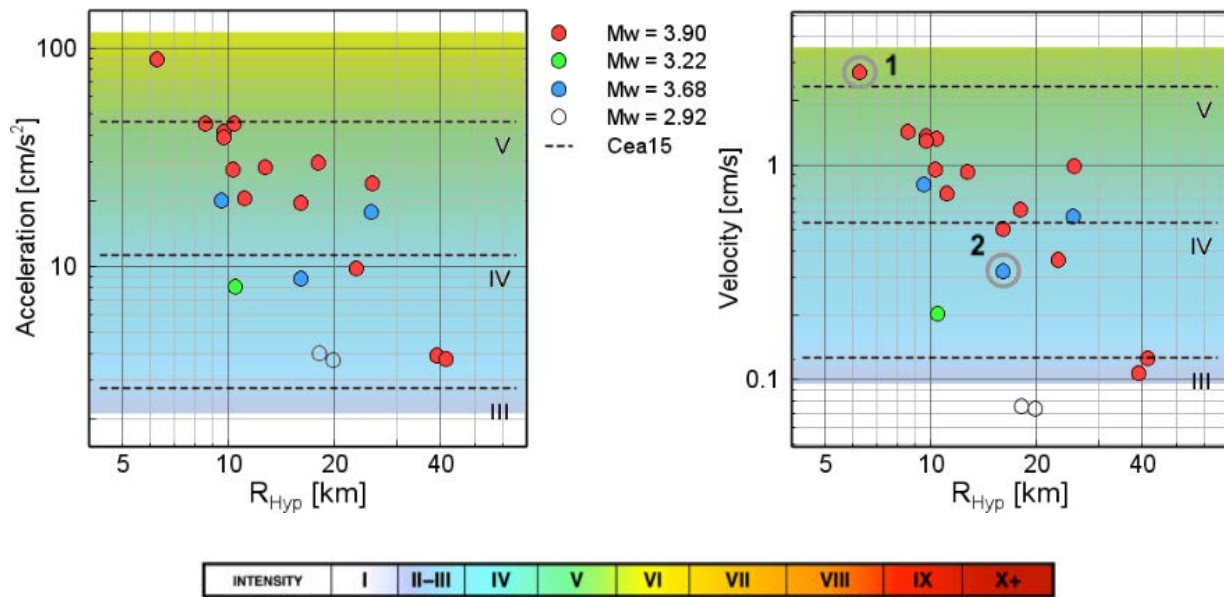


Figure 2-11. Ground motion assimilated peak amplitudes from shakemaps (PGA and PGV at left and right panels respectively) as a function of hypocentral distance. The symbol colors correspond to four events with felt reports (in Table 2-3), the dashed lines and background shades specify the MMI intensity based on Caprio et al., (2015) GMICE.

Figure 2-12 shows the overlay of few existing instrumental measurements on the plots shown in Figure 2-11. The square symbols show measured maximum horizontal amplitudes and their colors specify their range of magnitudes, and the colors are chosen to be consistent with those of the assimilated (shakemap) motions' symbols. Comparison of the distributions of assimilated amplitudes (circles) with those of instrumental measurements (square symbols) shows reasonable agreement. Two instrumental measurements, shown in black dots and enclosed in a gray dashed rectangle, fall within 120 m distance from felt report sites. The center of the circles represent the estimated amplitudes on shakemap based on the GMPE and site amplification grid developed in phase 1, and the black dots are real measurements. This analysis demonstrates that there is reasonable agreement between shakemap estimates and instrumental measurements in similar distances.

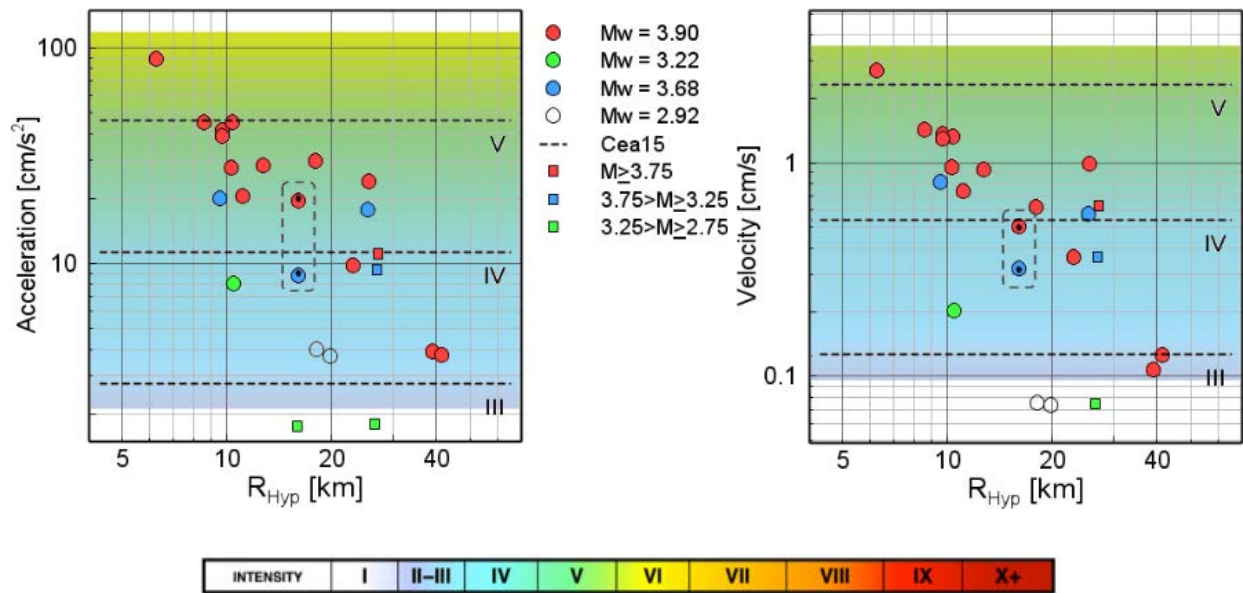


Figure 2-12. Circles and squares/black dots show the ground motion assimilated peak amplitudes from shakemaps (left: PGA, right: PGV) and measured peak amplitudes respectively as a function of hypocentral distance. The symbol colors correspond to the causative earthquake magnitude, the dashed lines and background shades specify the MMI intensity based on Caprio et al., (2015) GMICE. The gray rectangle shows amplitudes of co-located felt reporting site and seismic station.

2.7 Conclusion On GMICE Choice And Perception And Damage Thresholds

This study investigated the available literature and analyzed three GMICEs (equations relating MMI intensity, or implicitly perception/damage effects, to ground motion) relevant to the study area. Caprio et al., (2015) GMICE was found to be the most appropriate model and is adopted for use in this study. The basis for this choice are the following:

- It is more recent and is derived based on large database collected from wide geographic regions
- It assigns reasonable intensities to weaker ground motions and the felt effects are consistent with the results of other studies
- At stronger shaking motions, at intensities above IV (range of engineering concerns), it is more conservative than Worden et al. (2012) and consistent with Atkinson & Kaka (2007)

This study examined motions due to events of magnitudes $M_w > 2.8$ and found that the smallest perceived motions (perception threshold) are about $PGV \geq 0.07$ cm/s corresponding to intensity of MMI ~ II-III. This level of motion is:

- Consistent with USACE(1972) study perception thresholds due to blast
- Corresponds to acceleration of $PGA \geq 2.5\text{cm/s}^2$ (0.26%g, equivalent of a M1.5 at 1.7 km depth) and is consistent to the lowest perceptible amplitudes of Athanasopoulos & Pelekis (2000)
- Consistent with the lowest range of motions associated with felt reports

Motions associated with non-structural and structural damage motion thresholds are calculated using inverted equations of Caprio et al., (2015) corresponding to intensities of MMI ~ VI and VII (Onur et al, 2008 and Onur & Seemann 2004). The calculated motions for damage thresholds are:

- Non-structural:
 - $PGA = 84.3\text{cm/s}^2$ (8.6%g, equivalent of a M3.1 at 1.7 km depth) and 5.52cm/s
- Structural:
 - $PGA = 154.0\text{cm/s}^2$ (15.7%g, equivalent of a M3.5 at 1.7 km depth) and 13.87cm/s

This study finds regular background peak motion levels at Fort St. John correspond to intensities around or less than MMI ~ I and therefore are not perceptible/noticeable

3. Phase 3 - Review of Traffic Light Protocol Magnitude Thresholds

3.1 Introduction

In Phase 1, a ground motion prediction Equation (1-10) that describes the median ground motion level expected for an earthquake of magnitude M at distance R away as well as a site amplification map that accounts for localized site effects was developed. The variability of observed ground motions about the model were captured (section 1.4.6), and is used to evaluate the GMPE for different percentiles of motion (ie. 10% probability of exceeding threshold levels).

During Phase 2, perception and non-structural damage thresholds were determined through a literature review. They are found to be:

- Perception - $PGV=0.07\text{cm/s}$ (MMI II-III) which corresponds to acceleration of $PGA = 2.5\text{cm/s}^2$ (0.26%g)
- Non-structural - $PGV=5.52\text{cm/s}$ (MMI VI) which corresponds to acceleration of $PGA = 84.3\text{cm/s}^2$ (8.6%g)

Phase 3 aims to guide refinement of Traffic Light Protocol (TLP) magnitude thresholds on the basis of ground motions. To this end, maps displaying the maximum magnitude that is unlikely (assumed to be 10% probability) to exceed perception and non-structural damage thresholds are generated. With the goal in mind that damage of any severity should be avoided, we will refer to the possible onset of non-structural damage as 'damage' throughout the following sections. For discussion purposes, two cases are considered: Case 1 investigates the maximum magnitude unlikely to exceed the threshold for any point across the region, where maps for 50% and 10% probability of exceeding the existing BCER threshold of 0.8%g are also developed; and Case 2, where maximum magnitude unlikely to exceed the threshold for densely populated localities.

3.2 Generating Maximum Magnitude Maps

Maximum magnitude maps are generated by considering 10% probability of exceedance as 'unlikely' to occur. This means that 90% of ground motions originating from an earthquake of magnitude M at distance R away, will not exceed the defined threshold level. To generate maximum magnitude (M_{max}) maps the following points and steps are considered:

- Earthquakes are simulated for a range of magnitudes at 500 m interval across the entire region and considering localized site effects (site amplification grid)
- The minimum and maximum depths considered for this study are 1000 m and 2100 m respectively as they cover the typical upper and lower depth limits of earthquakes recorded in the region. The ground motion levels for each event is checked against the threshold for 2 cases:

1 - An exceedance at any location across the entire region

(a) Figures 3-1 and 3-2 display M_{\max} maps derived from PGA and PGV thresholds (identified in Phase 2) respectively, where the left panel in each figure shows the perception and the right panel shows the damage thresholds for events occurring at the depth of 1 km. Figures 3-3 and 3-4 show similar M_{\max} maps for events occurring at the depth of 2.1 km.

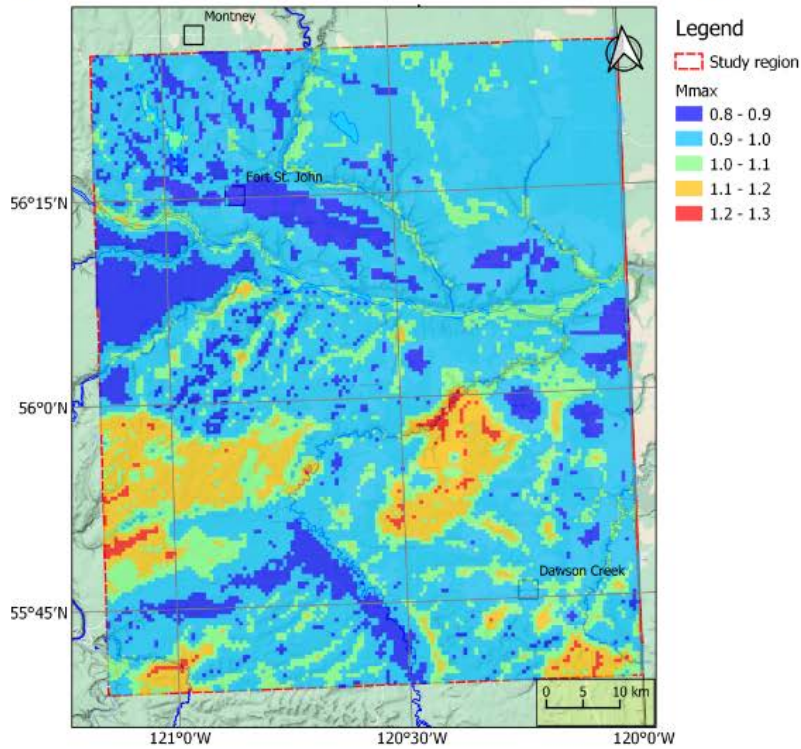
(b) M_{\max} maps are also generated based on 10% probability of exceeding the current BCER threshold of 0.8%g PGAs for both 1 km and 2.1 km depths. For comparison purposes additional maps are generated using the BCER threshold directly (50% probability of PGA exceeding 0.8%g). Figure 3-5 and 3-6 display M_{\max} maps for events occurring at depth of 1 km and 2.1 km respectively. The left panel of each figure shows M_{\max} maps considering the current BCER threshold of 0.8%g will have 50% chance of exceeding, and the right panel shows M_{\max} map with 10% probability of exceeding the current BCER threshold of 0.8%g.

2 - An exceedance at densely populated localities in the region

Maps are generated by considering maximum magnitudes that would not exceed the thresholds defined in Phase 2 within populated regions. The left and right panels show the M_{\max} with 10% probability to exceed the PGA and PGV perception thresholds respectively where Figures 3-7 and 3-8 show for the 1 km depth and 2.1 km depth cases respectively.

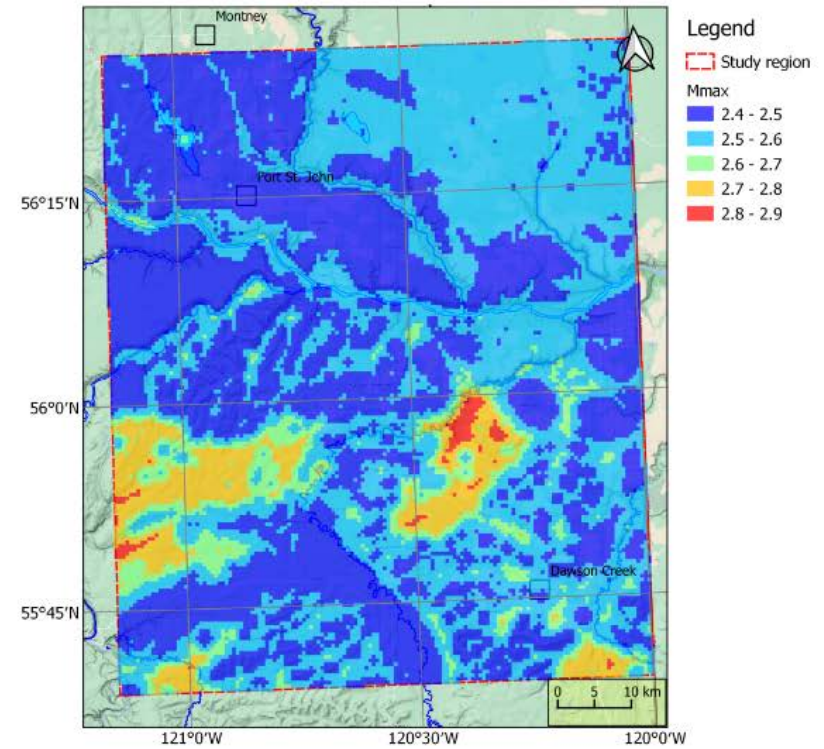
- The maximum ground motion value generated by a seismic event is expected to occur within 10km of the epicenter. The implication for Case #1 is that ground motions which approach the perception or damage threshold for any point on the surface will come from an event, in most cases, directly below the point. For Case #2, is that for increasing distance from populated regions, the magnitude scenario that would exceed the thresholds also increases.

10% Probability to Exceed **Perception** PGA 2.5 cm/s^2



Depth: 1 km

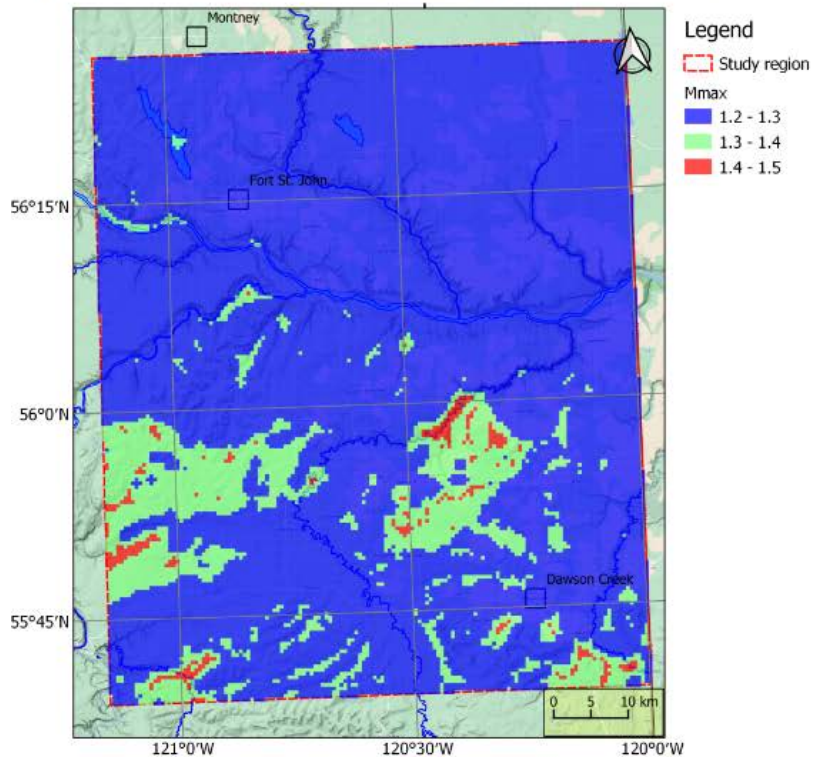
10% Probability to Exceed **Damage** PGA 84.3 cm/s^2



Depth: 1 km

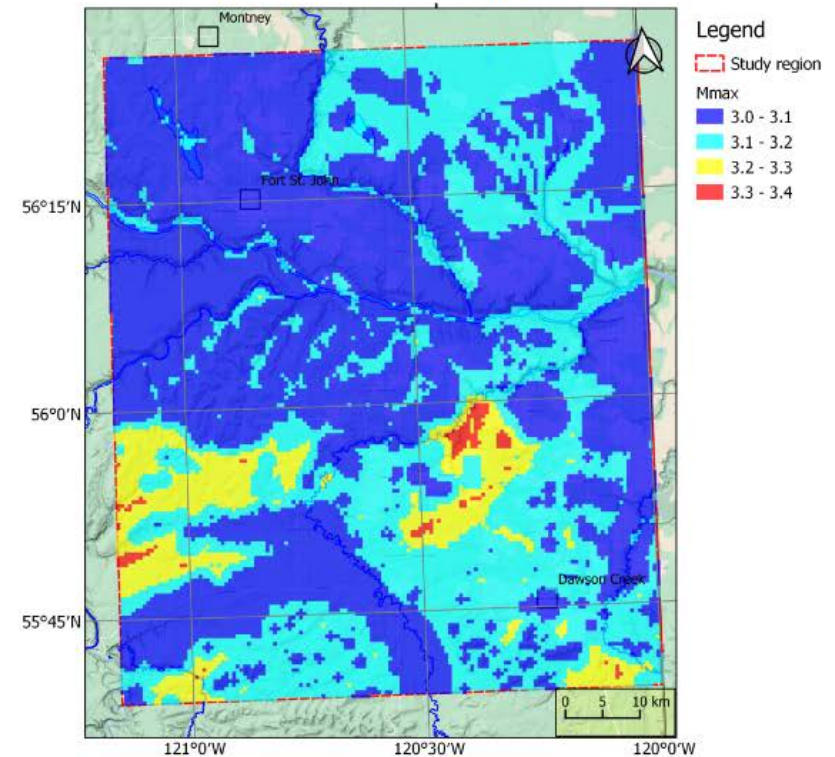
Figure 3-1: Maps of M_{\max} of earthquakes at depth of 1 km considering thresholds of PGA in the entire area. Left: 10% probability of exceeding perception threshold acceleration of 2.5 cm/s^2 and right: 10% probability of exceeding damage threshold acceleration of 84.3 cm/s^2 .

10% Probability to Exceed **Perception** PGV 0.07cm/s



Depth: 1 km

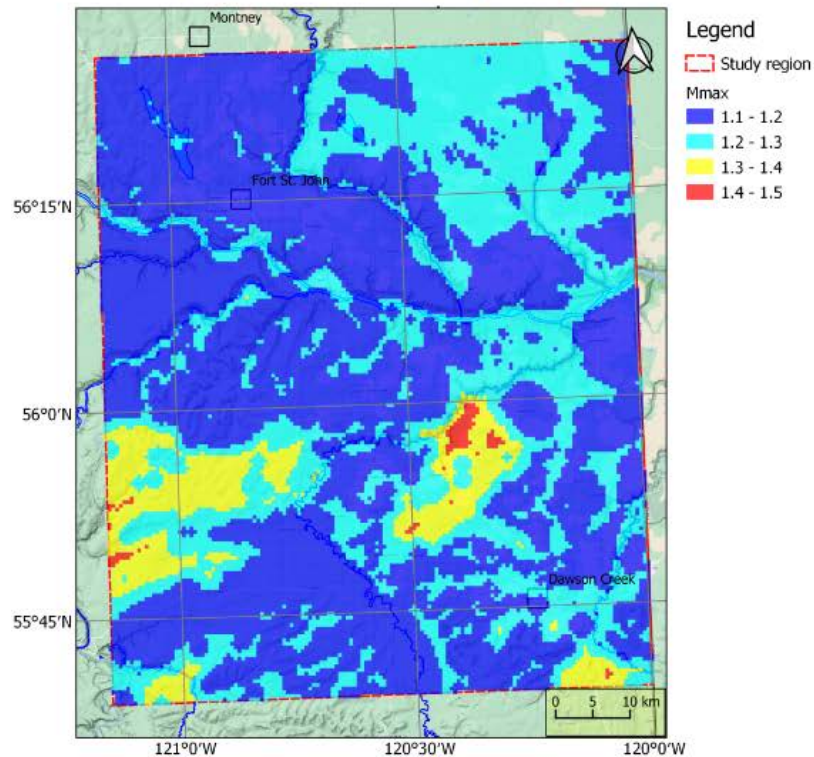
10% Probability to Exceed **Damage** PGV 5.52cm/s



Depth: 1 km

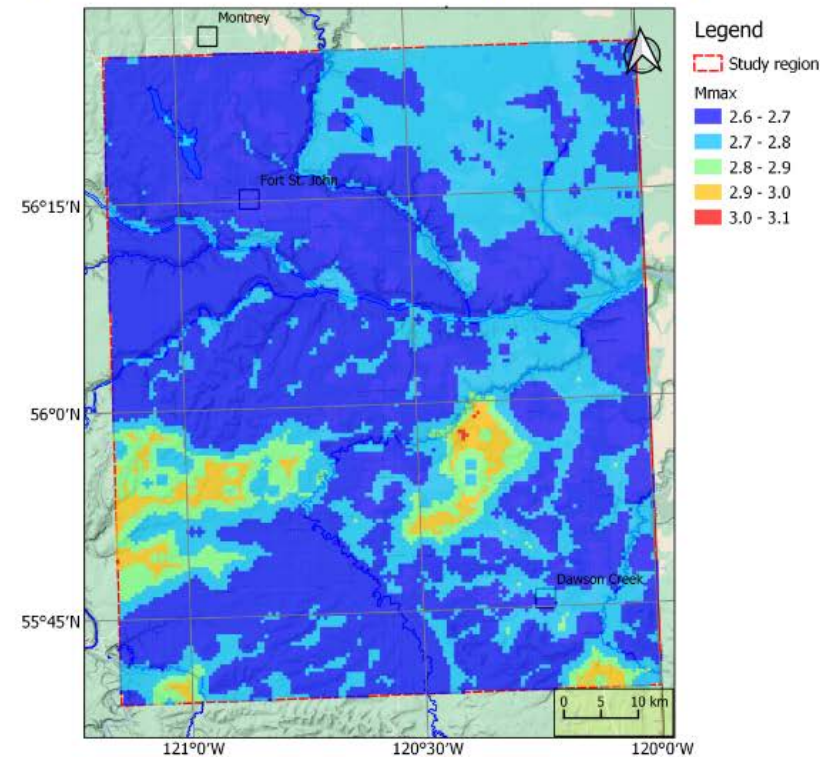
Figure 3-2: Maps of M_{max} of earthquakes at depth of 1 km considering thresholds of PGV in the entire area. Left: 10% probability of exceeding perception threshold velocity of 0.07 cm/s and right: 10% probability of exceeding damage threshold velocity of 5.52 cm/s.

10% Probability to Exceed **Perception** PGA 2.5 cm/s^2



Depth: 2.1 km

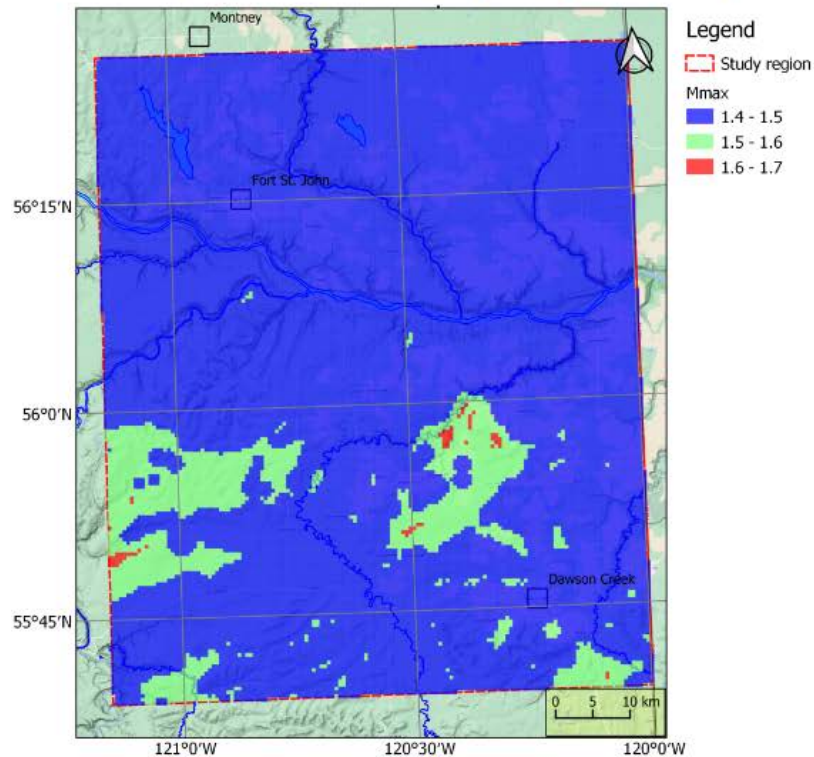
10% Probability to Exceed **Damage** PGA 84.3 cm/s^2



Depth: 2.1 km

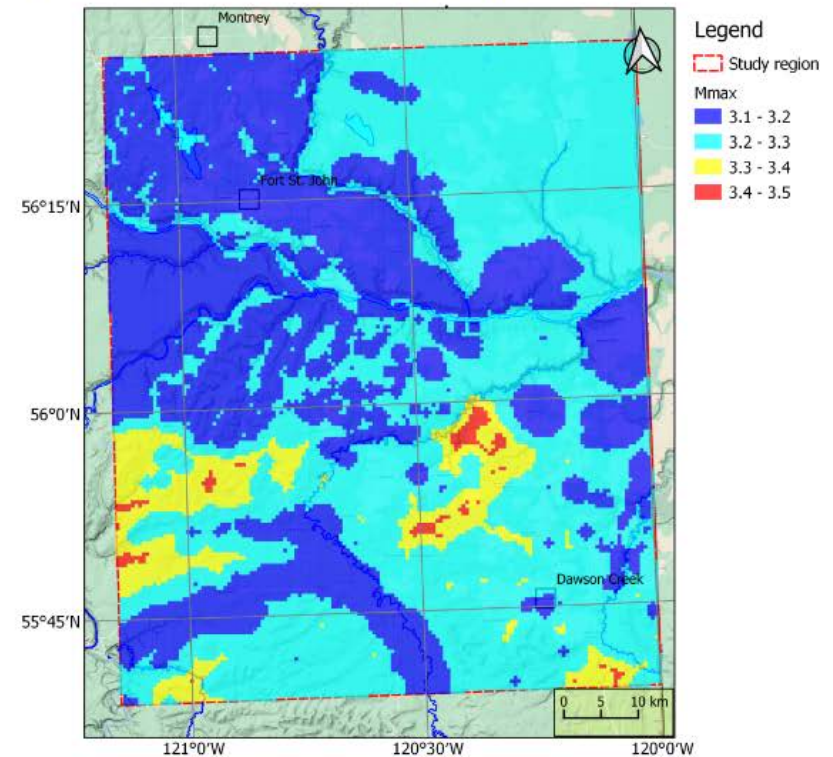
Figure 3-3: Maps of M_{\max} of earthquakes at depth of 2.1 km considering thresholds of PGA in the entire area. Left: 10% probability of exceeding perception threshold acceleration of 2.5 cm/s^2 and right: 10% probability of exceeding damage threshold acceleration of 84.3 cm/s^2 .

10% Probability to Exceed **Perception** PGV 0.07cm/s



Depth: 2.1 km

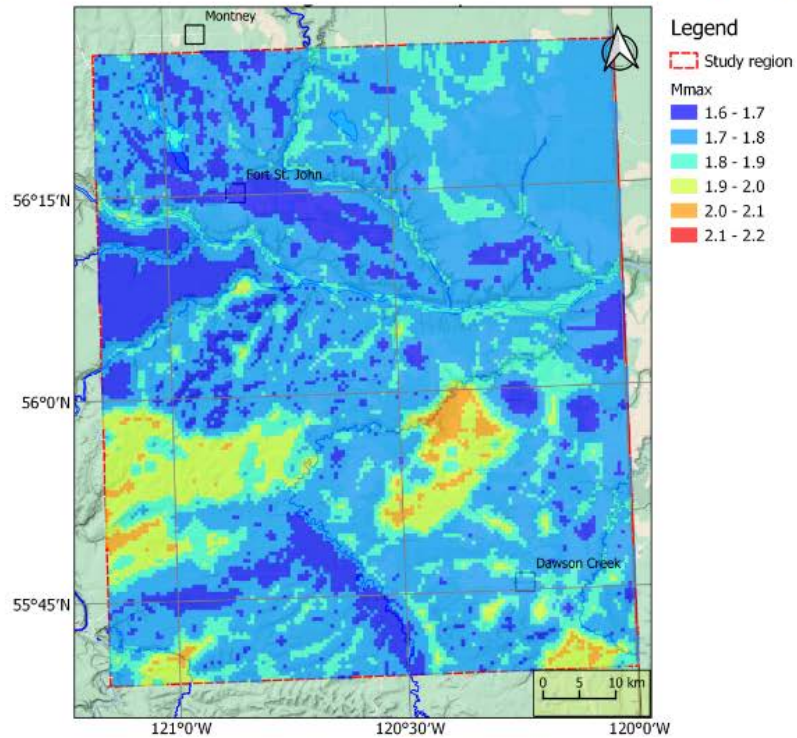
10% Probability to Exceed **Damage** PGV 5.52cm/s



Depth: 2.1 km

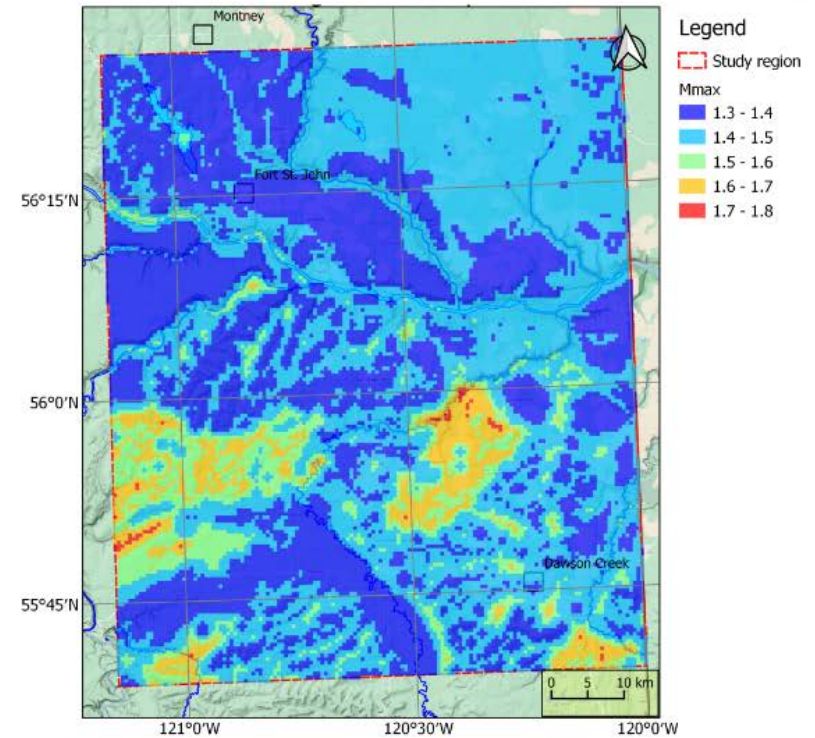
Figure 3-4: Maps of M_{max} of earthquakes at depth of 2.1 km considering thresholds of PGV in the entire area. Left: 10% probability of exceeding perception threshold velocity of 0.07 cm/s and right: 10% probability of exceeding damage threshold velocity of 5.52 cm/s.

50% Probability to Exceed **BCOGC** PGA 7.85 cm/s^2 (0.8%g)



Depth: 1 km

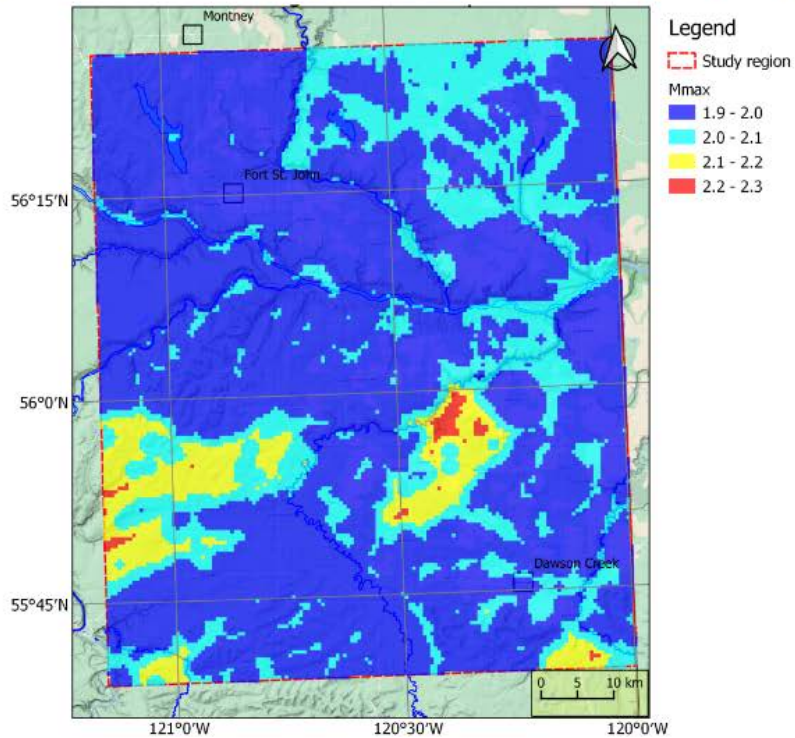
10% Probability to Exceed **BCOGC** PGA 7.85 cm/s^2 (0.8%g)



Depth: 1 km

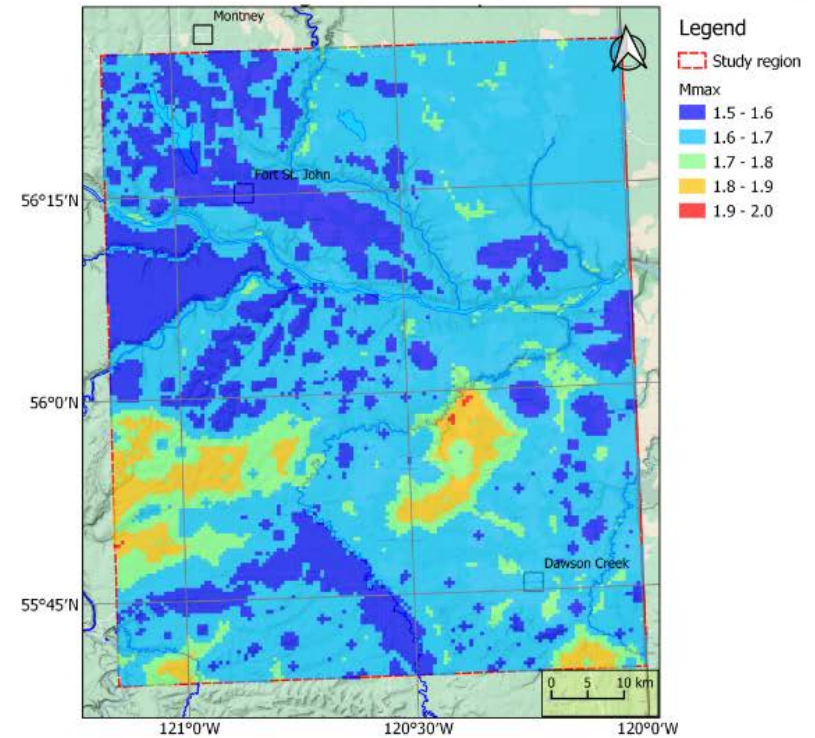
Figure 3-5: Maps of M_{\max} of earthquakes at depth of 1 km considering BCER thresholds of 0.8%g for PGA in the entire area. Left: 50% probability of exceeding BCER thresholds and right: 10% probability of exceeding BCER thresholds.

50% Probability to Exceed **BCOGC** PGA 7.85 cm/s^2 (0.8%g)



Depth: 2.1 km

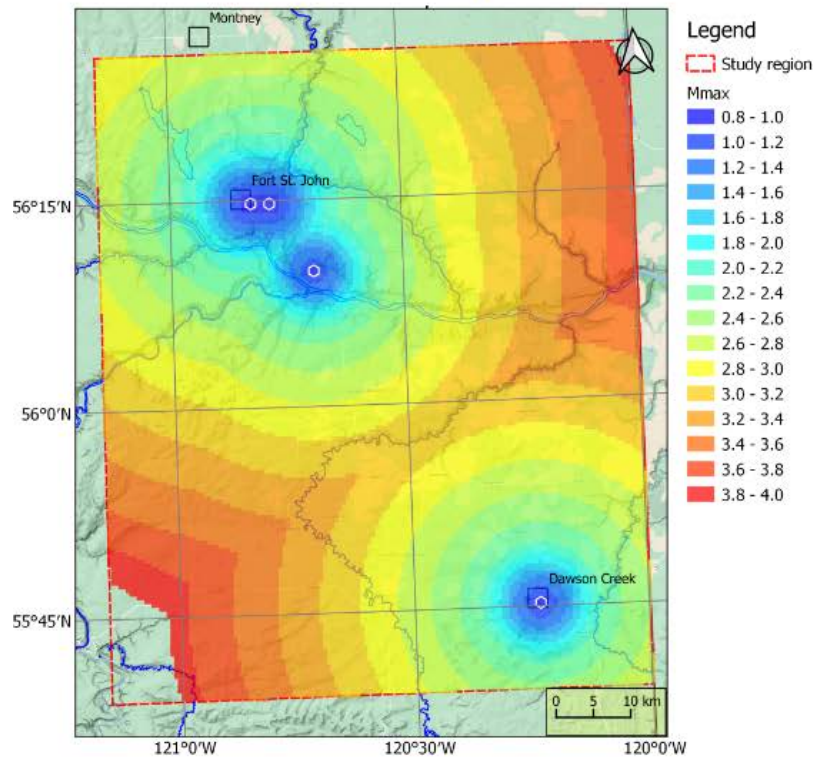
10% Probability to Exceed **BCOGC** PGA 7.85 cm/s^2 (0.8%g)



Depth: 2.1 km

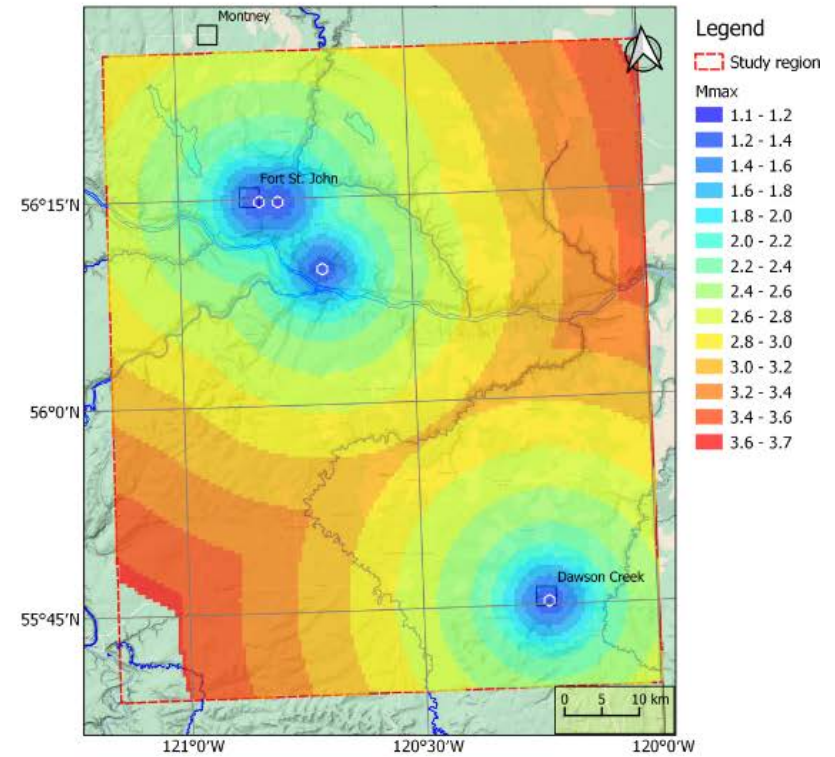
Figure 3-6: Maps of M_{\max} of earthquakes at depth of 2.1 km considering BCER thresholds of 0.8%g for PGA in the entire area. Left: 50% probability of exceeding BCER thresholds and right: 10% probability of exceeding BCER thresholds.

10% Probability to Exceed **Perception** PGA 2.5 cm/s²



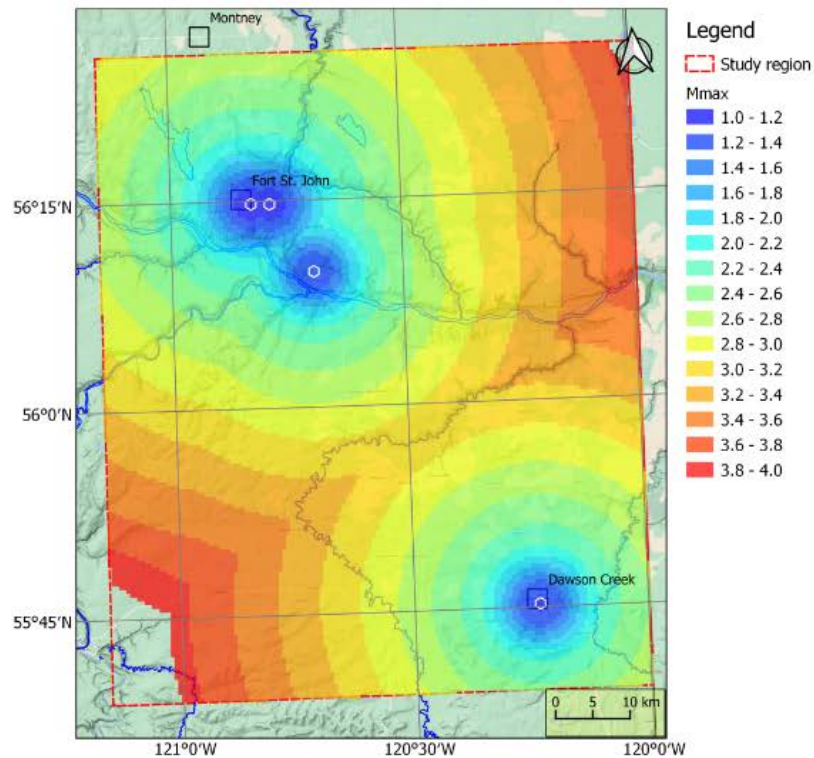
Depth: 1 km

10% Probability to Exceed **Perception** PGV 0.07 cm/s



Depth: 1 km

Figure 3-7: Maps of M_{max} of earthquakes at depth of 1 km considering perception thresholds in the entire area. Left: 10% probability of exceeding perception threshold acceleration of 2.5 cm/s² and right: 10% probability of exceeding perception threshold velocity of 0.07 cm/s.

10% Probability to Exceed **Perception** PGA 2.5 cm/s^2

Depth: 2.1 km

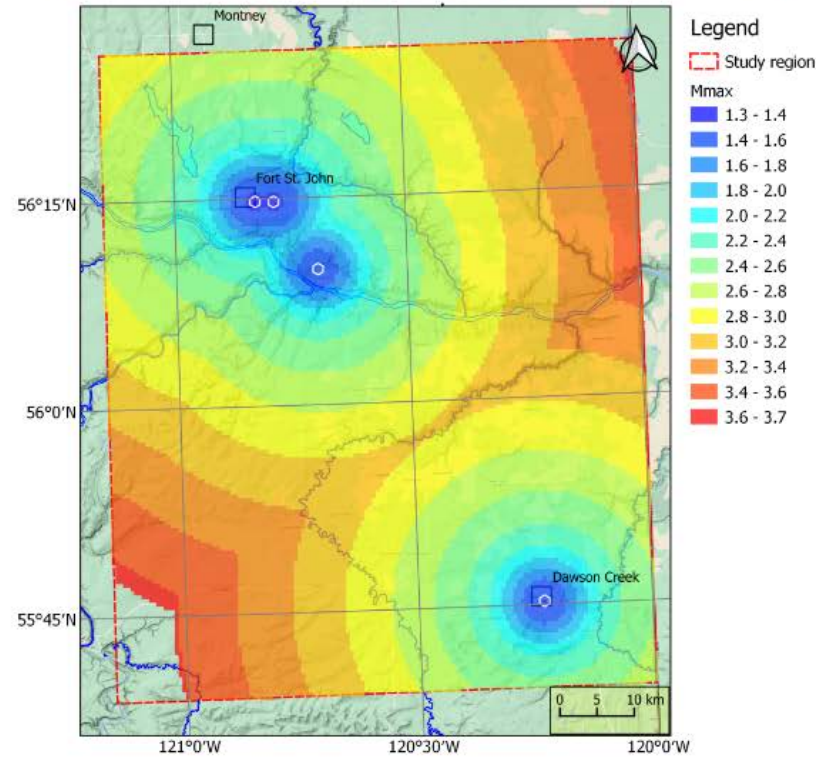
 10% Probability to Exceed **Perception** PGV 0.07 cm/s

Depth: 2.1 km

Figure 3-8: Maps of M_{\max} of earthquakes at depth of 2.1 km considering perception thresholds in the entire area. Left: 10% probability of exceeding perception threshold acceleration of 2.5 cm/s^2 and right: 10% probability of exceeding perception threshold velocity of 0.07 cm/s .

3.3 Conclusions

While MMI can be used as a simple measure of damage potential, there is no single definitive measure of what makes ground-motion damaging. A combination of factors including the amplitude, frequency content and duration of motion will determine the damage potential. Small-to-moderate events tend to be of short duration and are rich in high frequency content (at close distances), whereas larger events are longer in duration and have significant energy at longer periods. The overall robustness and frequency range of response of a structure will greatly impact the overall damage potential of motions.

Magnitude maps based on PGA tend to result in lower values than the maps generated based on PGV and additionally, PGA tends to be well correlated with felt effects whereas PGV tends to be well correlated with damage (e.g. Worden et al., 2012). To this end, it is recommended to define perception threshold levels based on PGA where the potential for damage should rely on PGV. Furthermore, with the goal in mind to mitigate the risk of generating potentially damaging ground motions, this study considered a conservative approach in defining the ground motion thresholds, where a 10% probability of exceeding the lower boundary of the corresponding MMI categories for the perception level and the beginning of non-structural damage potential are considered. It is noted that these thresholds mark the lower extent where ground motions may begin to be felt and may have the potential for damage. The likelihood of perception or damage increases with increasing ground motion, where damage also largely depends on the type, size, robustness and age of a structure.

When considering earthquakes that are unlikely to have any threshold exceedance across the entire region, the magnitude range of the perception level is from M_w 0.8 - 1.5 (related to PGA), and for the possibility of non-structural damage the magnitude ranges from M_w 3.0 - 3.5 (related to PGV). The overall magnitude level where ground motions begin to exceed the thresholds is primarily controlled by the depth of the event, where localized variations are attributed to differences in site condition. Areas with relatively higher magnitudes are associated with shallower and stiffer ground conditions and areas with relatively lower magnitudes are associated with areas having deeper and softer soil profiles. This trend is due to the fact that a smaller magnitude earthquake can generate relatively larger ground motions at the surface if the soil conditions amplify the waves

where a larger magnitude event may have lower ground motions at shallower and stiffer sites which are associated with relatively lower amplifications.

When considering threshold exceedance at densely population localities, at the perception level, we observe magnitudes in the range of $M_w 0.8-1.0$ within the municipality limits, where the magnitude increases by an entire magnitude unit within the first 6 km and roughly another whole magnitude unit for every 10 km further away from the locality. This comparison was largely carried out to demonstrate how M_{Max} maps can be generated to limit threshold exceedances at specific reference locations rather than the region as a whole. It is understood that there are a number of rural dwellings in close proximity to operations, where perceptible and damaging motions are unacceptable.

4. Summary

In this study, ground motion prediction equations and site amplification maps were generated for PGA and PGV using data from public as well as privately operated seismograph stations and available geological/geotechnical information throughout the region. First, attenuation was modeled in the Fourier domain in order to play back attenuation and correct ground motion recordings to the source (hypocenter) and calculate source parameters such as moment magnitude and stress drop through a displacement spectral fitting approach. In order to ensure robust scaling of ground motions with respect to moment magnitude, a relationship between moment magnitude and stress drop was found and used as an input to earthquake simulations. Next, earthquake records were corrected for magnitude scaling effects as well as alternative geometric spreading rates and inverted to determine the anelastic attenuation, empirical site amplification factors and an overall calibration factor. Ground motion variability is characterized such that alternative percentiles of motion that are likely or unlikely to occur as a result of a seismic event at some distance away may be estimated. The empirical site amplification factors are referenced to the average site response in the region and are correlated with geological and geotechnical attributes such as the shear wave velocity in the top 30 m, depth to bedrock and surficial geological unit. The developed site amplification models are evaluated for a grid with 500x500m spacing across the region of interest in order to estimate localized site effects at uninstrumented locations. Given an earthquake location and magnitude, ground motion prediction equation and site amplification maps are combined to generate shakemaps which describe the shaking distribution throughout the study region.

Literature is reviewed in order to identify appropriate ground motion thresholds in terms of PGA and PGV for the human perception and damage level. USACE (1972), The findings of Barneich (1985), New (1990), Athanasopoulos & Pelekis (2000), and Bommer et al. (2006) were investigated to understand perception thresholds based on different types of sources. In these studies, vibrations due to traffic, blasting, and pile-driving were investigated. At relatively close distances, earthquake ground motions due to induced seismicity are generally short in duration and the wavelet is more pulse-like due to their shallow depths and are more analogous to vibrations resulting from blasts or pile-driving. It was found that perception levels are on the order of 0.1 cm/s for these motion types. Damage can be defined in two broad categories: non-structural and structural.

Non-structural damage includes cracking, chipping or detachment of non-structural elements such as plaster, tiles, finishes or non-load bearing walls that do not compromise the overall safety of the building. Structural damage includes any damages that impact the load-bearing elements of a structure such as beams, columns, walls and the foundation which compromises the safety and continued use of the structure. In terms of ground motions which may be damaging, the thresholds vary depending on the type, size and age of a structure, and that different elements of a structure will react differently to ground motion loads due to their strengths. Onur and Seeman (2004) and Onur (2008) suggest that non-structural damage levels may begin to occur at Modified Mercalli Intensities (MMI) of VI where structural damage may begin to occur at MMI of VII.

Ground motion intensity conversion equations (GMICE) are commonly used to translate a description of an experienced ground motion to an intensity value (MMI), which can then be further converted into a ground motion in terms of PGA or PGV. A model developed by Caprio et al. (2015) using felt reports correlated to ground motion recordings from a large global database was selected for use in this study. Felt reports and their associated recorded ground motions from larger events in the Kiskatinaw region are investigated to determine the suitability of the Caprio et al. (2015) equation. Overall a good agreement is found between the descriptions in the report with MMI value and the associated range of ground motions for each intensity level. This study examined motions due to events of magnitudes $M_w > 2.8$ and found that the smallest perceived motions (perception threshold) are about $PGV \geq 0.07$ cm/s corresponding to intensity of MMI ~ II-III, and $PGA \geq 2.5$ cm/s² (0.26%g, equivalent of a M1.5 at 1.7 km depth). Consistent with USACE(1972) study perception thresholds due to blast and the lowest perceptible amplitudes of Athanasopoulos & Pelekis (2000).

Motions associated with non-structural and structural damage motion thresholds are calculated using inverted equations of Caprio et al., (2015) corresponding to intensities of MMI ~ VI and VII (Onur et al, 2008; and Onur & Seemann 2004). The calculated motions for non-structural damage thresholds are PGV of 5.52 cm/s and PGA of 84.3 cm/s² (8.6%g, equivalent to a M3.1 at 1.7 km depth). For structural damage, the thresholds of PGV are 13.87 cm/s and 154.0 cm/s² for PGA (15.7%g, equivalent to a M3.5 at 1.7 km depth). PGA is found to be well correlated with felt effects whereas PGV tends to be well correlated with damage (Worden et al., 2012). In this study it is recommended that perception thresholds

are defined based on PGA where thresholds related to potential damage are defined based on PGV.

With the goal in mind to mitigate the risk of generating potentially damaging ground motions, this study considered a conservative approach in relating the ground motion thresholds with equivalent magnitude. The magnitude of earthquake having an unlikely probability (10%) of exceeding the lower boundary of the corresponding MMI categories for the perception level and the beginning of non-structural damage potential are determined. It is noted that these thresholds mark the lower extent where ground motions may begin to be felt and may have the potential for damage. The likelihood of perception or damage increases with increasing ground motion, where damage also largely depends on the type, size, robustness and age of a structure.

When considering earthquakes that are unlikely to have any threshold exceedance across the entire region, the magnitude range of the perception level is from M_w 0.8 - 1.5 (related to PGA), and for the possibility of non-structural damage the magnitude ranges from M_w 3.0 - 3.5 (related to PGV). In general, the largest ground motion amplitudes are expected to occur in very close proximity to the epicenter of an earthquake. In areas where near-surface conditions rapidly change from relatively low amplification to relatively high amplifications over short distances, it is possible that the effects of amplification at a particular site will overcome the ground motion amplitude lost due to attenuation, and that the peak ground motion from an event may be experienced up to 10 km away from the epicenter. It should be noted that ground motions generated by events that may approach the thresholds are within 10 km of the epicenter, are controlled largely by localized site conditions, and attenuate rapidly with increasing distance.

References

Ahmadzadeh, S., Doloei, G. J., and H. Zafarani (2020). Ground motion to intensity conversion equations for Iran," *Pure and Applied Geophysics*, 177(11), 5435–5449.

Anderson, J. G., and S. E. Hough (1984). A model for the shape of the Fourier amplitude spectrum of acceleration at high frequencies. *Bulletin of the Seismological Society of America*, 1984, Vol.74 (5), p.1969-1993.

Athanasopoulos, G.A., and P.C., Pelekis (2000). Ground vibrations from sheetpile driving in urban environment: measurements, analysis and effects on buildings and occupants. *Soil Dynamics and Earthquake Engineering*, (19) 371-387.

Atkinson, G. M., and S.I., Kaka (2007). Relationships between felt intensity and instrumental ground motion in the central United States and California. *Bulletin of the Seismological Society of America* (97) 497-510.

Atkinson, G.M. (1996). The high-frequency shape of the source spectrum for earthquakes in eastern and western Canada, *Bull. Seism. Soc. Am.* 86(1A), 106-112.

Barneich, J.A. (1985). Vehicle induced ground motion. In: Gazetas G, Selig ET, editors. *Vibration problems in geotechnical engineering*. Special Publication of ASCE, 187-202.

BCER Kiskatinaw Seismic Monitoring and Mitigation Area Velocity Model developed by Nanometrics Inc. (May, 2020).

Bilal, M., and A. Askan (2014). Relationships between felt intensity and recorded ground-motion parameters for Turkey," *Bulletin of the Seismological Society of America*, 104(1), 484–496.

Bommer, J.J., Oates, S., Cepeda, J.M., Lindholm, C., Bird, J., Torres, R., Marroquin, G., and J. Rivas (2006). Control of hazard due to seismicity induced by a hot fractured rock geothermal project. *Engineering Geology*, (83) 287-306.

Boore, D. M. and G. M. Atkinson (1987). Stochastic prediction of ground motion and spectral response parameters at hard-rock sites in eastern North America, *Bull. Seism. Soc. Am.* 77, 440-467

Boore, D.M., Joyner, W.B., and L. Wennerberg, (1992). Fitting the stochastic ω^{-2} source model to observed response spectra in western North America: Trade-offs between $\Delta\sigma$ and κ , *Bull. Seism. Soc. Am.*, 82(4), 1956-196.

Caprio, M., Tarigan, B., Worden, C.B., Wiemer, S., and D.J. Wald, (2015). Ground motion to intensity conversion equations (GMICEs): a global relationship and evaluation of regional dependency. *Bulletin of the Seismological Society of America*, (105) 1-21.

Census Profile, 2021 Census of Population, Statistics Canada.

<https://www12.statcan.gc.ca/census-recensement/2021/dp-pd/prof/details/page.cfm?Lang=E&SearchText=Fort%20St%2E%20John&DGUIDlist=2021S05100298&GENDERlist=1,2,3&STATISTIClist=1&HEADERlist=0>

Dewey, J., Reagor, B., Dengler, L., and K. Moley (1995). Intensity and Iseismal Maps for the Northridge, California, Earthquake of January 17, 1994. USGS Open File Report 95-92

Electric Power Research Institute (1993). Guidelines for determining design basis ground motions, Palo Alto, Calif. Electric Power Research Institute, vol. 1-5, EPRI TR-102293.

Goulet, C., Bozorgnia, Y., Abrahamson, N., Kuehn, N., Al Atik, L., Youngs, R., and R. Graves (2018). Central and eastern North America ground-motion characterization - NGA-East final report, Pacific Earthquake Engineering Research Center, PEER 2018/08, 817 pp.

Hanks, T. C., and H. Kanamori (1979). A moment magnitude scale. *Journal of Geophysical Research*, 84(B5), 2348. doi:10.1029/jb084ib05p02348

Hashash YMA, Ilhan O, Harmon JA, et al. (2020) Nonlinear site amplification model for ergodic seismic hazard analysis in central and eastern North America. *Earthquake Spectra* 36(1): 69–86.

Human Perception, the World of Explosives.

<https://explosives.org/vibration-basics/human-perception/>

Kaka, S., and G. Atkinson (2004). Relationships between instrumental intensity and ground motion parameters in eastern North America. *Bulletin of the Seismological Society of America*. 94, 1728–1736.

McGuire, R. K., W. J. Silva, and C. J. Costantino (2001). Technical Basis for Revision of Regulatory Guidance on Design Ground Motions: Hazard- and Risk-consistent Ground Motion Spectra Guidelines, NUREG/CR-6728, U.S. Nuclear Regulatory Commission, Washington, DC.

Mortalla, J. M., Godes, T., Rhoades, D. A., Canessa, S., and M. C. Gerstenberger (2021). New ground motion to intensity conversion equations (GMICEs) for New Zealand. *Seismological Research Letters*, 92(1), 448–459.

Murphy J.R. and L.J., O'Brien (1977). The correlation of peak ground acceleration amplitude with seismic intensity and other physical parameters. *Bulletin of the Seismological Society of America*, 67, 877-915.

NBCC (2015). National Building Code of Canada, National Research Council of Canada, Volume 1, 1412 pp.

New, B. M. (1990). Ground vibration caused by construction works. *Tunnelling and Underground Space Technology* 5(3): 179-190, doi.org/10.1016/0886-7798(90)90004-4

Onur, T., Seemann, M., Halchuk, S., and J. Adams, (2008). Probabilities of significant earthquake shaking in communities across Canada. *Proceedings of the 14th World Conference in Earthquake Engineering*, Beijing, China.

Onur, T., and M., Seemann, (2004). Probabilities of significant earthquake shaking in communities across British Columbia: implications for emergency management. *Proceedings of the 13th World Conference in Earthquake Engineering*, Vancouver, BC, Canada, Paper No. 1065.

PEER, NGA-East: Median Ground-Motion Models for the Central and Eastern North America Region, PEER Report 2014/17, Pacific Earthquake Engineering Research Center, Headquarters at the University of California, Berkeley, CA. 2015

Silva, W.J. and R. Darragh (1995). Engineering characterization of earthquake strong ground motion recorded at rock sites, Palo Alto, Calif: Electric Power Research Institute, Rept. TR 102261.

Siskind, D.E., Stagg, M.S, Kopp, J.W., and C.H., Dowding, (1980). Structure response and damage produced by ground vibration from surface mine blasting. United States Bureau of Mines Report of Investigations 8507 (USBM RI 8507), p59.

Sokolov, V. Y. (2002). Seismic intensity and Fourier acceleration spectra: revised relationship. *Earthquake Spectra*, 18(1) 161–187.

Stewart J., G. Parker, G., Atkinson, Boore, D., Hashash, Y., and W. Silva (2020). Ergodic site amplification model for central and eastern North America. *Earthquake Spectra* 36(1): 42-68.

Stover, C.W. and J.L. Coffman, (1993). Seismicity of the United States, 1568-1989 (Revised), U.S. Geological Survey Professional Paper 1527, 417 pp.

Tian, X., Wen, Z., Zhang, W., and J. Yuan (2021). New ground motion to intensity conversion equations for China. *Hindawi*, <https://doi.org/10.1155/2021/5530862>

USACE, (1972). Systematic drilling and blasting for surface excavations. Engineering Manual EM 1110-2-3800US Army Corps of Engineers.

USGS, Did you feel it? <https://earthquake.usgs.gov/data/dyfi/>

USGS, Earthquake intensity scale Modified Mercalli Intensity (MMI).
<https://www.usgs.gov/media/images/earthquake-intensity-scale>

Yenier, E and G. Atkinson, (2014). Equivalent point-source modeling of moderate-to-large magnitude earthquakes and associated ground-motion saturation effects. *Bulletin of the Seismological Society of America*, 104 (3), p.1458-1478, DOI: 10.1785/0120130147

Wald, D. J., Heaton, T. H., and H. Kanamori (1999). Relationship between peak ground acceleration, peak ground velocity, and modified mercalli intensity in California. *Earthquake Spectra*, 15(3), 557-564.

Wood, H.O. and F., Neumann (1931). Modified Mercalli Intensity scale of 1931. *Bulletin of the Seismological Society of America*, 21, 277-283.

Worden, C.B., Gerstenberger, M.C, Rhoades, D.A., and D.J. Wald, (2012). Probabilistic relationships between ground-motion parameters and modified Mercalli intensity in California. *Bulletin of the Seismological Society of America*, (102) 204-221.

Wu, Y. M., Teng, T. L., Shin, T. C., and N. C. Hsiao (2003). Relationship between peak ground acceleration, peak ground velocity, and intensity in Taiwan. *Bulletin of the Seismological Society of America*, 93(1) 386–396.

Company Profile

Nanometrics Inc.

Nanometrics is an industry-leading developer of seismic monitoring and consulting solutions. Headquartered in Kanata, Ontario, with offices and representatives worldwide, Nanometrics has over 30 years' experience, delivering solutions to customers across the globe. Our real-time and portable seismic systems are utilized by the world's leading scientific institutions, universities, and major corporations. Our pedigree is founded on precision instrumentation, network technology and software applications for seismological and environmental research. We specialize in collecting and analyzing critical real-time data for global, regional and local seismic networks. As one of the world's largest seismic network operators, we offer proven network design methodology, station deployment, and network maintenance capabilities and extensive in-house data processing and analysis experience.

Our scientific and operational experience in seismology means we work closely with industry groups and researchers to stay abreast of regulatory discussions and ensure our systems are ready for any potential changes. The Nanometrics team is made up of industry experts engaged in operations, instrument design, software development, service and installation with a dedicated Science and Technology Research unit focused on data processing, machine learning/artificial intelligence (AI) based event detection, passive seismic monitoring, and engineering seismology services.

Nanometrics' Engineering Seismology Services is a suite of integrated consulting and monitoring solutions to assist in the assessment and management of seismic risk for critical infrastructure and structural integrity. With Nanometrics' in-depth seismic hazard assessment and monitoring services, operators can make informed decisions about the seismic risk to ensure that assets are protected, and stakeholders are informed. Our Engineering Seismology Services range over a wide spectrum of monitoring and analysis solutions, including:

Monitoring Services

- Real-time seismic monitoring
- 24/7 network operation
- AI-based event detection
- Manual review service
- Advanced data processing
- Rapid event/ground motion notification
- Earthquake early warning
- Structural health monitoring

Consulting Services

- Catalog enhancement
- Seismic source characterization
- Ground motion prediction
- Site response characterization
- Seismic microzonation
- Seismic hazard and risk assessment
- Scenario event and ground motion simulation
- Time history selection and scaling